Int J Thermophys (2012) 33:1776–1777
DOI 10.1007/s10765-012-1336-4

Photoacoustic, Photothermal, and Diffusion-Wave Sciences in the Twenty-First Century: Triumphs of the Past Set the Trends for the Future

Andreas Mandelis

Received: 3 May 2012 / Accepted: 6 October 2012 / Published online: 4 November 2012
© Springer Science+Business Media New York 2012

Abstract A handful of early breakthroughs in photoacoustic science and engineering since its modern-day (scientific) renaissance in the 1970s has defined directions in the development of the photoacoustic, photothermal, and diffusion-wave fields in the past 40 years that have shaped modern day developments and have led to an impressive range of vibrant and unique technologies in the third millennium (technological renaissance). A power-point presentation on the ICPPP-16 opening plenary talk focuses on the historical roots of what I perceive to be some of today's most successful and unique technologies, while readily acknowledging the impossibility to be all inclusive. It can be found under the url: http://cadift.mie.utoronto.ca/History_of_Photoacoustics-Photothermics.ppt. The thematic areas in question include historical reviews selected among the following topics: Piezoelectric photoacoustic microscopy (PAM) which, along with early gas-phase PA spectroscopic studies of biomaterials such as blood haemoglobin and progress in the physics of photon diffusion waves, has led to the modern-day explosion in biomedical photoacoustic imaging technologies with future trends for photoacoustic and ultrasound co-registered imagers; Thermoreflectance, piezoelectric, and gas-phase PA imaging of semiconductors which, along with developments in photocarrier diffusion wave physics, led to photocarrier radiometry, nanolayer diagnostics, carrierographic imaging of optoelectronic materials, and devices with industrial trends in solar cell inspection and control; Photoacoustic gas-phase and infrared radiometric probing and scanning imaging NDE which led to lock-in thermography and have spawned industrial and biomedical technologies; Thermal-wave interferometry and the quest for thermal coherence which led to thermal-wave cavities, the thermal-wave radar, and derivative depth profiling

technologies, and, very recently, thermal coherence tomography. This review is meant to be a growing public record of work in progress, with new materials in the given thematic areas and other thematic areas being added as more information on the rich history of the field becomes available. Direct inputs to the author by the broader photoacoustic, photothermal, and diffusion-wave community are solicited and strongly encouraged to ensure that all landmark and seminal work that shaped the state of the science and art in the field receives fair and deserving exposure and the historical review becomes truly representative and comprehensive.

Keywords Diffusion waves · History · Photoacoustic · Photothermal · Science · Technology

Acknowledgments I wish to acknowledge the valuable contributions of all those researchers in the field who have contributed important historical information to the review.

Andreas Mandelis (mandelis@mie.utoronto.ca)

PHOTOACOUSTIC, PHOTOTHERMAL AND DIFFUSION-WAVE SCIENCES IN THE 21ST CENTURY: TRIUMPHS OF THE PAST SET THE TRENDS FOR THE FUTURE
1961 – 2011+

Andreas Mandelis

Center for Advanced Diffusion-wave Technologies (CADIFT),
Department of Mechanical and Industrial Engineering,

University of Toronto, Toronto, Ontario M5S 3G8, Canada

CADIFT

Outline

- **Historical Photoacoustic and Photothermal Background: Our roots, 1973 – 2011+**
- **From Piezoelectric PA Microscopy to Biomedical Ultrasonic Photoacoustics and Imaging.**
- **From Gas-Cell Microphone PA to Optoelectronic Diffusion-Wave Imaging and High-Frequency Carrierography based on Energy Conversion Processes in Semiconductors and Devices**
- **From Gas-Cell Scanned NDT to Lock-in Thermography and the Thermal-Wave Radar Imager**

I. Historical Past

- The beginning of modern day photoacoustics:
- **J. G. Parker**, Applied Physics Laboratory, Johns Hopkins University, *"Optical Absorption in Glass: Investigation Using an Acoustic Technique"*, Appl. Opt. **12**, 2974 (December 1973)

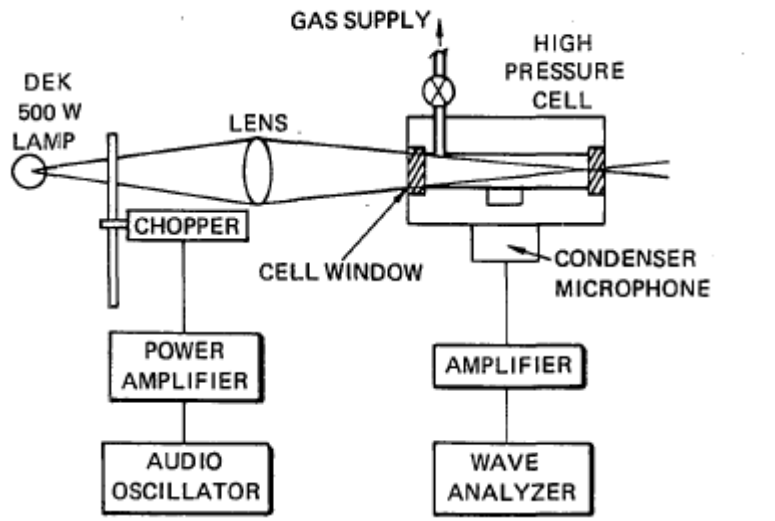

Fig. 1. Schematic diagram of the experimental arrangement. The focal length of the lens was 9.6 cm.

J. G. Parker

II. Theory

Applying the heat equation to the glass (region I) and to the gas (region II), we have, assuming a periodic time dependence,

$$-\kappa_1 \nabla^2 T_1 + j\omega C_1 T_1 = \alpha_1 I_0, \tag{1}$$

where κ_1 is the thermal conductivity of the glass, C_1 is the specific heat per unit volume, α_1 is the absorption coefficient, and I_0 the incident light intensity. Designating $x = 0$ as the glass-gas interface, we find as the physically important solution of Eq. (1)

$$T_1(x) = C_1 \exp(k_1 x) - j(\alpha_1 I_0/\omega C_1), \tag{2}$$

where

$$k_1 = [j(\omega C_1/\kappa_1)]^{1/2}. \tag{3}$$

In region II, we have neglecting the effect of gas viscosity,

$$\kappa_2 \nabla^2 T_2 - j\omega C_{p2} T_2 = -j\omega p_e, \tag{4}$$

where κ_2 is the gas thermal conductivity, C_{p2} is the specific heat at constant pressure per unit volume, and p_e is the differential pressure. Invoking the equations of state and continuity, we obtain from Eq. (4)

$$j(\kappa/\omega)\nabla^4 T_2 + [C_p + j(\gamma\kappa/\omega)k_0^2]\nabla^2 T_2 + k_0^2 C_p T_2 = 0, \tag{5}$$

where γ is the ratio of specific heats and $k_0 = \omega/c_0$, c_0 being the velocity of sound and is given by

$$c_0 = [(\gamma p_0/\rho_0)]^{1/2}, \tag{6}$$

where p_0 is the ambient pressure and ρ_0 the corresponding density.

J. G. Parker

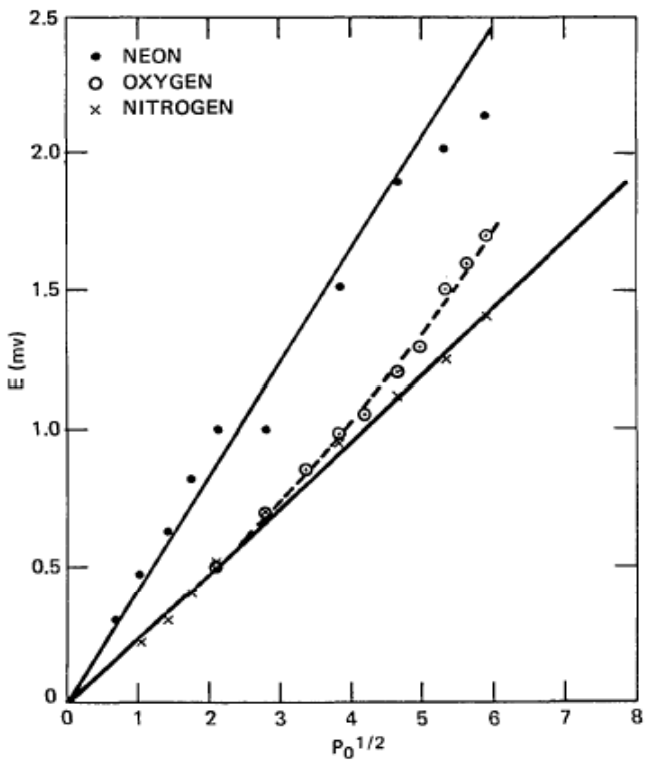

Fig. 2. Sound pressure level indicated by the wave analyzer plotted vs cell pressure to the one-half power for the gases N_e, N_2, and O_2 for a constant chopping frequency of 416 Hz.

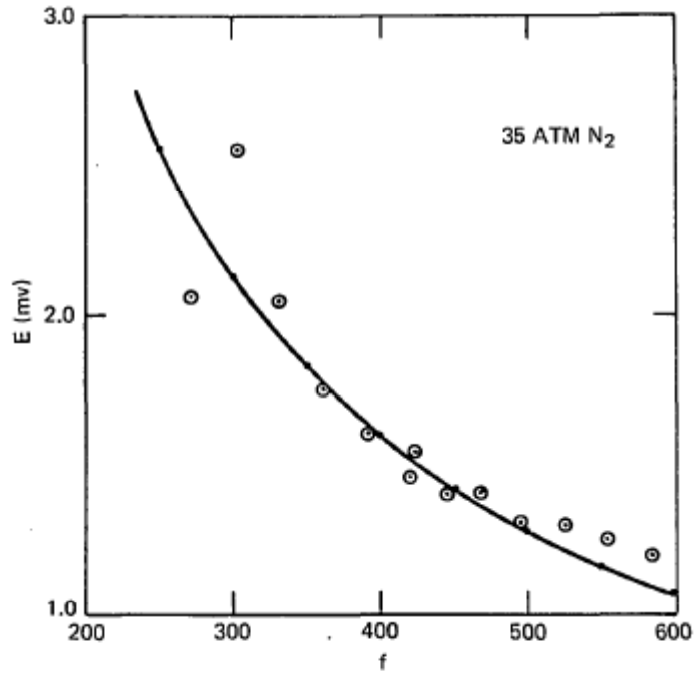

Fig. 3. Sound pressure level in N_2 indicated by the wave analyzer plotted vs frequency for a pressure of 35 atm.

III. Conclusion

The phenomenon of optically generated sound described here seems to be reasonably well explained on the basis of a thin absorbing layer whose function is to convert light to heat, which in turn is communicated to the gas by thermal conduction. This layer could correspond either to an adsorbed gas layer or to a surface layer in the glass itself. If adsorption

Allan Rosencwaig and Allen Gersho, Bell Laboratories. Murray Hill. New Jersey, *"Theory of the photoacoustic effect with solids",* J. Appl. Phys. **47** (1), 64 (1976).

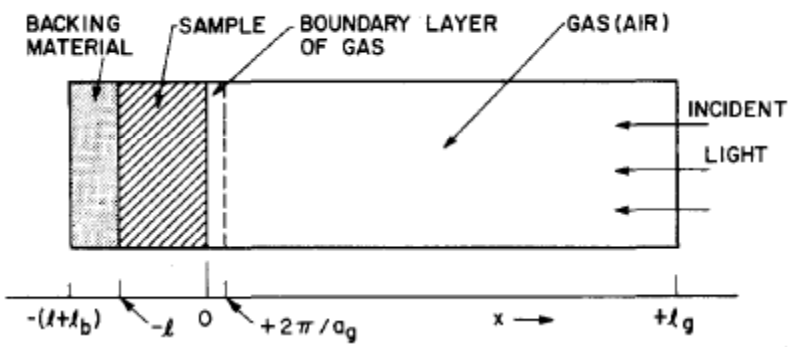

FIG. 1. Cross-sectional view of a simple cylindrical photoacoustic cell, showing the positions of the solid sample, backing material, and gas column.

The thermal diffusion equation in the solid taking into account the distributed heat source can be written

$$\frac{\partial^2\phi}{\partial x^2} = \frac{1}{\alpha_s}\frac{\partial\phi}{\partial t} - A\exp(\beta x)[1+\exp(j\omega t)], \quad \text{for } -l \leq x \leq 0, \qquad (1)$$

with

$$A = \beta I_0 \eta / 2k_s,$$

$$\frac{\partial^2\phi}{\partial x^2} = \frac{1}{\alpha_b}\frac{\partial\phi}{\partial t}, \qquad -l-l_b \leq x \leq -l \qquad (2)$$

$$\frac{\partial^2\phi}{\partial x^2} = \frac{1}{\alpha_g}\frac{\partial\phi}{\partial t}, \qquad 0 \leq x \leq l_g. \qquad (3)$$

Allan Rosencwaig and Allen Gersho

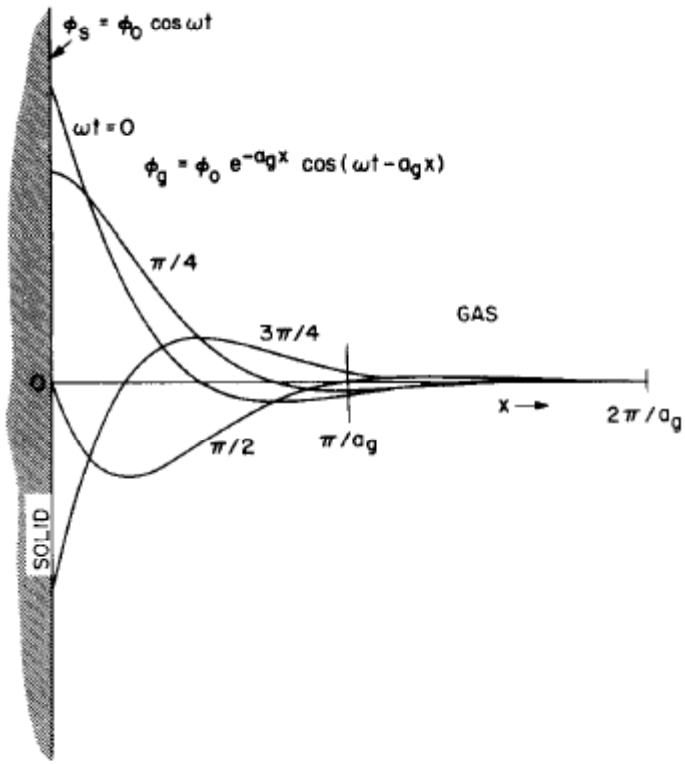

FIG. 2. Spatial distribution of the time-dependent temperature within the gas layer adjacent to the solid surface.

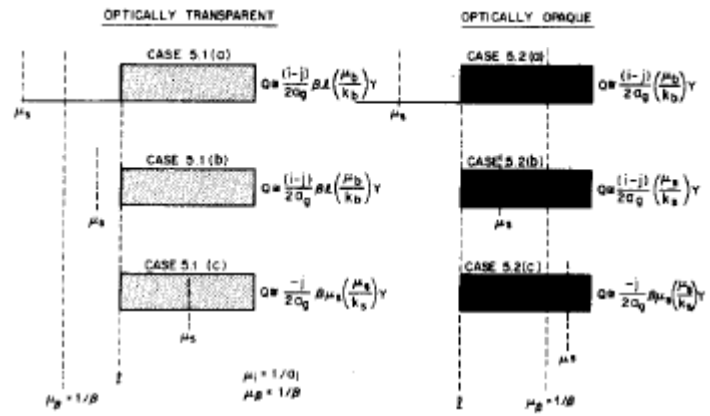

FIG. 3. Schematic representation of special cases discussed in the text.

Our formulas show that the photoacoustic signal is ultimately governed by the magnitude of the thermal diffusion length of the solid. Thus even when a solid is optically opaque, it is not necessarily opaque photoacoustically and, in fact, as long as $\beta\mu_s < 1$, the photoacoustic signal will be proportional to β, even though

tractive. In particular, these features give the photoacoustic technique a unique potential for noninvasive *in vivo* studies of human tissues, a potential which may have important implications in biological and medical research and in medical diagnostics.

II. From Piezoelectric PA Microscopy to Biomedical Ultrasonic Photoacoustics and Imaging

J. E. Michaels, Structures and Dynamics Operation, Aerosciences Laboratory Missile and Space Vehicle Department, General Electric Company, *"THERMAL IMPACT-THE MECHANICAL RESPONSE OF SOLIDS TO EXTREME ELECTROMAGNETIC RADIATION"*, Planetary Space Sci. **7**, 427 (1961)

Abstract—The phenomenon of thermally induced stress waves resulting from the deposition by radiation of intense electromagnetic energy into the surface of a solid is described. Both theoretical and experimental aspects are treated. The derivation and general solution for the case of a semi-infinite bar are given. A recent experiment is described which for the first time demonstrated and verified the thermal impact phenomenon. The design and development of an optimized experimental facility by which the phenomenon can be studied in the laboratory is discussed.

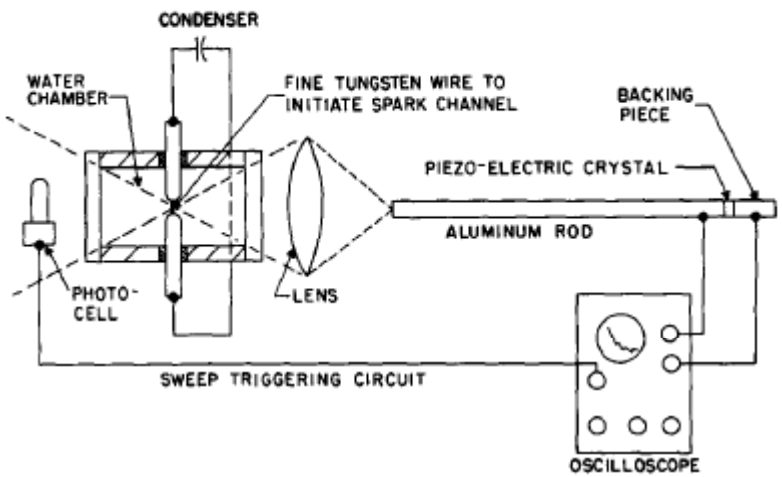

Fig. 2. Schematic of thermal impact experiment.

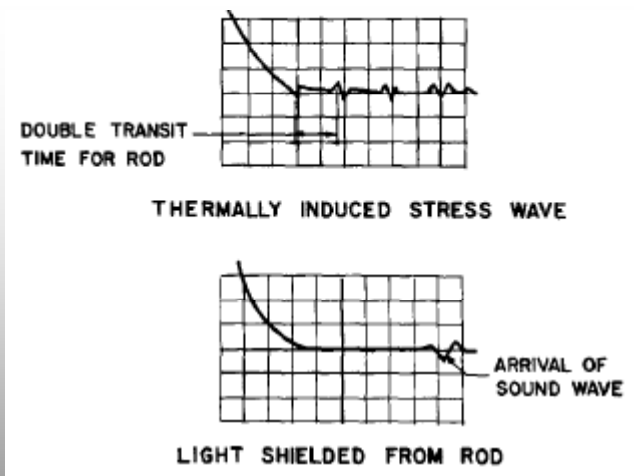

Fig. 3. Oscilloscope records of thermally induced stress waves. (Horizontal sweep 200 μsec per division.)

J. E. Michaels

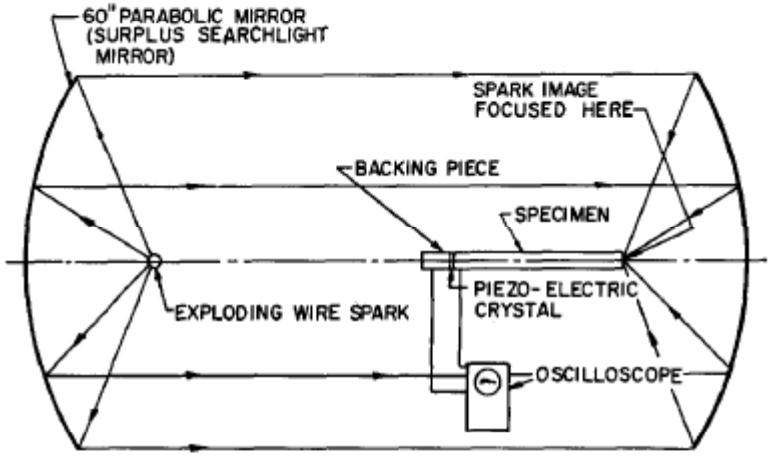

Fig. 4. Diagram of thermal impact facility.

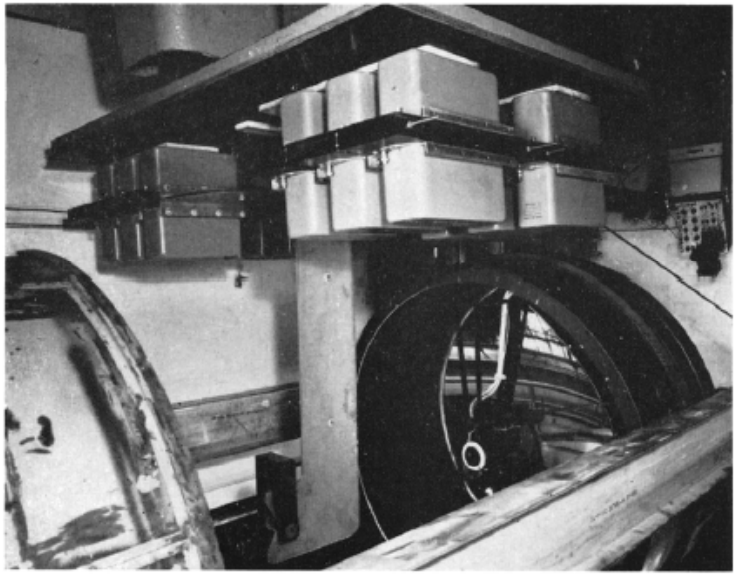

Fig. 5. Capacitor bank and copper conductor plates.

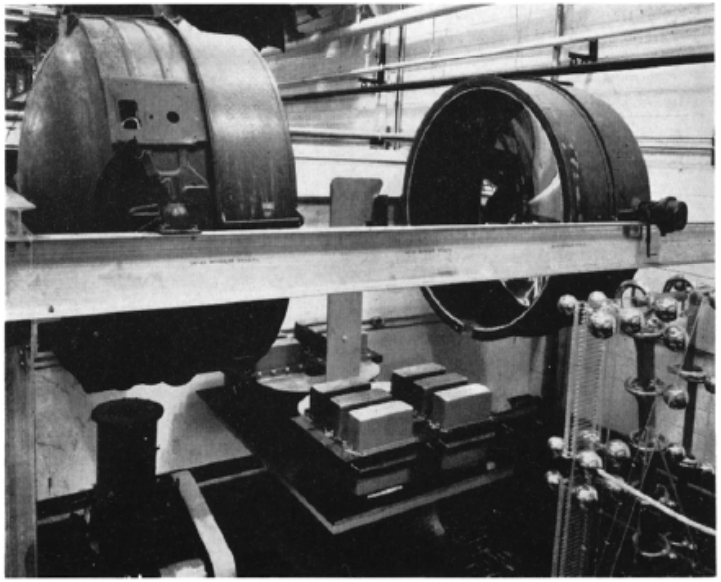

Fig. 7. General view of thermal impact facility.

From Piezoelectric PA Microscopy to Biomedical Ultrasonic Photoacoustics and Imaging

R. M. White, Traveling-Wave Tube Product Section, General Electric Company, Palo Alto, California, "*Elastic Wave Generation by Electron Bombardment or Electromagnetic Wave Absorption*", J. Appl. Phys. **34**, 2123 (1963)

HIGH-FREQUENCY elastic waves have been produced by the impact of a pulsed beam of electrons upon a solid target in a highly evacuated chamber. Elastic waves have also been produced by pulses of microwave-frequency, electromagnetic energy and light upon their absorption at the surfaces of elastic solids and fluids. Acoustic waves produced by electron impact

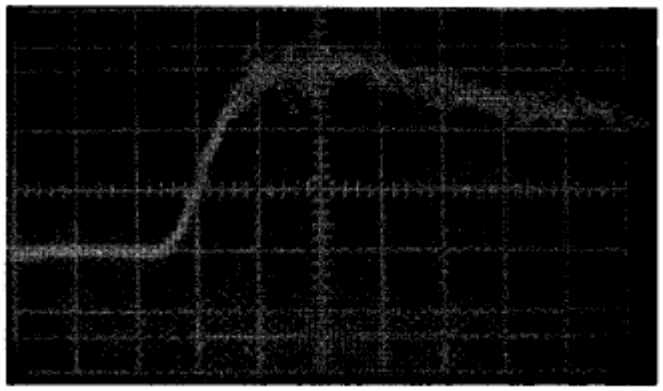

FIG. 2. Output of acoustic probe when illuminated directly in air by pulsed ruby laser. (Vertical deflection 1 mV/major division; horizontal scale, 50 μsec/major division.)

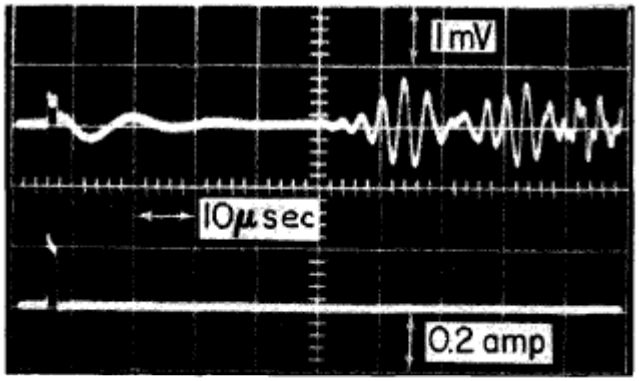

FIG. 3. Oscilloscope traces showing (top) electrical output of acoustic probe in contact with stainless steel target rod under impact of an electron beam pulse (cathode current pulse shown in bottom trace). Multiple elastic wave signals are believed due to wave reflections in target rod.

TABLE 1. Relative measured and corrected acoustic probe output voltages and relative values of $k\alpha(K\rho c)^{-\frac{1}{2}}$. For ease of comparison, relative values were set equal to unity for stainless steel.

Target material	Measured acoustic probe output voltage	Corrected acoustic probe output voltage	Computed value of $k\alpha(K\rho c)^{-\frac{1}{2}}$ for material
Stainless steel (304)	1.00	1.00	1.00
Copper	0.24	0.27	0.20
Molybdenum	0.12	0.14	0.19
Invar	0.060	0.036	0.057–0.036

where α is the coefficient of thermal expansion, Q_0 is the input heat flux density, K is the thermal conductivity, ρ is the density, and c is the specific heat. The amplitude of the compressional stress normal to the surface is $k\alpha\theta$, where k is the bulk modulus of compressibility. Thus, for input heat pulses of fixed duration, the peak value of the normal thermal stress at the heated (and constrained) surface is proportional to $k\alpha(K\rho c)^{-\frac{1}{2}}$. In Table I the

R. M. White, Department of Electrical Engineering, University of California, Berkeley, California, *"Generation of Elastic Waves by Transient Surface Heating"*, J. Appl. Phys. **34**, 3559 (December 1963)

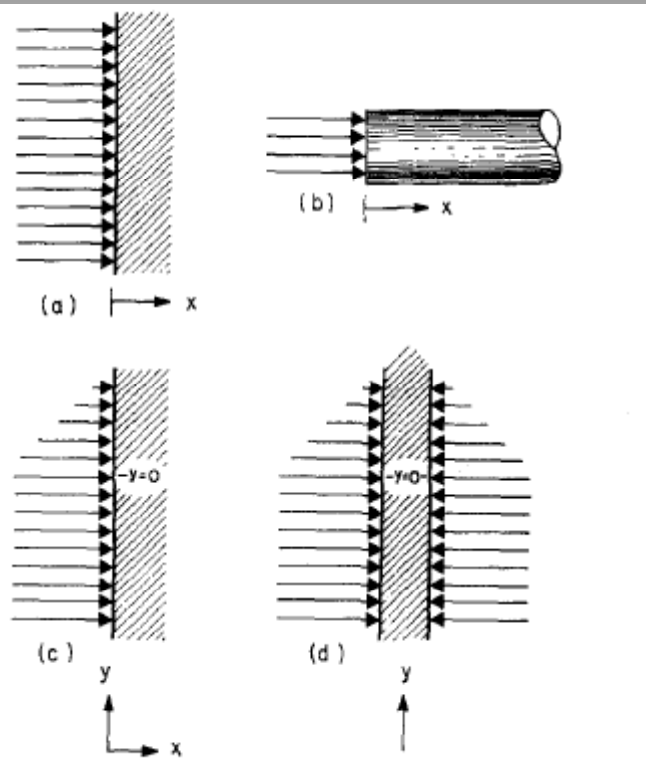

FIG. 1. Transient heating conditions. (a) Uniform heating of surface of semi-infinite body. (b) Uniform heating of end of long rod. (c) Nonuniform heating of semi-infinite body. (d) Section of thin lamina heated nonuniformly in y direction, representative of layer near surface of body in (c).

The equations of motion for the semi-infinite body and the rod are

$$\rho(\partial^2 u/\partial t^2) = (\partial\sigma_{xx}/\partial x)$$
$$= (\lambda+2\mu)(\partial^2 u/\partial x^2) - Ba(\partial\theta/\partial x) \quad \text{(semi-infinite body)} \quad (2.5a)$$
$$= E(\partial^2 u/\partial x^2) - Ea(\partial\theta/\partial x) \quad \text{(thin rod)}, \quad (2.5b)$$

where ρ is the density of the body. Recognizing that the elastic constants are related to the velocities of wave propagation by

$$(\lambda+2\mu) = \rho v_L^2, \quad (2.6a)$$

and

$$E = \rho v_R^2, \quad (2.6b)$$

where v_L = velocity of compressional wave propagation in an unbounded medium, and v_R = velocity of rod mode of propagation, one can write both equations of motion in the form

$$(1/v^2)(\partial^2 u/\partial t^2) = (\partial^2 u/\partial x^2) - \beta(\partial\theta/\partial x). \quad (2.7)$$

R. M. White

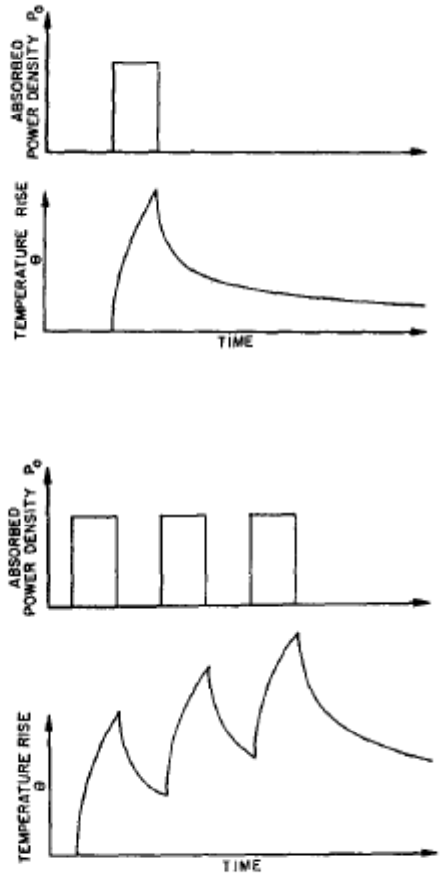

FIG. 2. Top: single rectangular pulse absorbed at a surface and the resultant transient temperature rise. Bottom: three rectangular pulses and resultant rise in surface temperature.

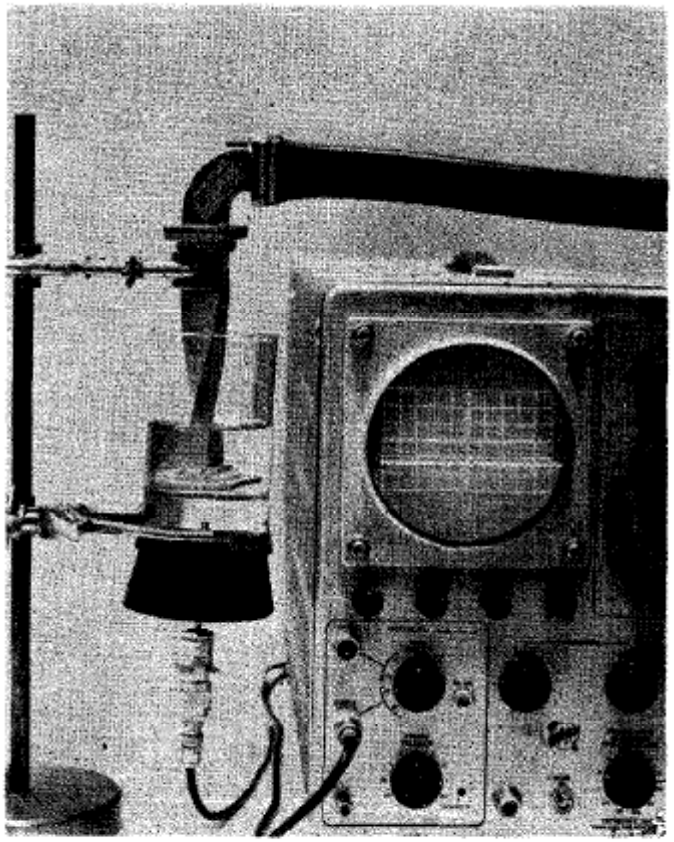

FIG. 3. Generation of elastic waves at the surface of a liquid by the absorption of an rf pulse. A 9-kMc/sec, 2-μsec rf pulse is partially absorbed at the surface of the tap water inside the waveguide (the water level inside the waveguide is the same as that outside). The compressional wave produced is detected by the piezoelectric probe mounted in the stopper at the bottom of the container. The time delay between triggering of the scope (when rf pulse is produced) and the first detected acoustic signal is equal to the computed time of travel of the compressional wave from the surface of the water to the probe crystal.

IX. SUMMARY AND CONCLUSIONS

In analyzing the generation of elastic waves by transient surface heating, particularly for the case of a harmonically varying temperature, it is found that the functional dependence of the stress wave amplitude on frequency and the properties of the body heated is governed by the type of constraint applied at the heated surface, as well as by the distance, compared with the elastic wavelength, over which heating takes place.

Egge Hey, Klaus Gollnick, *Optic-Acoustic Relaxation of Periodically Irradiated Solutions, Berichte der Bunsengesellschaft für physikalische Chemie, Volume 72, Issue 2, page 263, März 1968*

Abstract

A relaxation method is described which allows a direct measurement of radiationless transition rates. The method corresponds to the spectrophone in the gas phase; i.e. it employs intensity modulated light of variable modulation frequency as the means for perturbing the equilibrium, and a microphone as the measuring device for detecting the resultant pressure wave. By applying the method to solutions of eosine in methanol the following results were obtained: 1) The rate of the radiationless transition from the first excited singlet state of eosine to the triplet state is $1.25 \cdot 10^8$ sec^{-1}. 2) Besides this transition the radiationless deactivation of the first excited singlet state to the ground state may be neglected. 3) The natural lifetime of the triplet state of eosine is 0.104 sec. 4) Even at low temperatures (-196°C) the radiationless deactivation of the triplet state is much more prominent than the radiative transition. Generalizations of the optic-acoustic relaxation method are discussed.

This article is the first reported study on photoacoustics of liquids

S. Oda, T. Sawada, and H. Kamada, Department of Industrial Chemistry, Faculty of Engineering, The University of Tokyo, Hongo, Bunkyo-ku, Tokyo, Japan, *"Determination of Ultra Trace Cadmium by Laser-Induced Photoacoustic Absorption Spectrometry"*, ANALYTICAL CHEMISTRY, **50** (7), 865 (JUNE 1978)

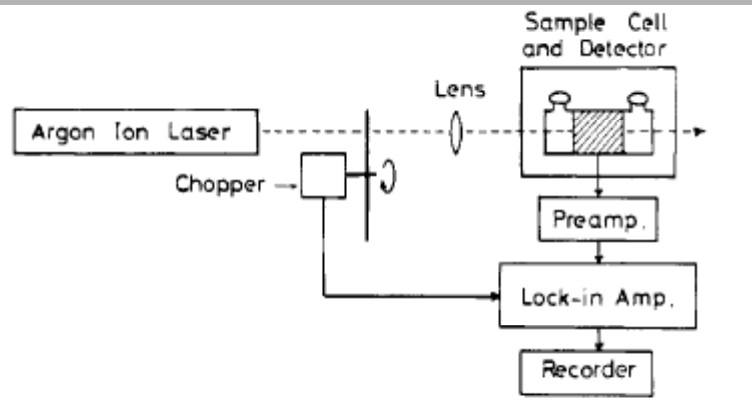

Figure 1. Block diagram of the laser-induced photoacoustic spectrometer

The pressure fluctuation induced in the sample solution by absorbed radiation was detected by a piezoelectric ceramic (NPM, N-6 supplied by Tohoku Kinzoku Co. Ltd.). A lock-in amplifier/preamplifier (NF Co. Ltd., Model LI-574) was used to amplify the modulated output signal.

Table I. Comparison of Cadmium Determinations in *Penicilium ochro-chloron* by This Method and Atomic Absorption Spectrometry

Sample No.	Cd concentration, μg/mL: This method	Cd concentration, μg/mL: A.A.S.
1	0.23	0.25
2	0.28	0.28
3	11.7	9.0
4	0.55	0.35
5	1.36	0.98

The laser-induced photoacoustic absorption method is applicable to a wide range of liquid samples and application of lasers operating in the UV, visible, and IR is recommended.

Radiative Transfer Equation in Turbid Media

J. Opt. Soc. Am. A **11** (10), 2727 (October 1994)

Boundary conditions for the diffusion equation in radiative transfer

Richard C. Haskell

Harvey Mudd College, Claremont, California 91711

Lars O. Svaasand

University of Trondheim, 7000 Trondheim, Norway

Tsong-Tseh Tsay

Beckman Laser Institute and Medical Clinic, University of California, Irvine, Irvine, California 92715

Ti-Chen Feng and Matthew S. McAdams

Harvey Mudd College, Claremont, California 91711

Bruce J. Tromberg

Beckman Laser Institute and Medical Clinic, University of California, Irvine, Irvine, California 92715

Haskel et al.

Propagation of EM waves in scattering media is described by the Boltzmann transport equation

B. Davison, *Neutron Transport Theory* (Oxford, London, 1958).

2. DIFFUSION THEORY IN RADIATIVE TRANSFER

$$\frac{1}{c}\frac{\partial L(\mathbf{r}, \hat{s}, t)}{\partial t} + \nabla \cdot L(\mathbf{r}, \hat{s}, t)\hat{s} = -(\sigma + \beta)L(\mathbf{r}, \hat{s}, t) + \sigma \iint_{4\pi} L(\mathbf{r}, \hat{s}', t) f(\hat{s} \cdot \hat{s}')\mathrm{d}\Omega' + Q(\mathbf{r}, \hat{s}, t), \quad (2.1.1)$$

where the radiance $L(\mathbf{r}, \hat{s}, t)$ has units $\mathrm{W/(m^2\ sr)}$ and where $\hat{s}$ is a unit vector pointing in the direction of interest. The linear scattering and absorption coefficients, σ and β, are the inverses of the mean free paths for scattering and absorption, respectively, and the normalized differential scattering cross section $f(\hat{s} \cdot \hat{s}')$ satisfies

$$\iint_{4\pi} f(\hat{s} \cdot \hat{s}')\mathrm{d}\Omega' = 1. \quad (2.1.2)$$

The source term $Q(\mathbf{r}, \hat{s}, t)$ represents power injected into a unit solid angle centered on $\hat{s}$ in a unit volume at $\mathbf{r}$. Equation (2.1.2) treats photons as billiard balls undergoing elastic collisions and traveling through the medium at speed $c = (3 \times 10^8\ \mathrm{m/s})/n$, where n is the refractive index of the medium (typically $n = 1.40$ for biological tissues[17]). Interference effects of photons are assumed to average to zero. In essence, Eq. (2.1.1) provides a mathematical accounting of incoherent photons.

The similarity of transport equation (2.1.1) to a continuity equation is emphasized by integration over all solid angles and use of the definitions of the fluence rate ϕ and the flux $\mathbf{j}$:

$$\frac{1}{c}\frac{\partial \phi(\mathbf{r}, t)}{\partial t} + \nabla \cdot \mathbf{j}(\mathbf{r}, t) = -\beta\phi(\mathbf{r}, t) + S(\mathbf{r}, t),$$

where

$$S(\mathbf{r}, t) \equiv \iint_{4\pi} Q(\mathbf{r}, \hat{s}, t)\mathrm{d}\Omega,$$

$$\phi(\mathbf{r}, t) \equiv \iint_{4\pi} L(\mathbf{r}, \hat{s}, t)\mathrm{d}\Omega,$$

$$\mathbf{j}(\mathbf{r}, t) \equiv \iint_{4\pi} L(\mathbf{r}, \hat{s}, t)\hat{s}\mathrm{d}\Omega. \quad (2.1.3)$$

When scattering is much stronger than absorption ($\sigma_{\mathrm{tr}} \gg \beta$), the radiance can be expressed as an isotropic fluence rate ϕ plus a small directional flux $\mathbf{j}$, and transport equation (2.1.1) reduces to a diffusion equation.[5,13–16] We first write the radiance as

$$L(\mathbf{r}, \hat{s}, t) = \frac{1}{4\pi}\phi(\mathbf{r}, t) + \frac{3}{4\pi}\mathbf{j}(\mathbf{r}, t) \cdot \hat{s}. \quad (2.1.4)$$

Substituting this diffusion approximation into Eq. (2.1.1) and then multiplying by $\hat{s}$ and integrating over all solid angles yields

$$\frac{1}{c}\frac{\partial \mathbf{j}(\mathbf{r}, t)}{\partial t} = -\frac{1}{3}\nabla\phi(\mathbf{r}, t) - \frac{1}{3D}\mathbf{j}(\mathbf{r}, t),$$

where

$$D = \frac{1}{3[(1-g)\sigma + \beta]} = \frac{1}{3\sigma_{\mathrm{tr}}} = \frac{l_{\mathrm{tr}}}{3}, \quad (2.1.5)$$

where D is the photon-diffusion coefficient, g is the average cosine of the scattering angle, $\sigma_{\mathrm{tr}} = (1 - g)\sigma + \beta$ is the linear transport coefficient, and $l_{\mathrm{tr}} = 1/\sigma_{\mathrm{tr}}$ is the transport mean free path.

Haskel et al.

$$\mathbf{j}(\mathbf{r}, t) = -D\nabla\phi(\mathbf{r}, t).$$

Fick's law valid for isotropic source term Q

$$D\nabla^2\phi(\mathbf{r}, t) - \beta\phi(\mathbf{r}, t) = (1 + 3D\beta)\frac{1}{c}\frac{\partial\phi(\mathbf{r}, t)}{\partial t} - S(\mathbf{r}, t) + \frac{3D}{c^2}\frac{\partial^2\phi(\mathbf{r}, t)}{\partial t^2} - \frac{3D}{c}\frac{\partial S(\mathbf{r}, t)}{\partial t}. \quad (2.1.7)$$

For most biological tissues the scattering and absorption coefficients are in the range $10/\text{cm} < \sigma_{tr} < 50/\text{cm}$ and $0.03/\text{cm} < \beta < 0.15/\text{cm}$ [*in vivo*, and with $\lambda \cong 650$ nm (Refs. 18 and 19)], so $3D\beta \ll 1$. If the source varies in time with frequencies of less than ~1 GHz, then the last two terms in Eq. (2.1.7) can also be neglected,[20] leaving the diffusion equation

$$D\nabla^2\phi(\mathbf{r}, t) - \beta\phi(\mathbf{r}, t) = \frac{1}{c}\frac{\partial\phi(\mathbf{r}, t)}{\partial t} - S(\mathbf{r}, t). \quad (2.1.8)$$

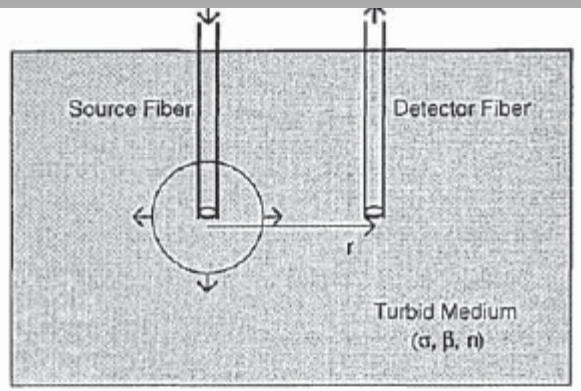

Fig. 1. Infinite-medium geometry. The medium is strongly scattering with scattering coefficient σ, absorption coefficient β, and refractive index n. The detector fiber is oriented perpendicular to the radial flux from the source, so the detector signal is simply proportional to the fluence rate.

Y. Fan, A. Mandelis, G. Spirou, I. A. Vitkin, and W. M. Whelan, *"Laser photothermoacoustic heterodyned lock-in depth profilometry in turbid tissue phantoms"*, PRE **72** (5), 051908, 2005

- Frequency-domain radiative transfer boundary-value problem

diffuse photon density wave (DPDW, or *diffuse radiant energy fluence rate*) field [13], ψ_d [W m^{-2}]:

$$\frac{\partial^2}{\partial z^2}\psi_d(z,\omega) - \sigma_p^2\psi_d(z,\omega) = I_0' e^{-\mu_t(z+L)}, \quad -L \leqslant z \leqslant 0.$$

$$\mu_t = \mu_s + \mu_a. \qquad (1)$$

$$I_0' = -\frac{I_0\mu_s}{D}\left(\frac{\mu_t + g\mu_a}{\mu_t - g\mu_s}\right), \quad D = \frac{1}{3[\mu_a + (1-g)\mu_s]},$$

The complex diffuse-photon wave number is defined as [15]

$$\sigma_p = \sqrt{\frac{1 - i\omega\tau_a}{D_{eff}\tau_a}}, \qquad (4)$$

where

$$D_{eff} = \nu D = \frac{\nu}{3[\mu_a + (1-g)\mu_s]}, \quad \tau_a = (\nu\mu_a)^{-1}.$$

Here ν is the speed of light ($\approx 10^{10}$ cm/s for light propagating in turbid media); D is the optical diffusion coefficient, in units of length.

$$\psi_d(-L,\omega) - A\frac{\partial}{\partial z}\psi_d(-L,\omega) = -3\mu_s g A I_0,$$

$$\psi_d(0,\omega) + A\frac{\partial}{\partial z}\psi_d(0,\omega) = 3\mu_s g A I_0 e^{-\mu_t(z+L)}, \qquad (7)$$

where $A = 2D(1+r_{21})/(1-r_{21}) \equiv 2D\xi$. r_{21} is the internal reflectance, defined as the ratio of the upward-to-downward hemispherical diffuse optical fluxes at the boundary.

OPTOACOUSTIC TOMOGRAPHY

V.E. Gusev and A. A. Karabutov, "Laser Optoacoustics" Transl. by K. Hendzel, AIP Press, 1993, New York, Chap. 2.2, The transfer function method. (see next slide)

A. A. Karabutov and O. B. Ovchinnikov, [Shipbuilding Industry] Acoustics Series ("RUMB", Leningrad, 1987), No. 2, p. 93.

L. V. Burmistrova, A. A. Karabutov, A. I. Portnyagin, O. V. Rudenko and E. B. Cherepetskaya, "Method of transfer functions in problems of thermooptical sound generation", Sov. Phys. Acoust. 24 (5), pp. 369 – 374, Sept. – Oct. 1978

These theoretical results and their experimental implementations confirming the theoretical predictions form the background of the current laser optoacoustic tomographic technologies for biomedical applications. The following slide shows the formalism and first experimental application of the spatial distribution of the optical absorption coefficient recovery from measurements of the temporal profiles of laser-generated acoustic pulses.

se Eq. (2.35) to analyze thermoelastic sound generation for the case where bsorption is dependent on the coordinate: $\alpha = \alpha(z)$. The acoustic wave can be represented as

$$\frac{\partial G(t,z)}{\partial t} = -\frac{c_0^2\beta}{c_p} I_0 f(t) \frac{d}{dz}\left[\exp\left(-\int_0^z \alpha(\xi)d\xi\right)\right].$$

hen obtain for traveling acoustic wave (2.36) in the rigid boundary case

$$v_r(\tau) = \frac{\beta I_0}{\rho_0 c_p} \int_{-\infty}^{\infty} \tilde{f}(\omega) e^{-i\omega\tau} d\omega \int_0^{\infty} \cos\left(\frac{\omega}{c_0}\xi\right) g(\xi) d\xi, \qquad (2.37)$$

(ξ) describes the spatial distribution of the sources G.

$$v_f(\tau) = \frac{\beta I_0}{\rho_0 c_p} \int_{-\infty}^{\infty} \tilde{f}(\omega) e^{-i\omega\tau} d\omega \int_0^{\infty} \sin\left(\frac{\omega}{c_0}\xi\right) g(\xi) d\xi. \qquad (2.38)$$

tions (2.37) and (2.38) can be generalized by continuing the source func-) (this function is defined only for $z > 0$) into the domain $z < 0$ either oddly ree boundary $\bar{g}_f(-z) = -\bar{g}_f(z)$], or evenly (for a rigid boundary) $= \bar{g}_r(z)$. Taking this into account

$$v = \frac{\beta I_0}{2\rho_0 c_p} \int_{-\infty}^{\infty} \tilde{f}(\omega) e^{-i\omega\tau} d\omega \int_{-\infty}^{\infty} e^{-i\omega\tau} \bar{g}(\xi) d\xi, \qquad (2.39)$$

(z) is the corresponding continuation. Therefore the thermooptical transfer is the Fourier transform of the spatial distribution of the thermal sources. words, the OA-signal spectrum is the product of the laser radiation density n and the Fourier spectrum of the spatial distribution of absorption (taking inuation into account).

is the fundamental result from using the transfer function method. The function and the spatial distribution of optoacoustic sources can be recov- m the known light intensity spectrum (the laser pulse wave form) and the d spectrum of the acoustic signal. This technique was implemented in Ref. laser pulses of sufficiently short duration are used and when the spectrum broader than the range of the transfer function, the leading edge of the pulse mimics the source distribution:[3]

$$v \sim \alpha(z - c_0 t)\exp\left(-\int_0^{z-c_0 t} \alpha(\xi)d\xi\right), \quad z > c_0 t.$$

$z)$ can be determined from this equation. Figure 2.9 shows the results of ents to recover the absorption distribution in a model medium.[8] Such ex- ts have demonstrated that recovery is possible to a depth z of the order of cal thickness of the medium

$$\int^z \alpha(\xi)d\xi \approx 2 - 3.$$

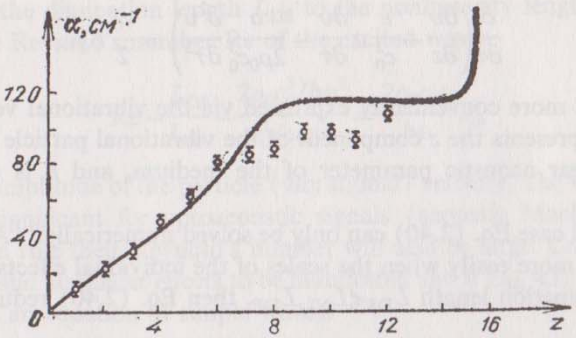

FIG. 2.9. OA diagnostics of an inhomogeneously absorbing medium. Solid curve—absorptio vs depth; circles—experiment; z—number of absorbing layer.

single laser pulse.[3] In some sense this is the inverse of the previous c technique has also been implemented experimentally in Ref. 8.

It should be pointed out that in many versions of OA spectroscopy a acoustic wave is not measured but rather different characteristics of the fi excitation region are measured. We will nonetheless represent their tempo trum as the product of the radiation intensity spectrum and a certain f function independent of the type of radiation modulation. The transfer method is therefore also applicable in these modifications of optoacoustic copy. Some of the more commonly encountered versions will be examine

2.3. Stage-by-stage Analysis of Thermooptical Excitation of Sound

The transfer function method can be employed to find the spectrum of coustic signal to a depth of a few (3–5) absorption lengths of light α^{-1}. sound is commonly recorded at far greater distances experimentally. T neglected in the generation zone can no longer be ignored here. These inclu dissipation, finite sound amplitude, and diffraction.

As a rule, a disk-type acoustic source geometry is typical of laser opto and a stage-by-stage approach can be used to account for the cited eff approach is as follows. If the lengths over which dissipation L_{DS}, nonlinea and diffraction L_{DF} are manifested for efficiently thermooptically excited cies are much greater than the dimensions of the thermal sources

$$(\alpha L_{DS}, \alpha L_{NL}, \alpha L_{DF}) \gg 1,$$

the problem is divided into two stages. In the first stage the transfer method, for example, is employed to determine the traveling wave spec profile (see Sec. 2.2; all cited effects are not incorporated). The resulting s

Photoacoustic ultrasound (PAUS)—Reconstruction tomography

Robert A. Kruger, Pingyu Liu, Yuncai "Richard" Fang, and C. Robert Appledorn
Department of Radiology, Division of Imaging Sciences, CL-112, Indiana University Medical Center, 541 Clinical Drive, Indianapolis, Indiana 46202-5111

Med. Phys. **22** (10), 1605 (October 1995)

$$\rho C \frac{\partial T(\mathbf{r},t)}{\partial t} = \lambda \nabla^2 T(\mathbf{r},t) + S(\mathbf{r},t), \tag{1}$$

The second equation is a wave equation that relates acoustic pressure $p(\mathbf{r},t)$ to the excess temperature distribution $T(\mathbf{r},t)$:

$$\frac{\partial^2 p(\mathbf{r},t)}{\partial t^2} - v_s^2 \nabla^2 p(\mathbf{r},t) = \frac{\beta}{\kappa} \frac{\partial^2 T(\mathbf{r},t)}{\partial t^2}, \tag{2}$$

the excess pressure, $p(\mathbf{r},t)$, at position $\mathbf{r}$ and time t can be expressed as a volume integral:

$$p(\mathbf{r},t) = \frac{\beta\rho}{4\pi} \int\int\int \frac{d\mathbf{r}'}{|\mathbf{r}-\mathbf{r}'|} \frac{\partial^2 T(\mathbf{r}',t')}{\partial t'^2}, \tag{3}$$

where the volume integral is carried out over the entire $\mathbf{r}'$ space, where the temperature acceleration $\partial^2 T(\mathbf{r}',t')/\partial t'^2$ is nonzero, and $t' = t - |\mathbf{r}-\mathbf{r}'|/v_s$.

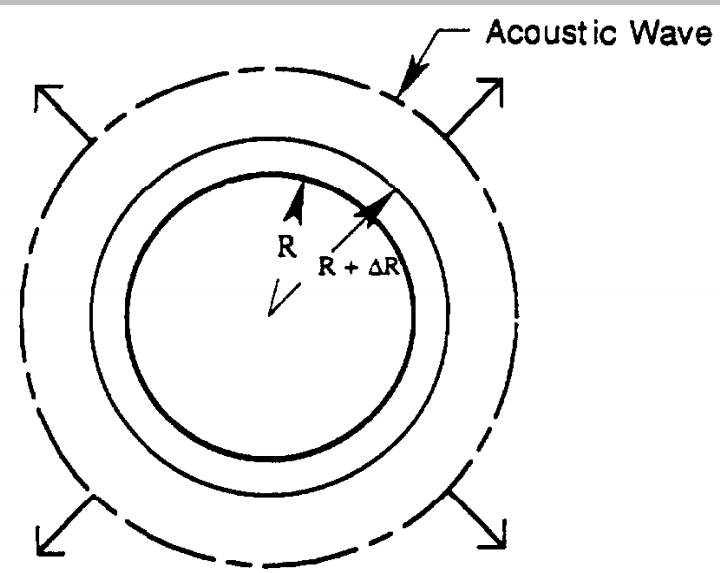

FIG. 1. A sphere of radius R expands to radius $R+\Delta R$ in time τ, creating an acoustic pressure wave.

Photoacoustic ultrasound

Robert A. Kruger
Radiology Department, Division of Imaging Science, CL-112, 541 Clinical Drive, Indiana University Medical Center, Indianapolis, Indiana 46202-5111

Med. Phys. **21** (1), 127 (January 1994)

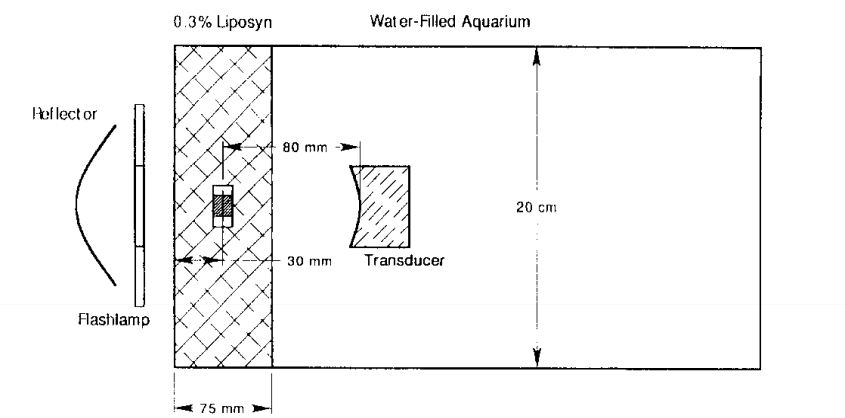

FIG. 2. Modlified aquarium for photo acoustic experiments.

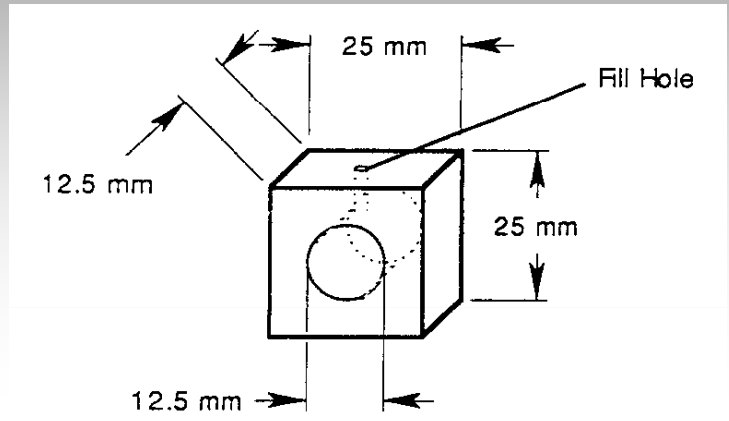

FIG. 3. Lucite absorption phantom.

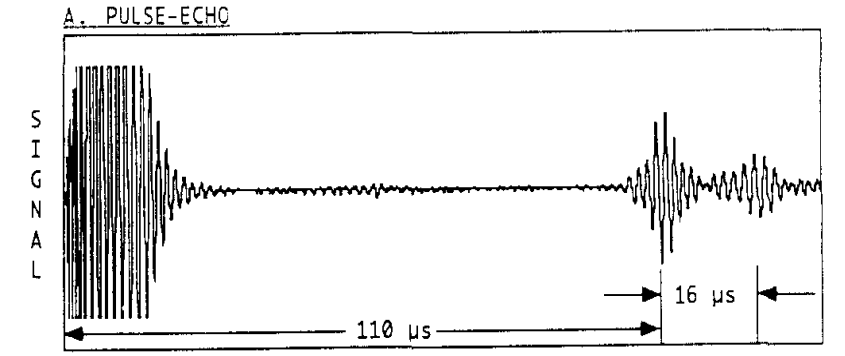

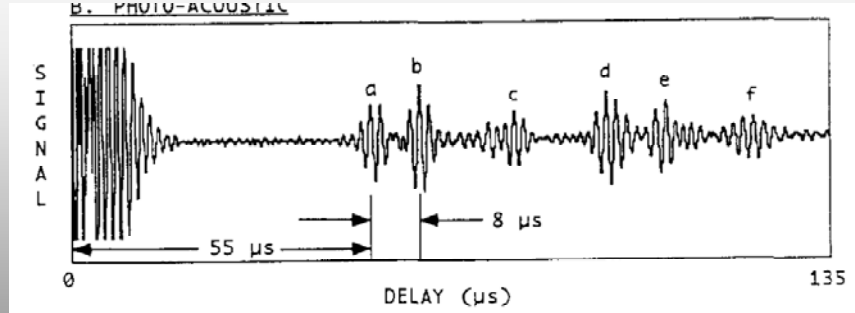

FIG. 6. Lateral response of PA signal to absorption by the phantom illustrated in Fig. 3.

Blood (hemoglobin) spectrum determination using PT or PA spectroscopy

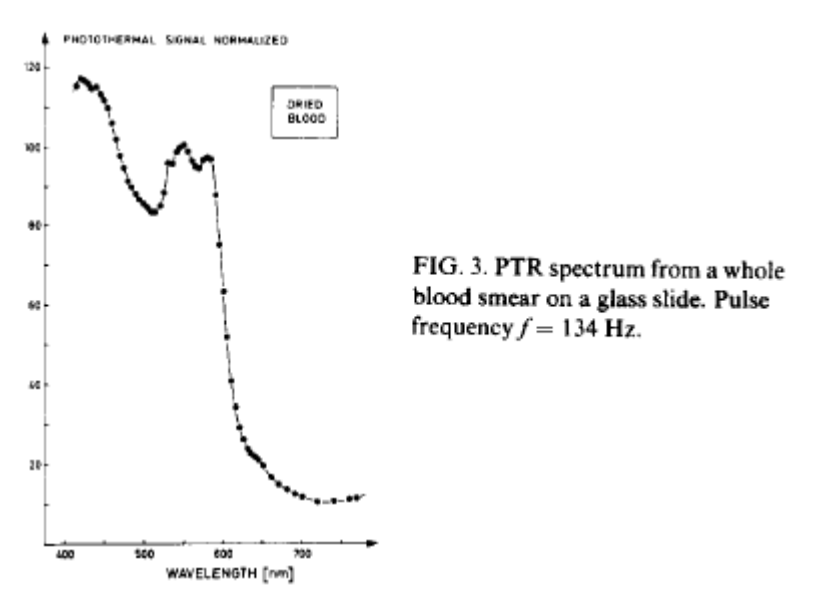

FIG. 3. PTR spectrum from a whole blood smear on a glass slide. Pulse frequency $f = 134$ Hz.

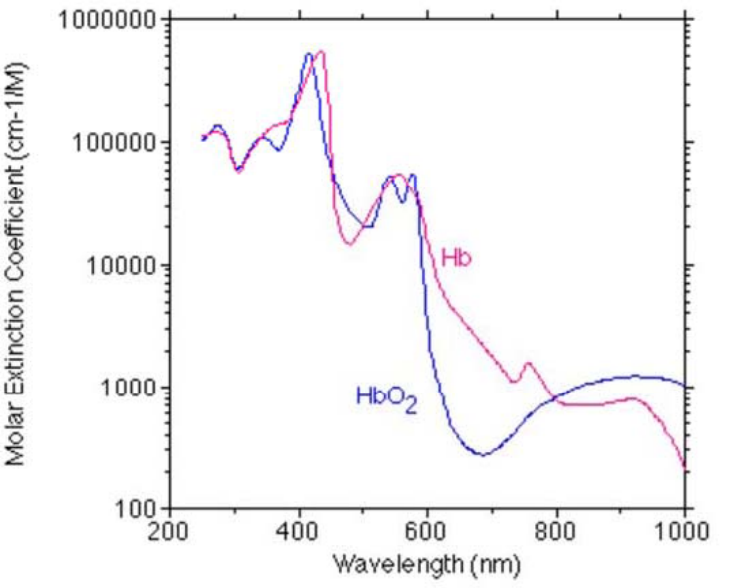

- Per-Erik Nordal and Svein Otto Kanstad, Laser and Applied Optics Laboratory, P. 0. Box No. 303 Blindern Oslo 3, Norway, *"Visible-light spectroscopy by photothermal radiometry using an incoherent source",* Appl. Phys. Lett. **38** (7), 486 (April 1981).

Scott Prahl, Oregon Medical Laser Center, *"Optical Absorption of Hemoglobin",* http://omlc.ogi.edu/spectra/hemoglobin/ (15 December 1999)

A. A. Oraevsky [1,2] S. L. Jacques [1,2] F. K. Tittel[2], *"Determination of tissue optical properties by piezoelectric detection of laser-induced stress waves"*
1. Laser Biology Research Lab. Box 17, UT/M.D. Anderson Cancer Center,
1515 Holcombe boulevard, Houston TX 77030
2. Department of Electrical and Computer Engineering, P.O. Box 1892
Rice University, Houston TX 77251
SPIE Laser-Tissue Interaction IV, **1882,** 86 (1993)

"A technique is described for the measurement of optical properties in clear and turbid media based on time-resolved detection of acoustic transients. Thermal expansion of the irradiated volume of a sample heated by short laser pulses causes a pressure-rise that is proportional to the laser fluence and the absorption coefficient in the sample".

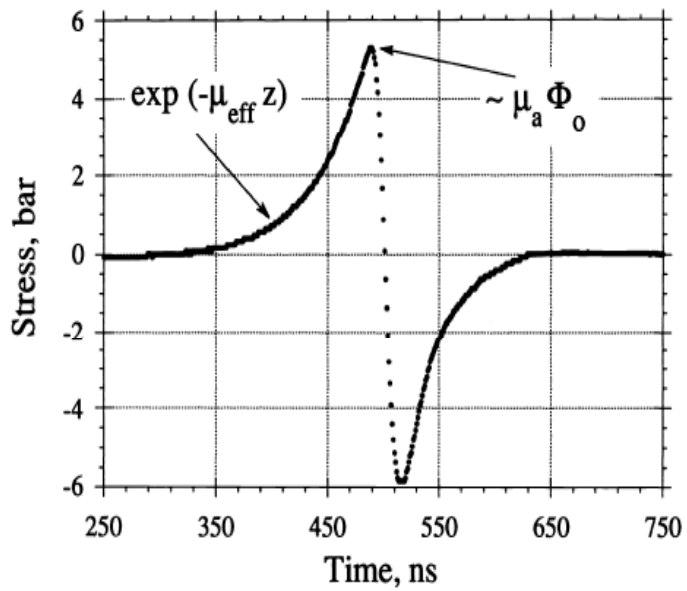

FIGURE 1. The profile of acoustic signal generated by a 14-ns pulse of Nd:YAG laser at 355 nm in potassium chromate aqueous solution. The surrounding medium is air that creates "free" boundary at the surface of irradiated medium.

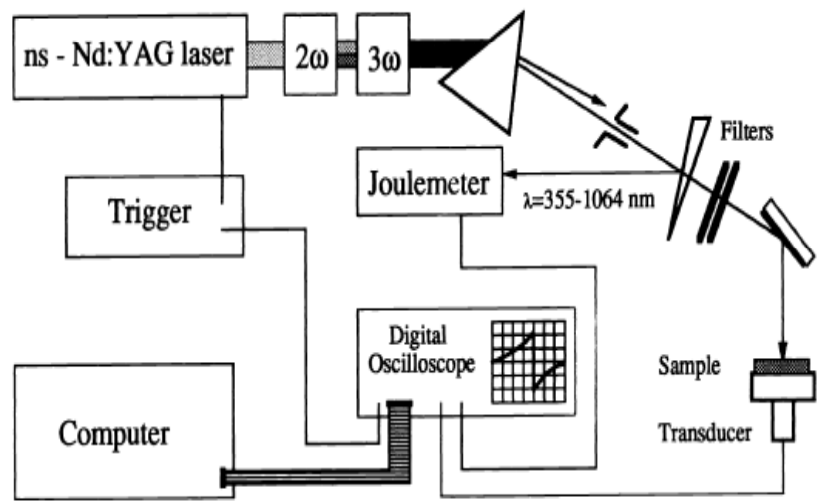

FIGURE 6. Experimental set-up for time resolved detection of laser induced acoustic waves.

the pressure distribution generated in the sample. The actual acoustic pulse profile formed by the laser pulse profile, L(t), can be calculated as the convolution of the instant spatial distribution of the thermoelastic sources moving into the media and temporal intensity envelope of deposited laser energy:

$$P(t) = \Gamma C_s \mu_a I_0 \int_{-\infty}^{+\infty} L(t) \exp(-\mu_a C_s |t - \tau_L|)\, dt \qquad (11)$$

A. A. Oraevsky, S. L. Jacques, F. K. Tittel, A. A. Oraevsky, SPIE Laser-Tissue Interaction IV, **1882**, 86 (1993)

Table 1. Optical properties of soft tissues *in vitro* measured at three wavelengths of Nd:YAG laser.

OPTICAL PROPERTY	BEEF LIVER			DOG PROSTATE			ADVANCED FIBROUS ATHEROMA		
Wavelength	1064	532	355	1064	532	355	1064	532	355
$R_{d\infty}$	0.32	0.06	0.05	0.60	0.285	0.205	0.45	0.285	0.165
μ_{eff}, cm^{-1}	2.0	27.8	72.2	0.8	13.7	39.4	1.45	20.4	66.2
μ_a, cm^{-1}	0.3	11.5	31.5	0.05	2.4	9.2	0.15	3.6	17.7
μ'_s, cm^{-1}	4.0	10.9	23.6	4.2	23.8	47.1	4.5	34.8	64.9

- $R_{d\infty}$: total diffuse reflectance from optically thick samples
- μ_{eff} , which includes absorption and scattering:

$$\mu_{eff} = (3\mu_a*(\mu_a+\mu'_s))1/2$$

A. A. Oraevsky, S. L. Jacques, and F. K. Tittel, *"Measurement of tissue optical properties by time-resolved detection of laser-induced transient stress",* Appl. Opt. **36** (1), 402 (January 1997).

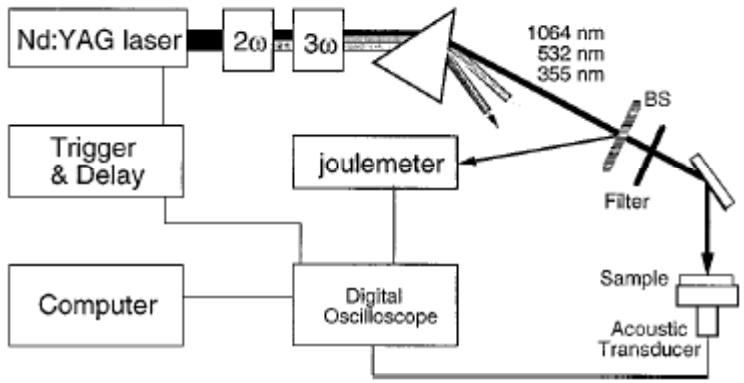

Fig. 1. Experimental setup for laser-induced thermoelastic stress detection. BS, beam splitter.

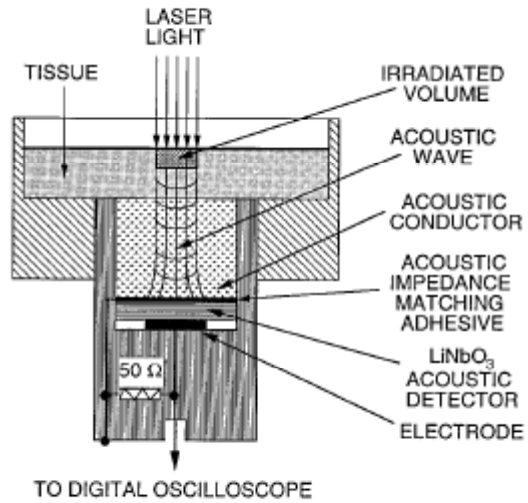

Fig. 2. General scheme of acoustic transducer.

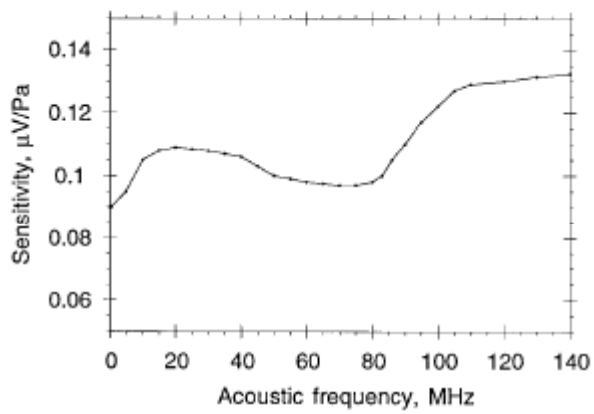

Fig. 3. Sensitivity of the lithium niobate acoustic transducer (WAT-04) as a function of frequency of the pressure waves propagating in the acoustic conductor. Calibration was performed on the basis of differential ultrasonic frequency spectra of a reference signal and a signal detected by a WAT-04 transducer.

A. A. Oraevsky, S. L. Jacques, and F. K. Tittel, *"Measurement of tissue optical properties by time-resolved detection of laser-induced transient stress"*, Appl. Opt. **36** (1), 402 (January 1997).

$$\Delta P = \frac{1}{\gamma}\frac{\Delta V}{V} = \frac{1}{\gamma}\beta\Delta T$$
$$= \frac{1}{\gamma}\frac{\beta E_{abs}(z)}{\rho C_v} = \frac{\beta c_s^2}{C_p} H\mu_a = \Gamma H \mu_a, \qquad (1)$$

where $\gamma[\mathrm{Pa}^{-1}]$ is the thermodynamic coefficient of isothermal compressibility (4.59×10^{-5} bar^{-1} for water):

$$\gamma = \frac{1}{\rho c_s^2}\frac{C_p}{C_v}, \qquad (2)$$

where c_s(m/s) is the sound velocity in the medium, ΔV(cm^3) is the volume increase caused by the thermal expansion, V is the laser-irradiated volume initially at room temperature, ρ[g/cm^3] is the density of a medium, C_p(J/gK) is the heat capacity at constant pressure, and C_v is the heat capacity at constant volume. The pressure increase is proportional to the thermal coefficient of volume expansion β [K^{-1}] of the given medium, and the absorbed energy density E_{abs} [J/cm^3], which in turn equals the product of the laser fluence H (J/cm^2) and the absorption coefficient of the medium μ_a (cm^{-1}).

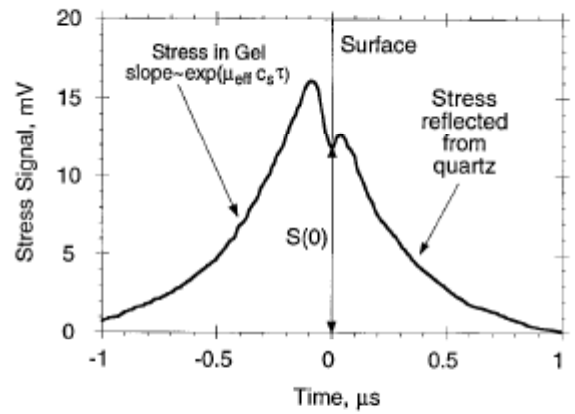

Fig. 9. Acoustic signal profile induced by a 14-ns Nd:YAG laser pulse in a turbid gel. The top medium is quartz that creates a rigid boundary at the surface of irradiated gel colored with potassium chromate and made turbid with polystyrene microspheres.

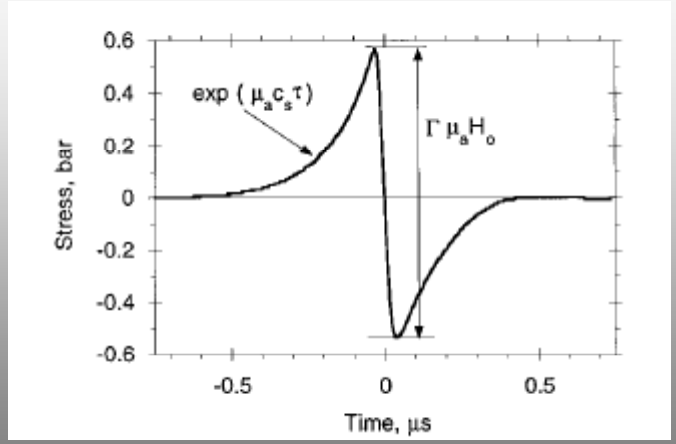

Free boundary at the surface of the irradiated medium

Photoacoustic Tomography

L.V. Wang, Optical Imaging Laboratory - Washington University in St. Louis website -I

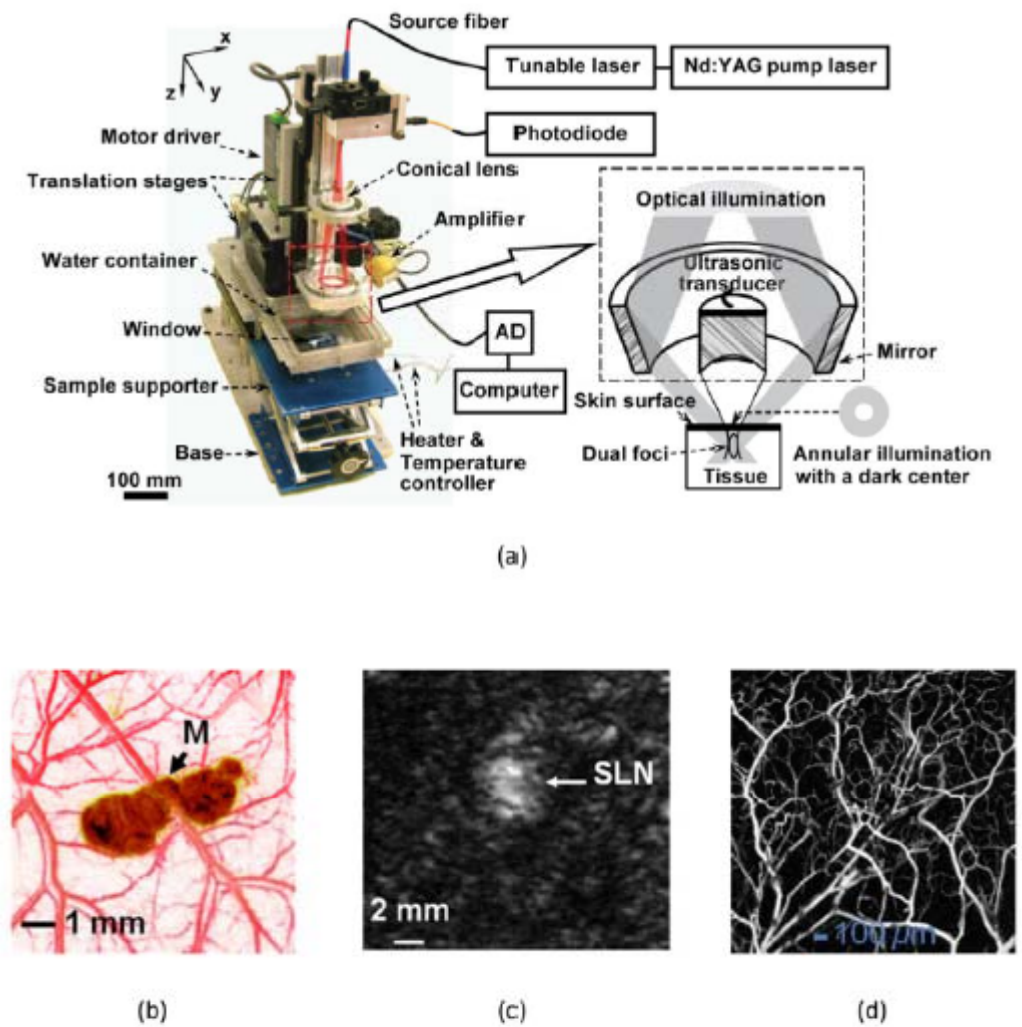

Focusing light through an objective lens with a numerical aperture of 0.1 yields a 5 μm lateral resolution, which is limited by the optical focal diameter. Such a resolution allows *in vivo* imaging of capillaries—the smallest blood vessels—as shown in Fig. 1(d), where single files of red blood cells are imaged.

Photoacoustic macroscopy: 144 μm axial resolution, 30 mm depth

The image resolution and the penetration limit are scalable with the ultrasonic frequency. For example, employing a 5-MHz ultrasonic transducer and an 804-nm near-infrared light source scaled the penetration to 30 mm, whereas the resolution is scaled up to 144 and 560 μm in the axial and lateral directions, respectively.

An *in vivo* image of a rat overlaid with additional tissue was acquired with this system [Fig. 1(c)], where the SLN accumulated injected dye through the lymphatics

Photoacoustic Tomography

L.V. Wang, Optical Imaging Laboratory - Washington University in St. Louis
website -II

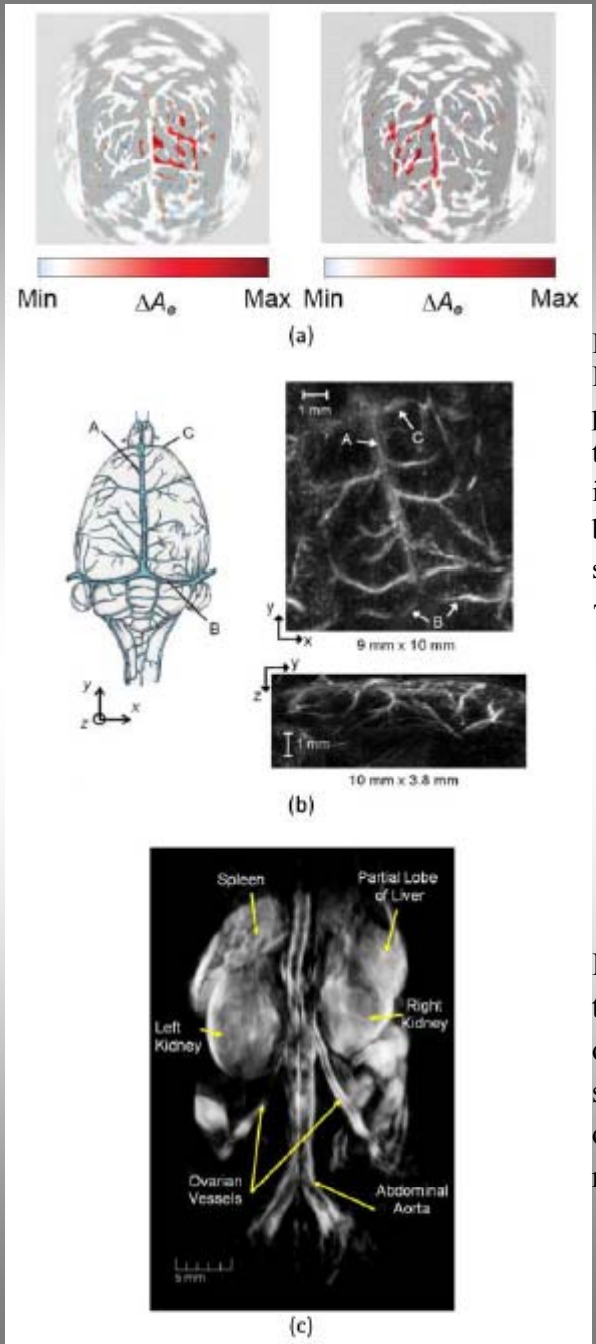

Planar-view computed tomography: Fabry-Perot detection array

In planar-view photoacoustic computed tomography, ultrasonic detection follows a plane. Optical interferometry, instead of the piezoelectric effect, can be used to sense the ultrasonic displacement or pressure. When a solid planar Fabry-Perot interferometer was constructed, a dielectric or polymer spacer was sandwiched between a pair of mirrors. A focused laser beam was optically scanned across the surface of the interferometer.

Then, an inverse algorithm was used to reconstruct a photoacoustic image [Fig. 2(b)].

Spherical-view computed tomography: rotation of object and detection by arc array

In a recently constructed small-animal whole-body photoacoustic tomography system, the animal, immersed in coupling liquid, is rotated inside a virtual spherical surface, on which a concave arc-shaped array of 64 piezo-composite ultrasonic transducers is situated. Two expanded counter-propagating laser beams illuminate the small animal orthogonally to the plane of the array. At 755 nm wavelength, the internal organs of a nude mouse were imaged [Fig. 2(c)].

Photoacoustic Tomography

L.V. Wang, Optical Imaging Laboratory - Washington University in St. Louis website -III

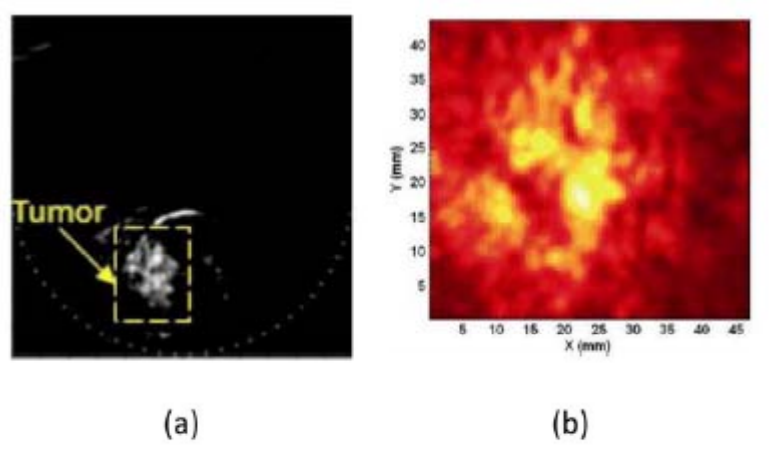

Photoacoustic breast imaging

PAT lends itself to breast imaging. Breast tissue has relatively homogeneous (~±5%) speed of sound, and breast tumors tend to present higher total blood concentrations and lower oxygen saturations of hemoglobin than surrounding tissues. Figure 3(a) shows an *in vivo* photoacoustic image of a human breast,where the ultrasonic detection follows an arc. The imaged lesion measured ~18 mm and centered at 23 mm deep from the laser-illumination surface; it was confirmed by biopsy to be an invasive carcinoma. Figure 3(b) shows another *in vivo* photoacoustic image of a human breast, where the ultrasonic detection follows a plane. The lesion was identified as a ring-shaped structure having an average optical absorption contrast of 1.6 relative to the background. The lesion was estimated to be 30 mm in diameter, which matched the pathologically estimated size (26 mm).

Progress in PA Imaging Instrumentation: Frequency-domain biomedical photoacoustics – The Photoacoustic Radar/Sonar

A. Mandelis, A. Vitkin, S. Telenkov and Y. Fan, US patent 7,525,661 B2, Issued: April 28, 2009; S. Telenkov and A. Mandelis, JBO **11** (4), 044006 (July/August 2006)

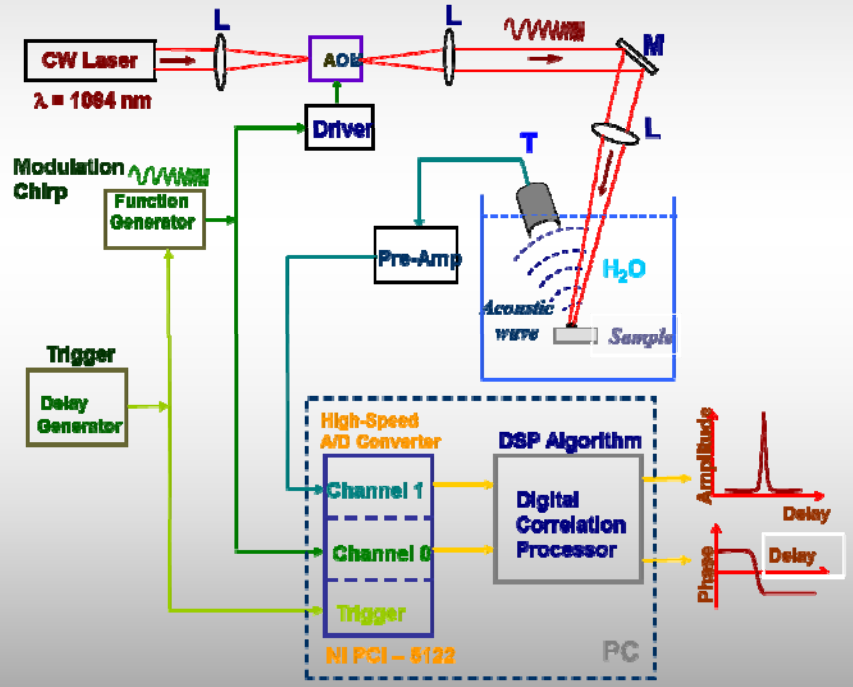

Two signal generation modalities for FD Photoacoustics:

Correlation Processing (Matched Filter Compression)

Heterodyne Mixing with Coherent Detection

Frequency-Swept FD-PA Radar

Heterodyne Mixing and Coherent Detection

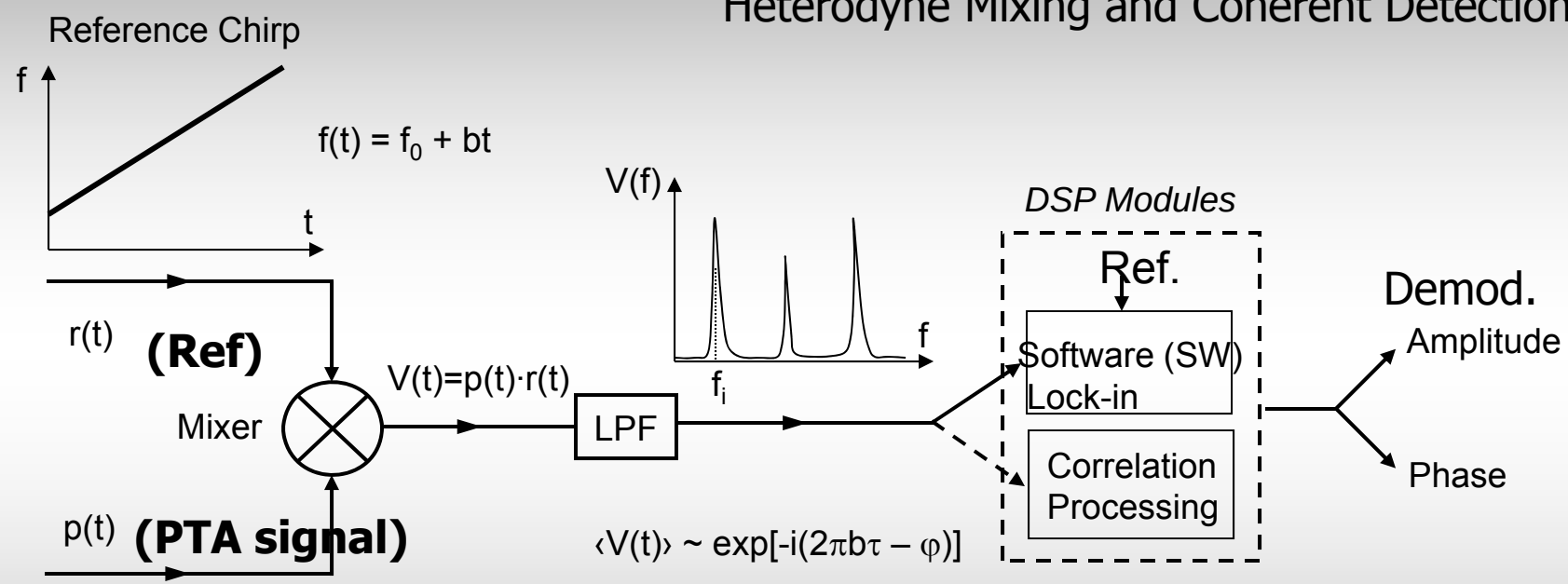

$\langle V(t) \rangle \sim \exp[-i(2\pi b\tau - \varphi)]$

ϕ : phase lag due to acoustic delay

Heterodyne signal contains frequency components proportional to the chromophore depth:

$f_i = b\tau_i = b(z_i/c_a)$, c_a – speed of sound

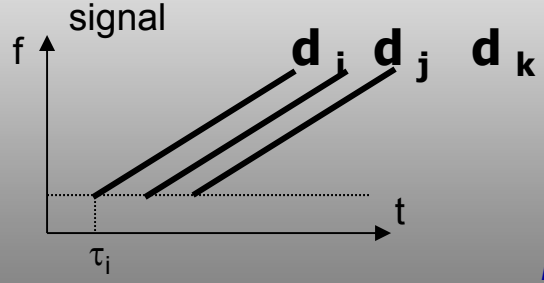

$p_i(t) = A_i \exp(i2\pi f(t - \tau_i)t + \varphi)$

FD-PA with linear frequency modulation relates signal spectrum to the depth d_i of subsurface chromophores.

τ_i : Characteristic response time of chromophore at $d_i = c_a \tau_i$

DSP Algorithms for FD-PTA Imaging

Correlation Processing (Matched Filter Compression) - Photoacoustic RADAR

1. Digital correlation processor with quadrature demodulation.
(Records multiple chirps, averages and time-shifts post-processing) – SLOW!

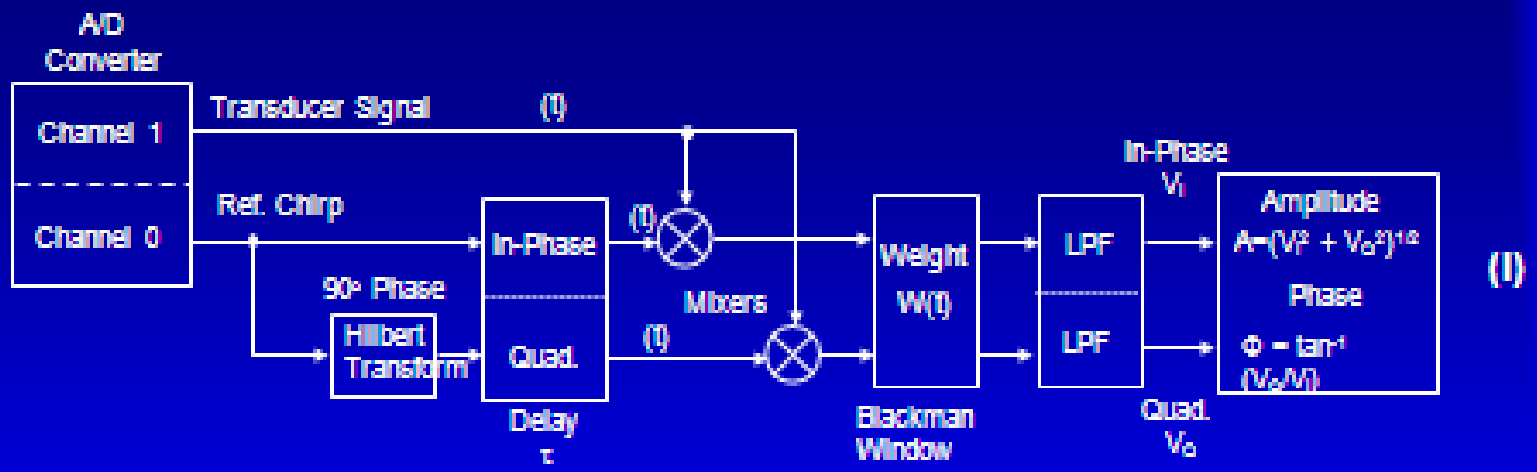

(I)

2. Fourier-domain cross-correlation processing (FD mixing) – FAST!

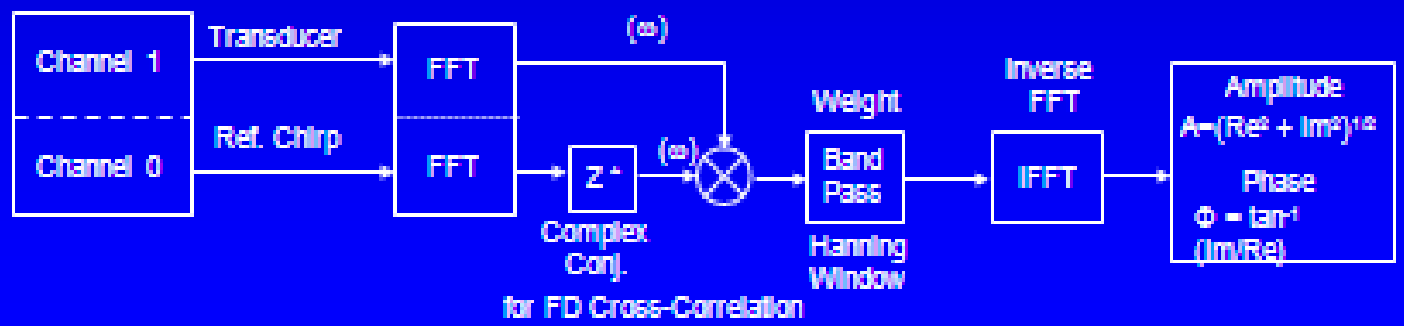

(II)

System Autocorrelation Function

Configuration (I)

Frequency sweep: 1 – 5 MHz
Sweep duration: 1 ms
Reference signal delay time: 30 μs

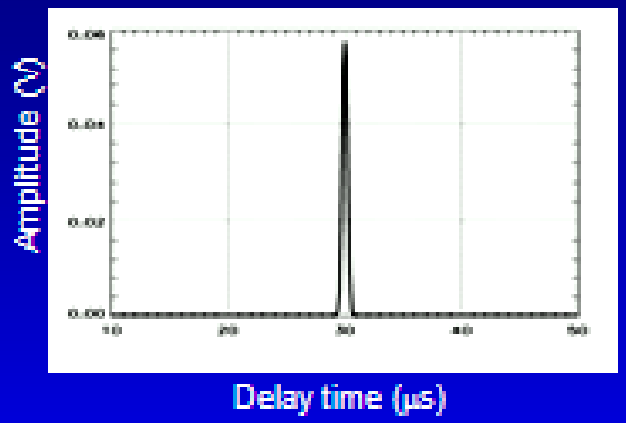

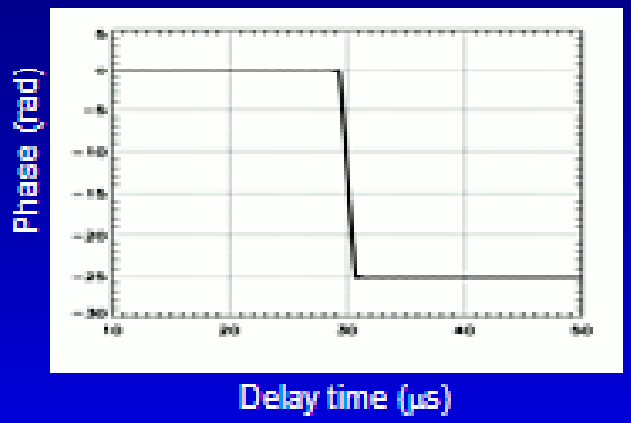

FWHM = 0.5 μs, ΔL = 0.74 mm at $c_a = 1.48 \cdot 10^5$ cm/s

Delay time is equivalent to depth $z = c_a \cdot \tau$, therefore FD-PTA system can be used for single-point depth selectivity or 2-D and 3-D imaging of subsurface tissue chromophores.

3-D FD-PTA Depth-Selective Imaging of Tissue

Sample: Chicken breast with embedded disc-shaped gel inclusion (μ_a = 4 cm^{-1}).

Frequency sweep: 1 – 5 MHz

Fixed depth images of the 3-D volume

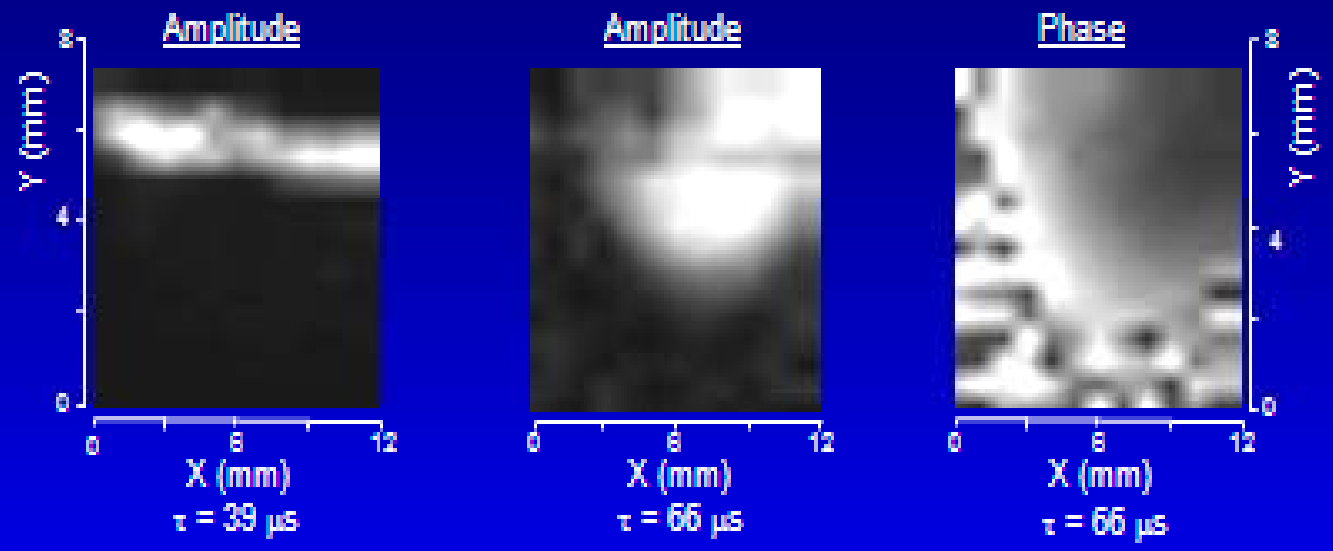

Sample Geometry

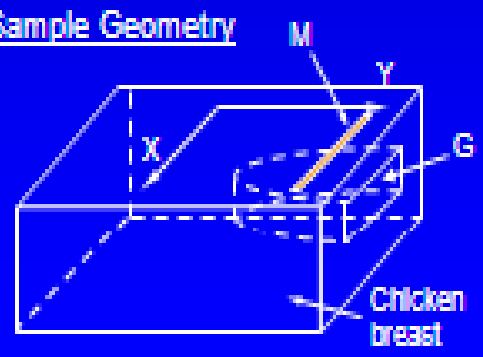

M – Black ink marker
G – Gel inclusion

Axial resolution comparison, Images:

The sample is a 1 mm layer of plastisol (μ_a=9 cm^{-1}) separated from a thick plastisol with a transparent layers of tape (~0.9 mm).

The absorbers are located in 1 cm of Intralipid solution.

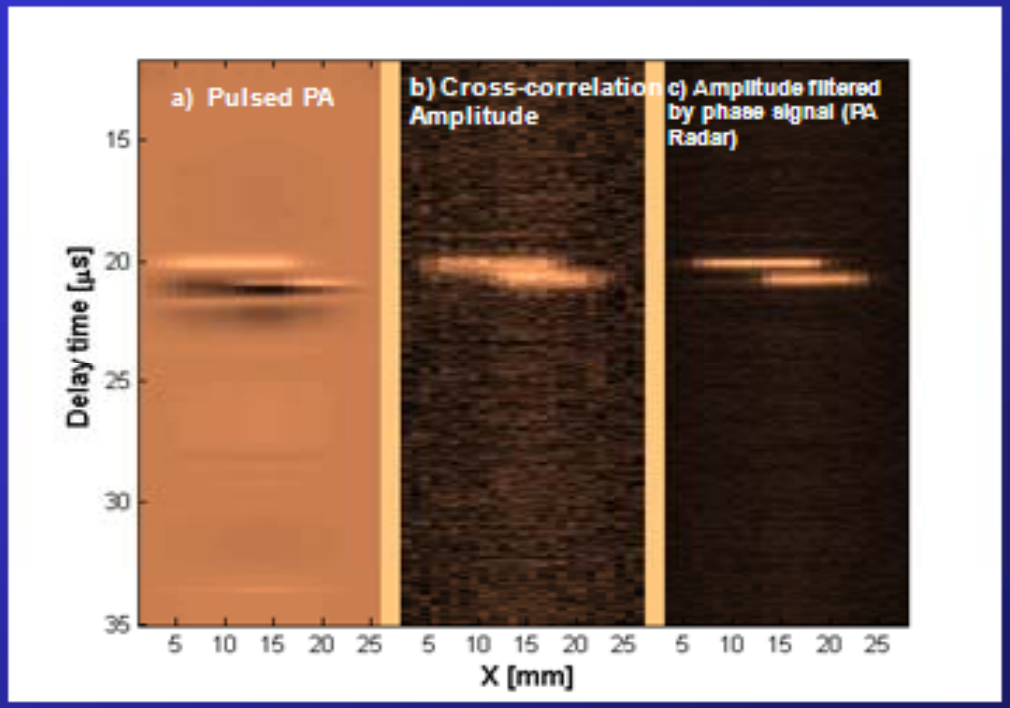

20

PA Radar Ultrasonic B-mode imaging using phased arrays

Image is formed using a set of ultrasound beams with direction controlled by delay time applied to individual transducer sensors

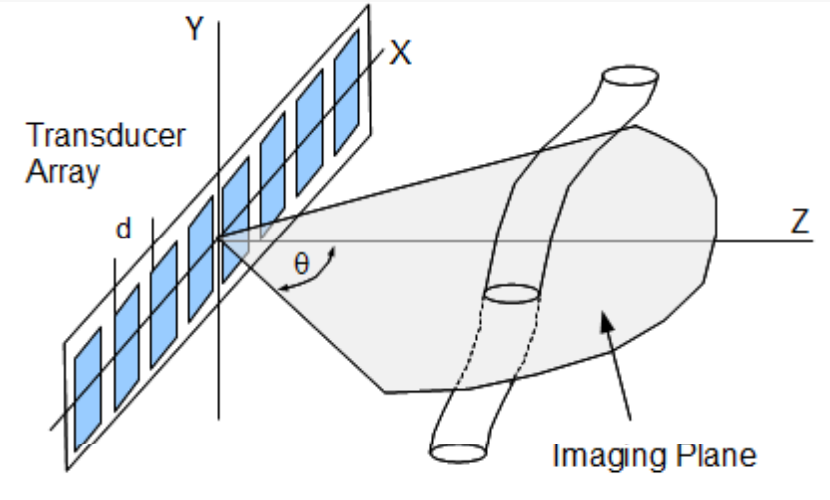

Beam steering is dynamic without any mechanical scans

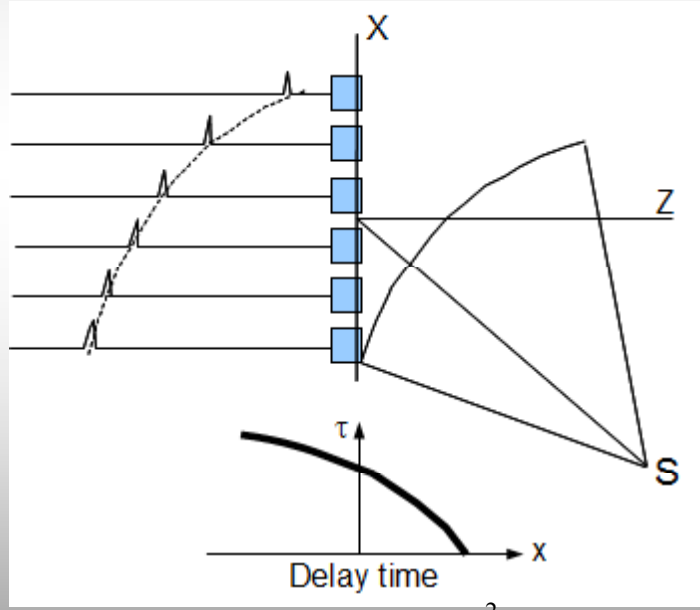

$$\tau_n = \frac{x_n \sin\theta}{c_a} - \frac{x_n^2}{2c_a r}$$

Phased array PA correlation of small animal

Small animal (rat) with intramuscular tumor implanted.
Superficial and deep (~ 1cm) blood vessels at tumor position are visible

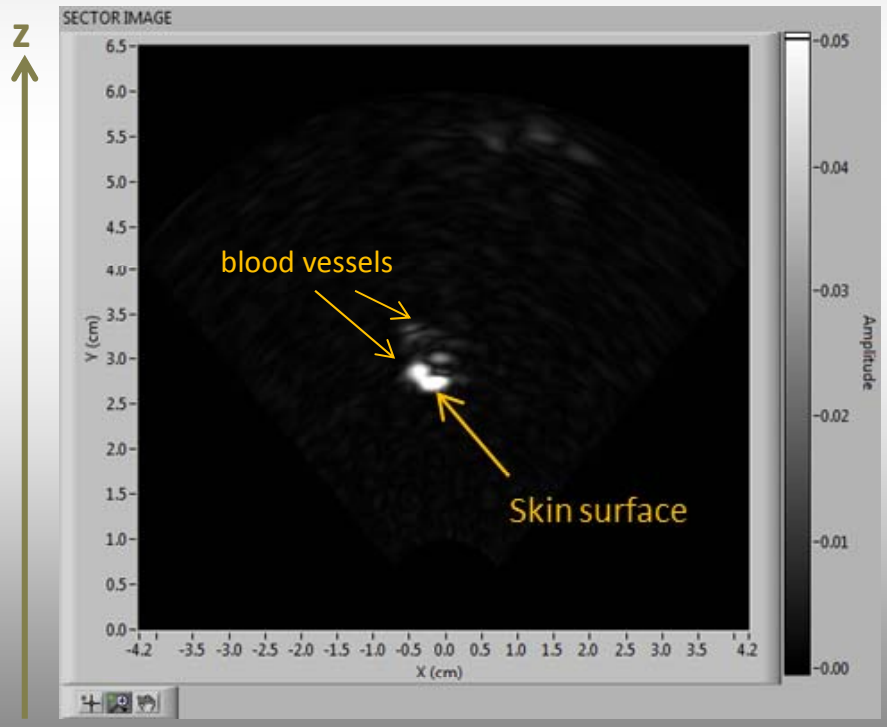

Tumor vertical cross-section

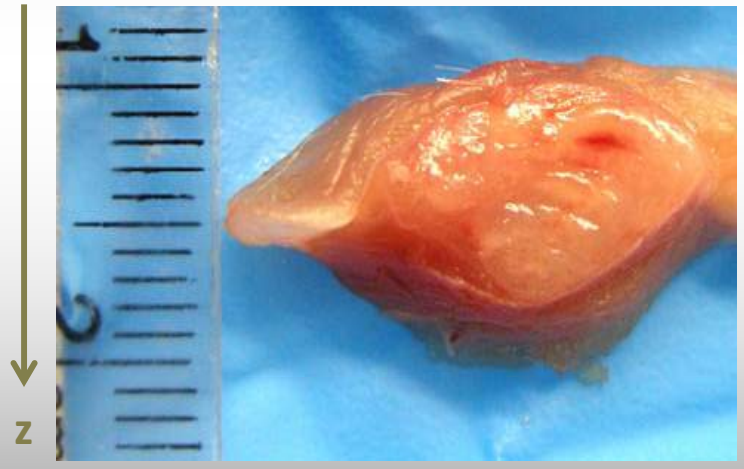

PA scan: 1W laser, 1-5 MHz chirp (1ms), 64-element 2.8 MHz phased array transducer.

Deep Subsurface Imaging and Comparison to US Images: Early Stages Tumor Simulation

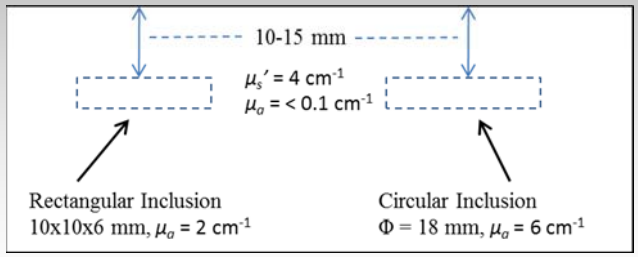

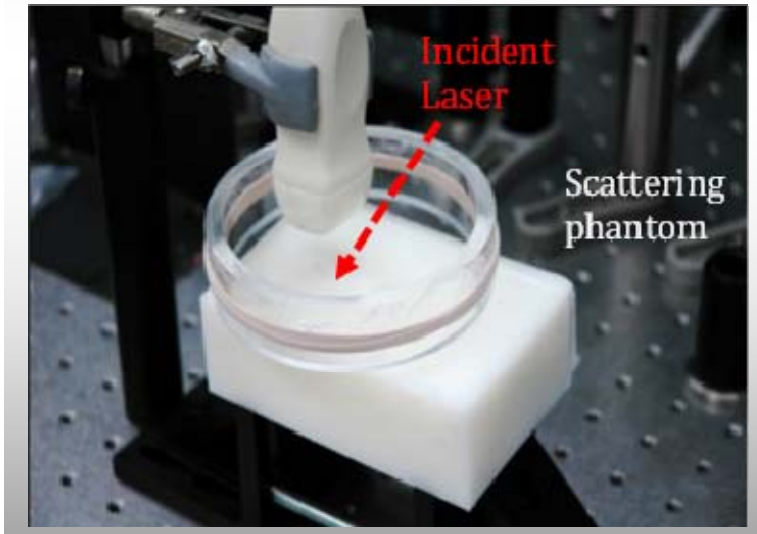

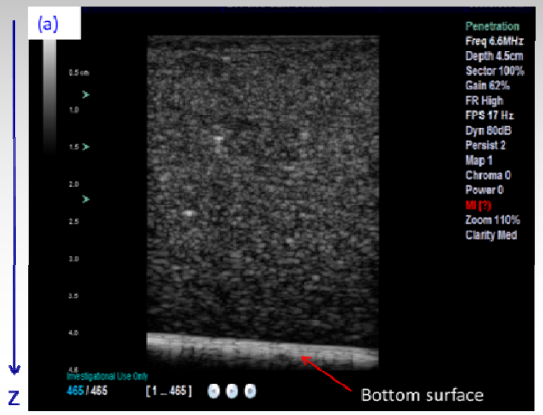

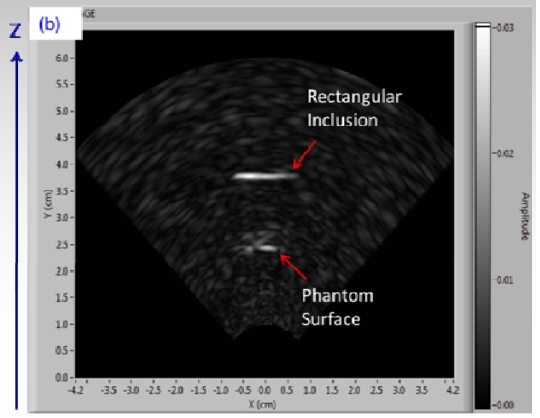

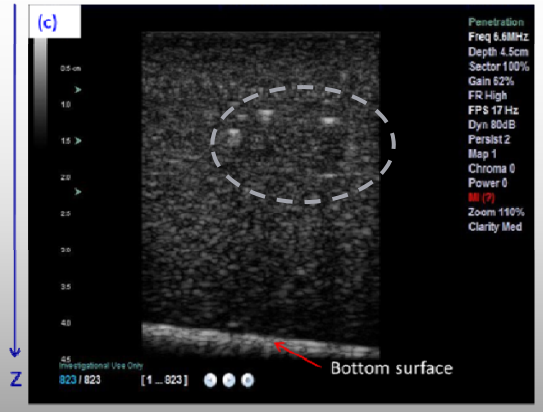

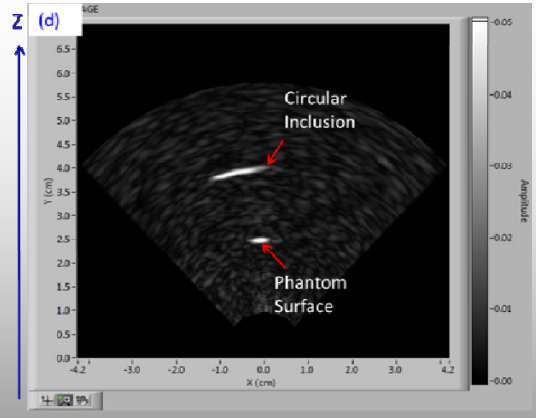

PA scan: P=1 W, 3 mm beam diameter, 1ms 1-5MHz chirp, 3.5 MHz phased array transducer.
US scan: 6.6 MHz 128-element linear array.

Phased Array FD-PA Imaging

FD-PA correlation image of blood vessels in a human wrist

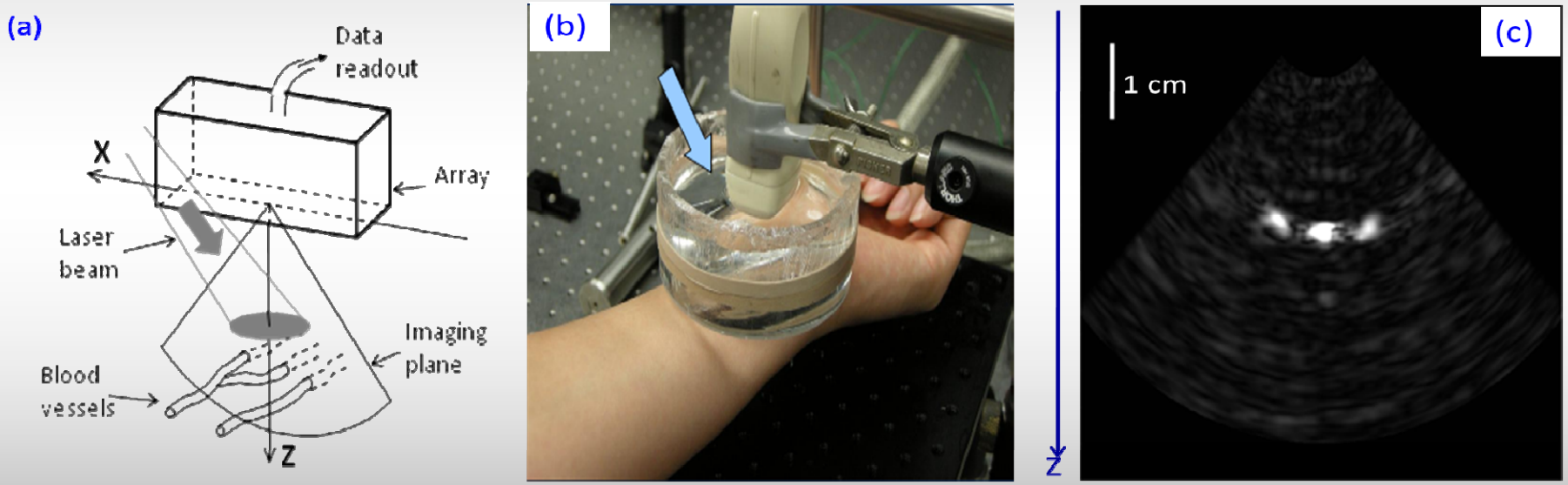

Laser intensity impinged on the wrist = 1 Watt
Beam diameter = 2 mm
64-elements phased array transducer frequency = 3.5 MHz

Future Outlook for Biomedical Photoacoustics

Imaging modality	Primary contrast	Imaging depth	Resolution
Confocal microscopy	Fluorescence/scattering	~0.2 mm	~1-2 microns
Two-photon microscopy	Fluorescence	~0.5 mm	~1-2 microns
Optical coherence tomography	Optical scattering	~1-2 mm	~10 microns
Ultrasonography (5 MHz)	Ultrasonic scattering	~60 mm	~300 microns
Photoacoustic microscopy (50 MHz)	Optical absorption	~3 mm	~15 microns
Photoacoustic tomography (3.5 MHz)	Optical absorption	~50 mm	~700 microns

Industrial outlook for biomedical photoacoustics

- **Endra,** 35 Research Drive, Suite 100, Ann Arbor MI 48103, USA
- Endra, Inc. is commercializing a breakthrough medical imaging technology that combines the properties of light-based (optical) imaging with ultrasound to enable advanced medical imaging. Based on the principles of photoacoustics, Endra's equipment utilizes ultrasound to detect the miniscule amount of heating caused by laser light deep within tissue, providing high contrast imaging at depths and spatial resolution far exceeding existing techniques.

- **VisualSonics Inc.,** 3080 Yonge Street Suite 6100, Box 66, Toronto, ON M4N 3N1, Canada
- Photoacoustic Mode, or 'PA' Mode is a new integrated feature built onto the Vevo LAZR platform to enhance high-resolution ultrasound-derived images with the sensitivity of optical imaging. The result is visually stunning anatomical images overlaid with functional hemodynamic and molecular data. Photoacoustics is changing the way cancer biologists, neurologists, developmental biologists and countless other researchers are seeing & obtaining their data.

- **TomoWave Laboratories, Inc. ,** 675 Bering Drive, Suite 575, Houston, Texas 77057-1203, USA
- *Optoacoustic Contrast Agent Development.* Currently, TomoWave is exploring the development of several new optoacoustic contrast agents involving gold nanorods (GNR). We are looking for potential collaborations within academia and industry partners to develop applications and validate biochemical properties.

Industrial outlook for biomedical photoacoustics (Cont'd)

- **Nanopartz Inc.,** 192 Barberry Pl., Loveland CO 80537, USA
- The Gold Nanoparticle for Nanotechnology. Nanopartz Gold Nanorods can enhance optical absorption (and photoacoustic signals) in targeted cancer tissue and provide high contrast for non-invasive cancer imaging. In many photoacoustic imaging applications, for example in optical mammographic methods, it is already understood that intrinsic contrast alone will not provide the sufficient sensitivity and specificity necessary, and that target contrast enhancement is likely to be required.

- **Fairway Medical Technologies,** 710 N. Post Oak Road, Suite 204, Houston, Texas 77024, USA
- Seno Medical, Inc. was formed to commercialize a new modality in cancer screening and diagnosis: opto-acoustic imaging. Unlike most screening techniques, which rely on anatomical imaging, Seno's goal is to bring functional imaging that can detect angiogenesis to the marketplace. Our first product is a small animal imaging device. This product application was successfully licensed to a world market leader, VisualSonics. Products for use with humans, focusing initially on breast cancer, are also in development. Seno's first clinical application is for breast cancer diagnosis.

III. From Gas-Cell Microphone PA to Optoelectronic Diffusion-Wave Imaging and High-Frequency Carrierography based on Energy Conversion Processes in Semiconductors and Devices

David Cahen, Department of Structural Chemistry. The Weizmann Institute of Science. Rehovot, Israel, *"Photoacoustic determination of photovoltaic energy conversion efficiency"*, Appl. Phys. Lett. **33** (9),1 November 1978

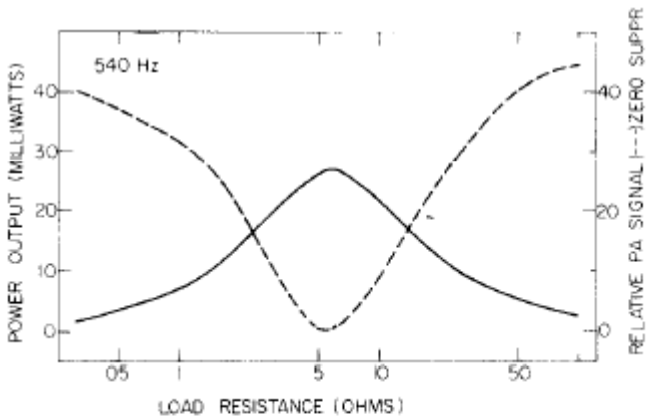

FIG. 1. Electrical output power and zero-suppressed PA signal as function of the resistance load over the Si photovoltaic cell. Illumination was by a 450-W Xe-arc lamp, filtered through a 3-cm-deep water filter and a uv (>420 nm) cutoff filter. The power curves for continuous and 540-Hz modulated light are virtually identical. Care was taken to exclude stray light and ensure 100% modulation. Detection of the modulated signal was by a Brookdeal 9502 Lock-in Analyzer. Knowles Electronics, Inc. BL 1685 microphones, polarized at 2.8 V, were used as acoustic transducers. Photovoltaic cell performance under these conditions: $V_{oc} = 0.53$ V; $I_{sc} = 85$ mA/cm^2; FF = 0.6.

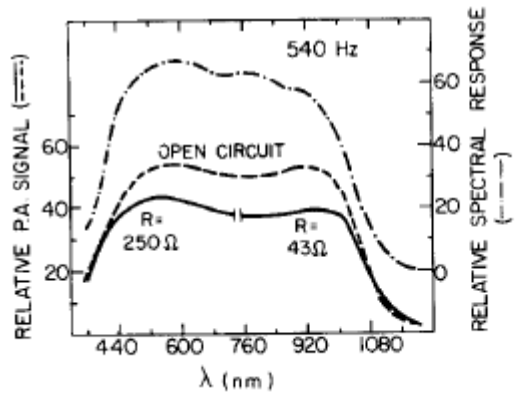

FIG. 2. Spectral response (i.e., short-circuit current) as a function of incident light wavelength and photoacoustic spectra at open circuit and under near-optimal load of the Si solar cell. The vertical scale of the spectral response curve is moved upwards for clarity's sake. Light from a 450-W Xe-arc lamp was passed through a Bausch & Lomb High-Intensity Monochromator. In the 360—740-nm range a grating blazed at 500 nm was used, while for the 740—1200-nm range a grating blazed at 1000 nm, in connection with a Corning 2-58 filter to eliminate second-order transmission, was used. The spectral widths for the two ranges were 20 and 40 nm, respectively. All data are corrected for the variation of incident light intensity with wavelength.

L. C. M. Miranda, Centro Tecnico Aerospacial, Instituto de Atividades Espaciais, 12200 San Jose dos Campos, SP, Brazil, *"Theory of the photoacoustic effect in semiconductors influence of carrier diffusion and recombination",* Appl. Opt. **21** (16), 2923 (August 1982).

$$\frac{\partial n}{\partial t} = -\frac{n}{\tau} + D\frac{\partial^2 n}{\partial x^2} + \frac{\beta I_0}{h\nu}\exp(\beta x)\exp(j\omega t), \qquad -l < x < 0. \quad (4)$$

Here, D and τ are the carrier diffusion coefficient and recombination time, respectively. Equation (4), together with the boundary conditions

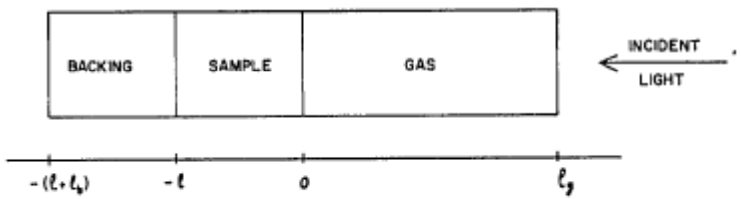

Fig. 1. Schematic configuration of the photoacoustic cell.

$$\frac{\partial^2 \phi_s}{\partial x^2} = \frac{1}{\alpha_s}\frac{\partial \phi_s}{\partial t} - \frac{Q_s(x,t)}{K_s}, \qquad -l < x < 0,$$

$$Q_s = \epsilon h\nu \frac{\partial n}{\partial t}(x,t).$$

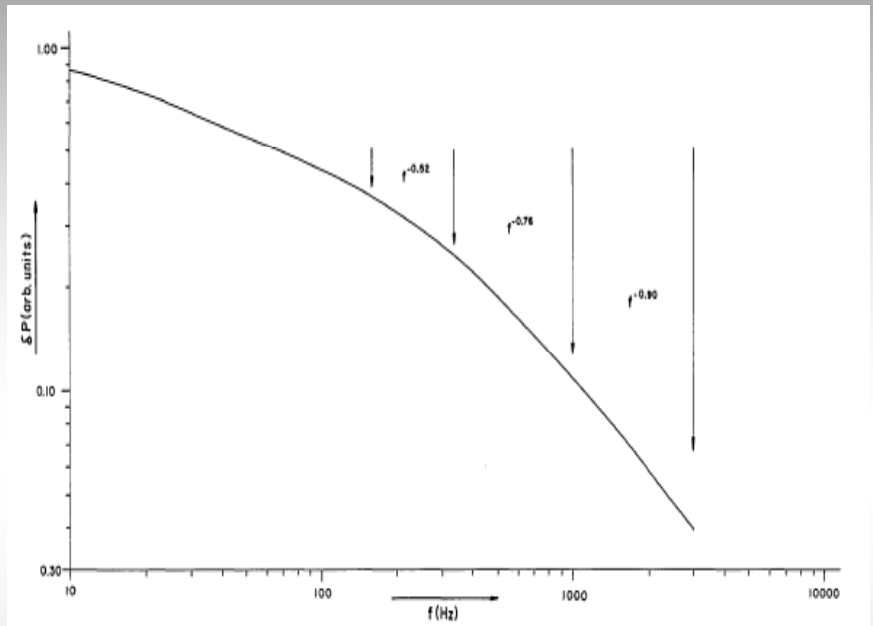

Fig. 2. Frequency dependence of the pressure fluctuation obtained from Eqs. (15) and (17) for a typical thermally thick (l = 1 cm) Si sample with a carrier recombination time of 1 msec.

"It is shown that the photoacoustic signal is ultimately governed by the relative sizes of the thermal diffusion time, the carrier diffusion, and the carrier recombination time".

C. C. Ghizoni, M. A. A. Siqueira, H. Vargas, and L. C. M. Miranda, *"On the use of photoacoustic cell for investigating the electron-phonon interaction in semiconductors",* Appl. Phys. Lett. **32**, 554 (1978)

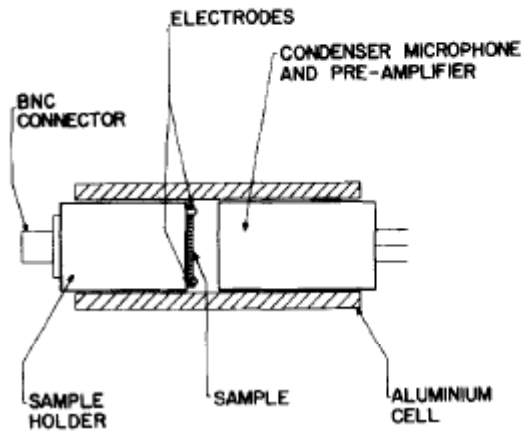

FIG. 1. Acoustic cell used for investing the transport properties in semiconductors.

when the energy gained from the field equals the energy lost to the lattice. This heat, dissipated by the carriers, is translated into excitation of mechanical vibrations (phonons) of the solid, via the electron-phonon interaction. Hence, by pulsing a dc voltage in a semiconductor, these phonons (excited by the heat dissipation), once transmitted through the crystal, can cause pressure fluctuations in the surrounding gas. Confining

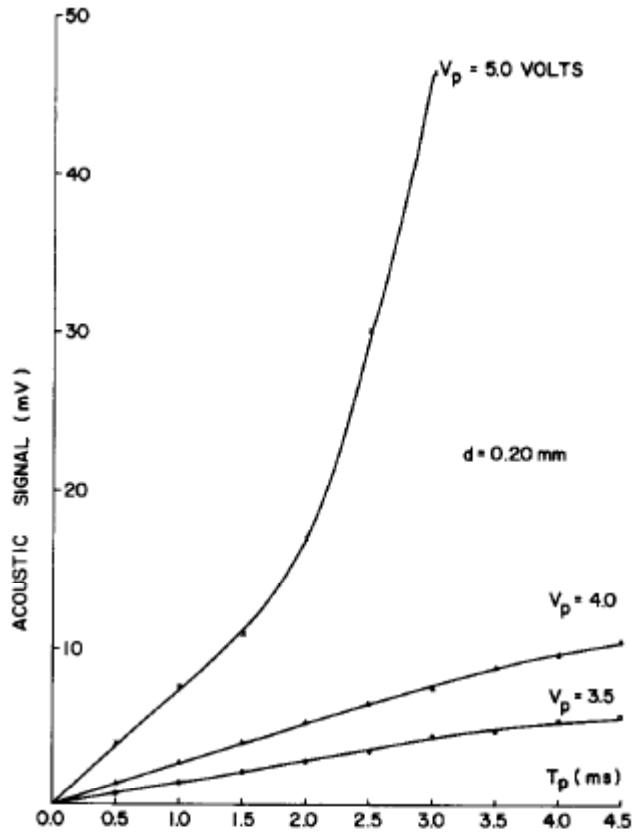

FIG. 3. Acoustic signal versus pulse duration for different values of the amplitude V_p.

I. F. Faria, C. C. Ghizoni, L. C. M. Miranda, and H. Vargas, «Photopyroelectric versus photoacoustic characterization of photovoltaic cells", J. Appl. Phys. **59**, 3294 (1986)

- The photothermal pyroelectric technique is applied to the characterization of photovoltaic cells and a comparison with the photoacoustic detection is presented. The difference between the photoacoustic and the pyroelectric data is interpreted in terms of a simple model for a junction type solar cell.

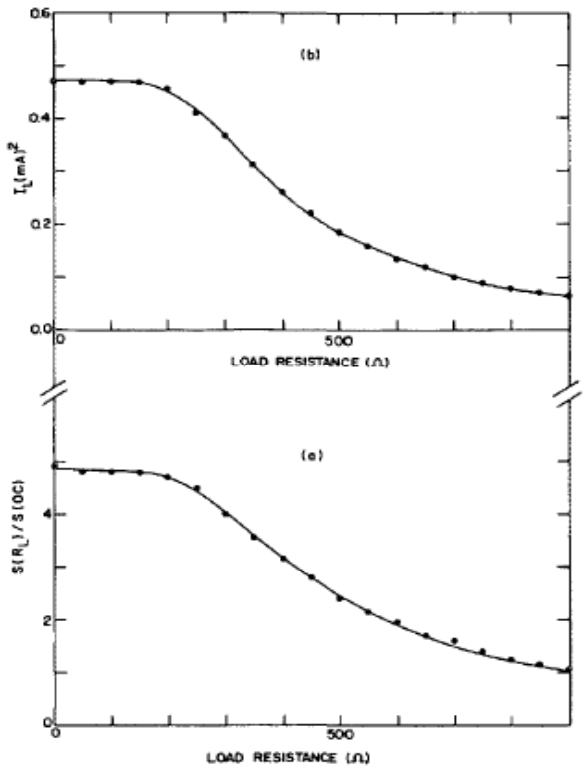

FIG. 4. (a) PP signal for the solar cell, as a function of the load resistance at 200 Hz under ~5.2-mW He-Ne laser illumination. (b) Dependence of the square of the load resistance I_L (mA) as a function of R_L, as obtained from the electrical measurements.

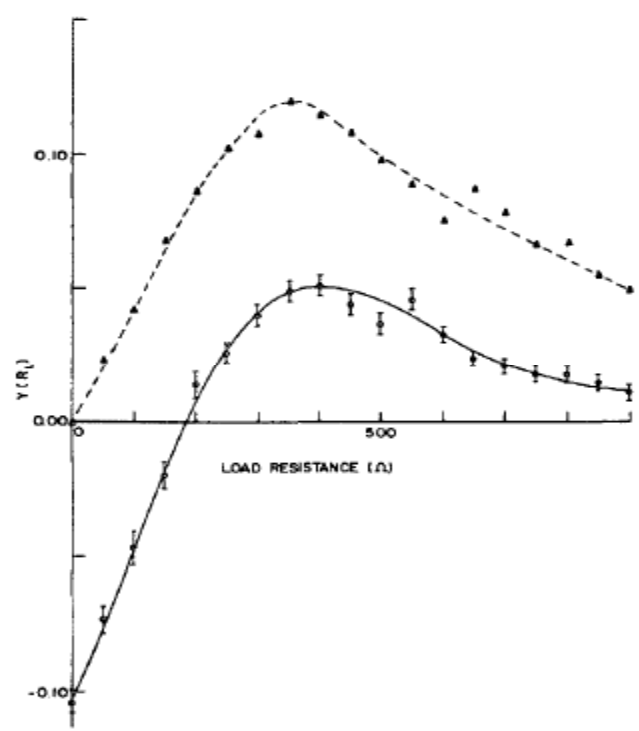

FIG. 1. Photopyroelectric γ_{PP} (solid) and photoacoustic γ_{PA} (dashed) conversion efficiencies as a function of the load resistance R_L, for a 500-μm-thick p-n solar cell, at 18 Hz under ~5.2 mW He-Ne laser illumination. At 350 Ω the PA-determined conversion efficiency is ~12%, whereas the PP-determined optimal conversion efficiency is ~5% at 400 Ω.

J. Opsal, A. Rosencwaig, and D. L. Willenborg, Therma-Wave, Inc., 47734 Westinghouse Drive, Fremont, California 94539, *"Thermal-wave detection and thin-film thickness measurements with laser beam deflection",* Appl. Opt. **22** (20), 3169 (October 1983).

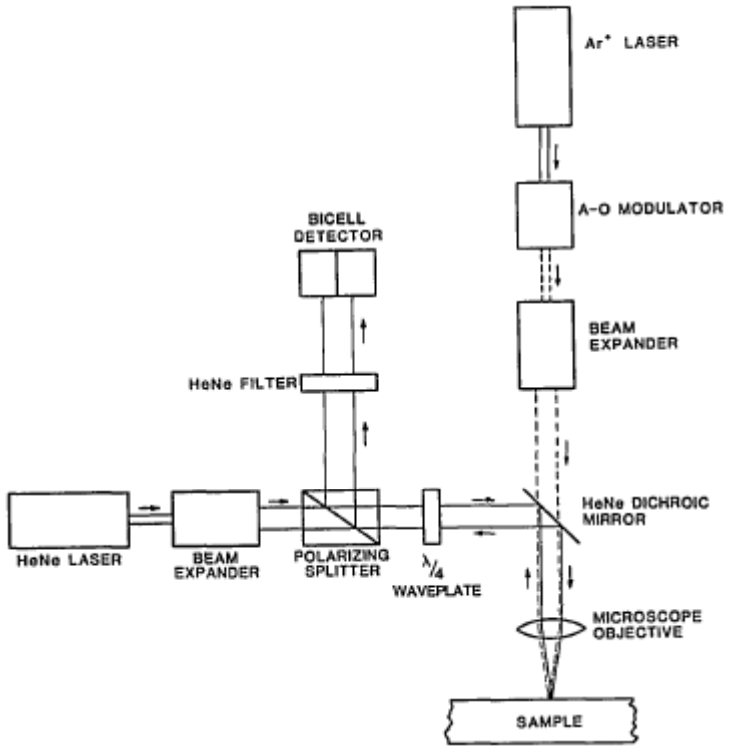

Fig. 1. Schematic depiction of laser beam deflection technique used for the thin-film thickness measurement experiments.

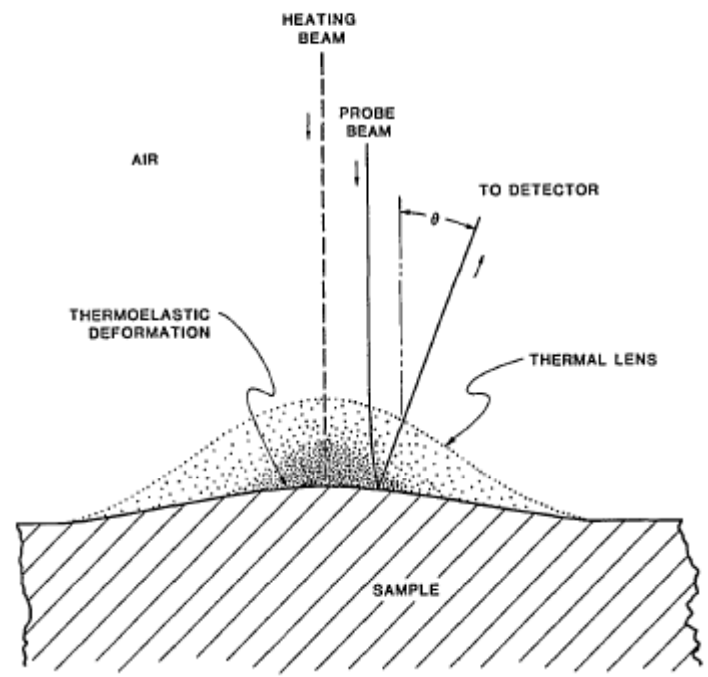

Fig. 2. Schematic depiction of physical processes affecting the laser probe beam for an opaque homogeneous sample including thermoelastic deformation of the air–sample interface and thermal lens effects in the air above the sample.

J. Opsal, A. Rosencwaig, and D. L. Willenborg

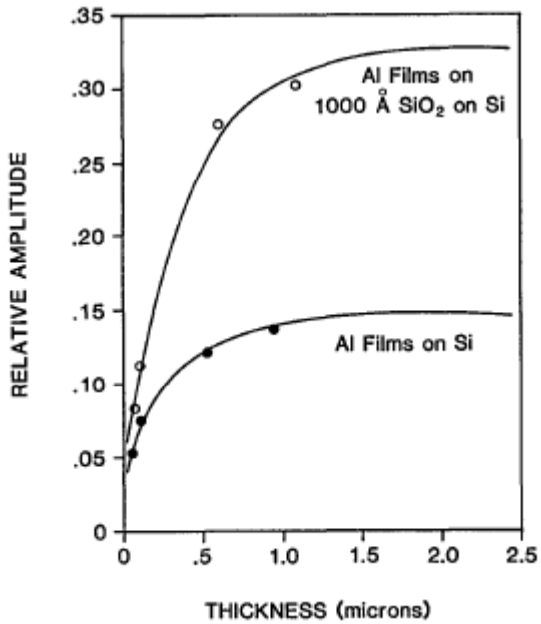

Fig. 6. Relative amplitude at 1 MHz of laser beam deflection signal as a function of Al film thickness for a series of Al-on-Si and Al-on-SiO_2-on-Si films. Circles are experimental data, and curves are from the extended Opsal-Rosencwaig model.

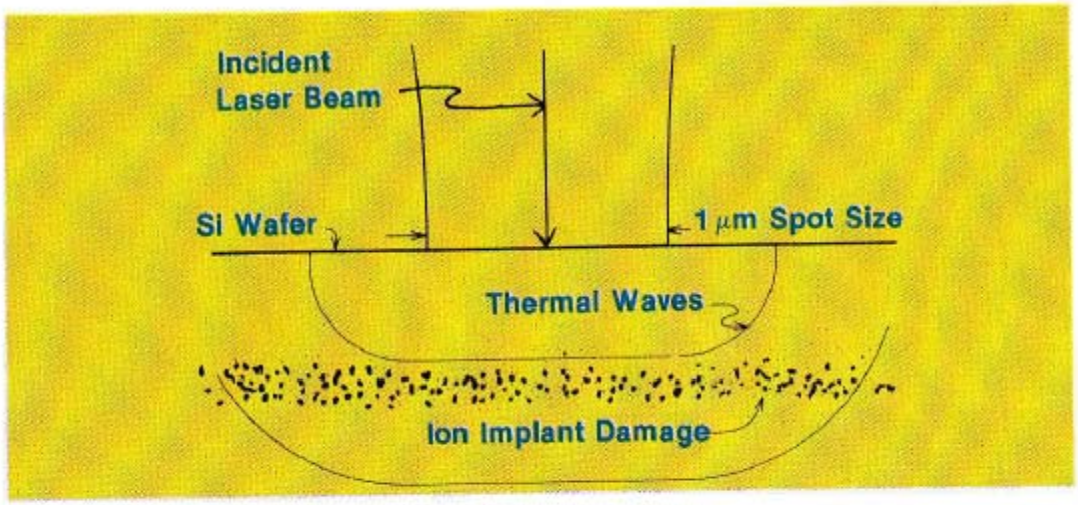

Fig. 2—Illustration of the generation of thermal waves, using a focused laser beam incident on a silicon wafer containing subsurface lattice damage from ion implantation.

J. Opsal, A. Rosencwaig, and D. L. Willenborg

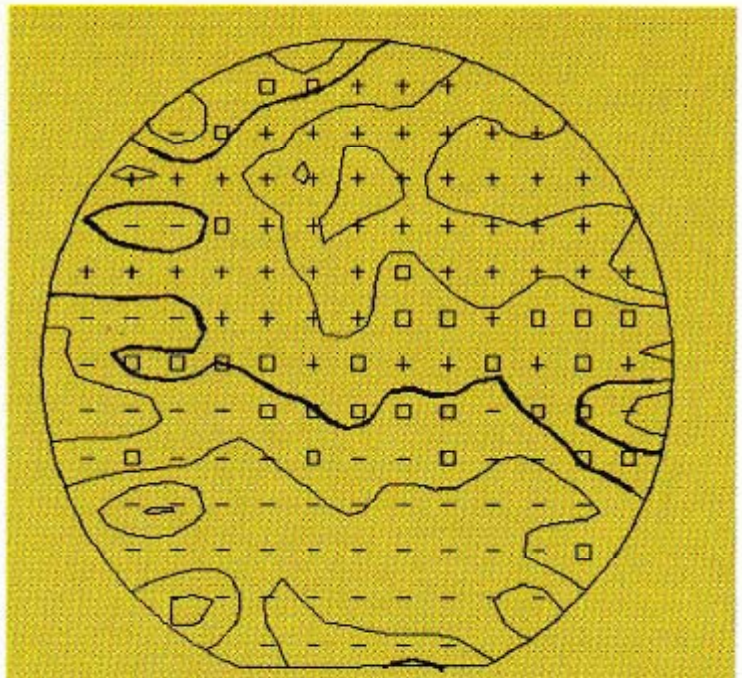

Fig. 9—Contour map of ion-implanted dose uniformity on a GaAs wafer [11].

Table I—Thermal Wave Diffusion Length for Thermal Conductors (Silicon and Metals) and Thermal Insulators (Oxides, Ceramics, and Biological Materials)

Modulation Frequency	Diffusion Length: Thermal Conductor	Diffusion Length: Thermal Insulator
100 Hz	200–300 μm	20–30 μm
10 kHz	20–30 μm	2–3 μm
1 MHz	2–3 μm	2000–3000 Å

A.Mandelis, A. Williams, and E. K. M. Siu, Photoacoustic and Photothermal Sciences Laboratory, Department of Mechanical Engineering, University a/Toronto, Toronto, Ontario M5S lA4, Canada, *"Photothermal wave imaging of metal-oxide-semiconductor field-effect transistor structures"*, J. Appl. Phys. **63**, 92 (January 1988)

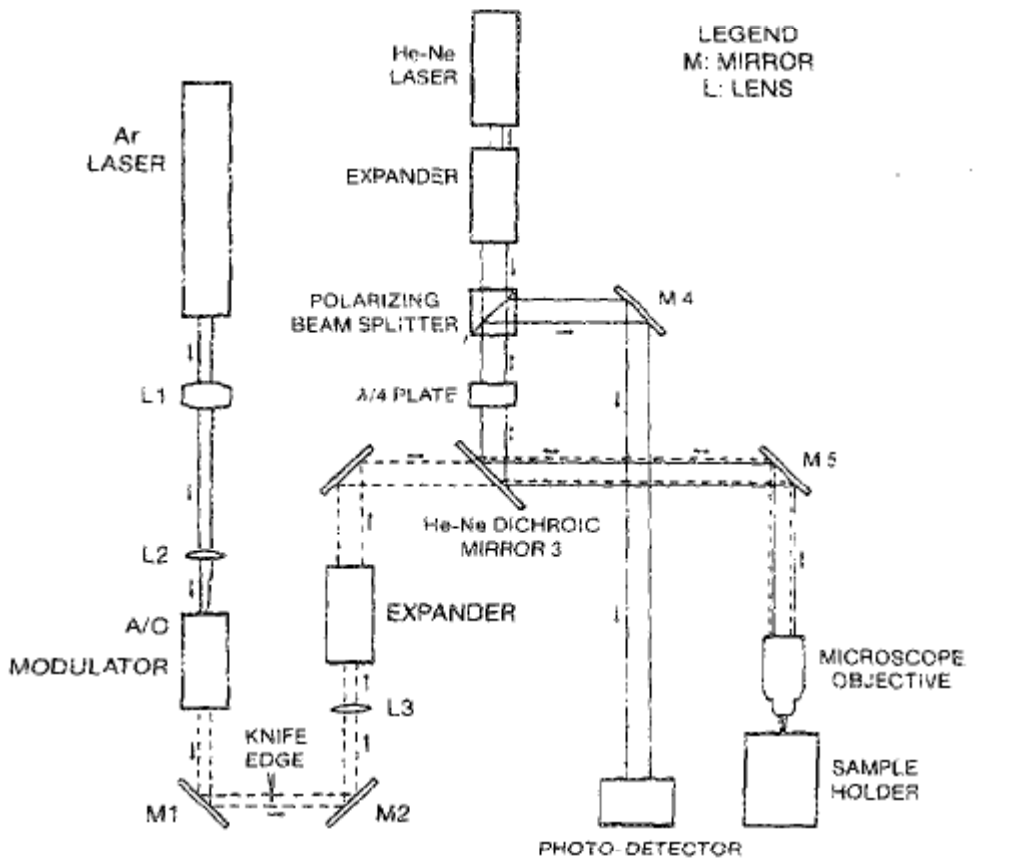

FIG. 1. Schematic diagram of PTW Imager apparatus. The entire assembly rests on an antivibrational optical table.

A photothermal wave imager which monitors the thermoelastic surface deformation due to absorption of a highly focused, intensity-modulated heating laser beam, was capable of producing images of subsurface features related to processing steps (thermal-wave depth profiling) at open circuit, as well as current flow sensitive images related to electronic processes in the active transistor (plasma-wave depth profiling).

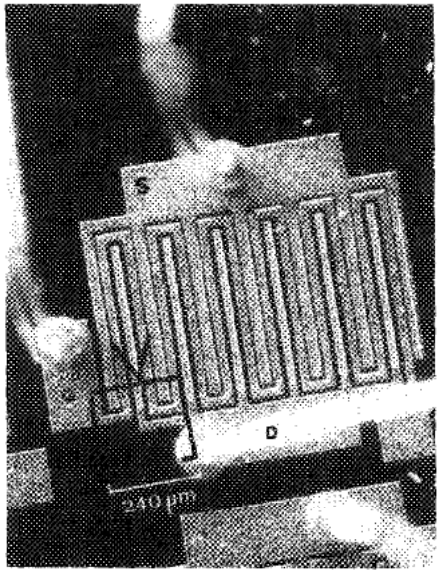

FIG. 3. Magnified view of the MOSFET, including scanned regions. S = source; G = gate; D = drain.

A.Mandelis, A. Williams, and E. K. M. Siu

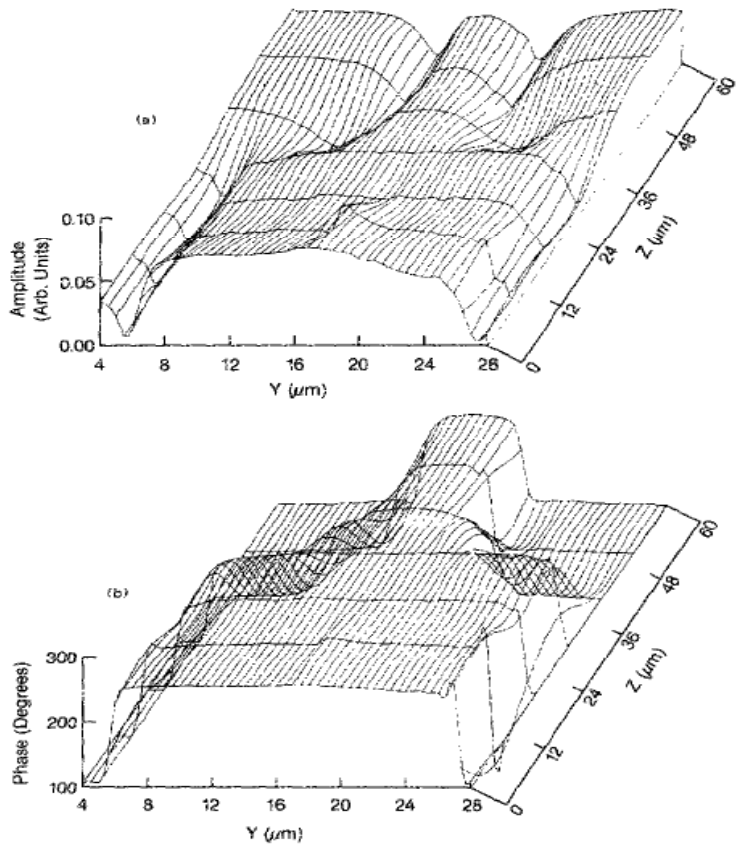

FIG. 5 Thermal-wave scan of a MOSFET gate metal padding as it narrows into the gate strip (Fig. 3). Light modulation frequency: 1 MHz; (a) amplitude, and (b) phase.

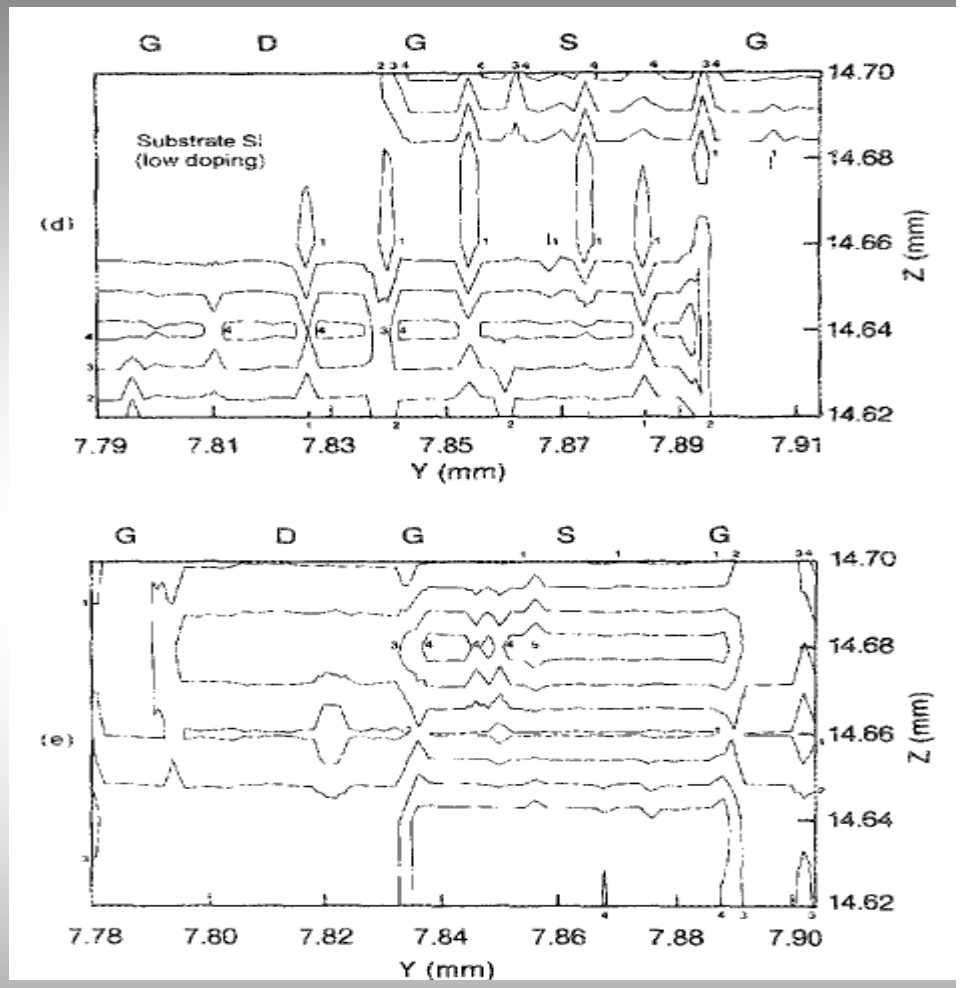

(d) Isometric contour map of phase of the device **at open circuit** with numbers corresponding to degrees (1) 200.17, (2) 326.79, (3) 453.41, (4) *580.02,* and (5) 706.64, (e) isometric map of phase of **activated device with $V_a = V_v = 1.5$ V.** Numbers correspond to degrees. (1) ~ 92.12', (2) 108.11·, (3) 308.36', (4) 508.60', and (5) *708.85'.*

A. Salnick, A. Mandelis, H. Ruda, and C. Jean, Photothermal and Optoelectronic Diagnostics Laboratories, Department of Mechanical and Industrial Engineering, University of Toronto, Toronto M5S 3G8, Canada, *"Relative sensitivity of photomodulated reflectance and photothermal infrared radiometry to thermal and carrier plasma waves in semiconductors"*, J. Appl. Phys. **82** (4), 1853 (August 1997).

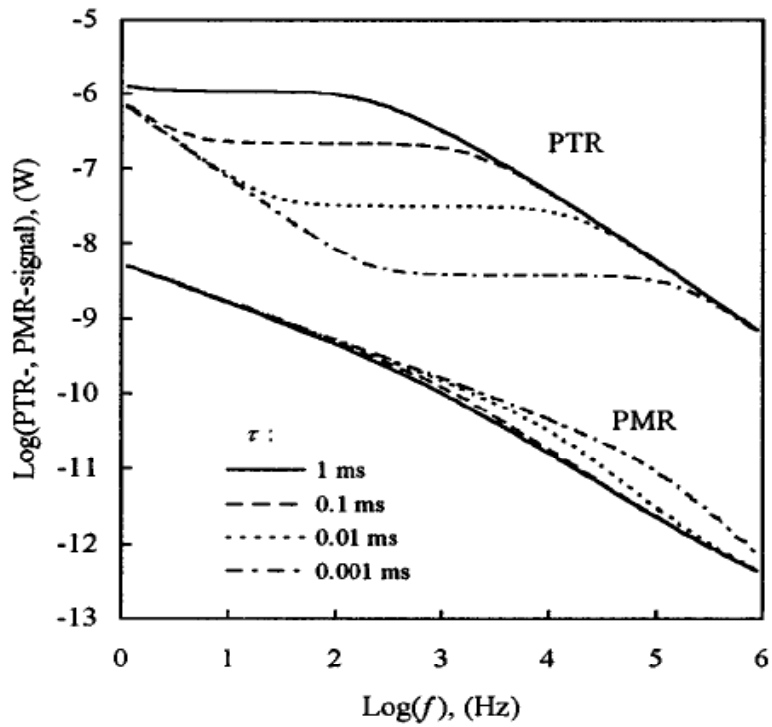

FIG. 2. PTR and PMR amplitude frequency responses for p-Si calculated using the values of the carrier plasma-wave and thermal-wave coefficients of Table II with different minority-carrier lifetimes, as indicated in the insets. Other calculating parameters are: $h\nu = 2.41$ eV, $I_0 = 10^4$ W/m^2, $N_i = 5\times10^{24}$ m^{-3}, $E_g = 1.12$ eV, $D_n = 3.5\times10^{-3}$ m^2/s, $s = 5.0$ m/s, $k = 150$ W/m K, and $\beta = 8\times10^{-5}$ m^2/s.

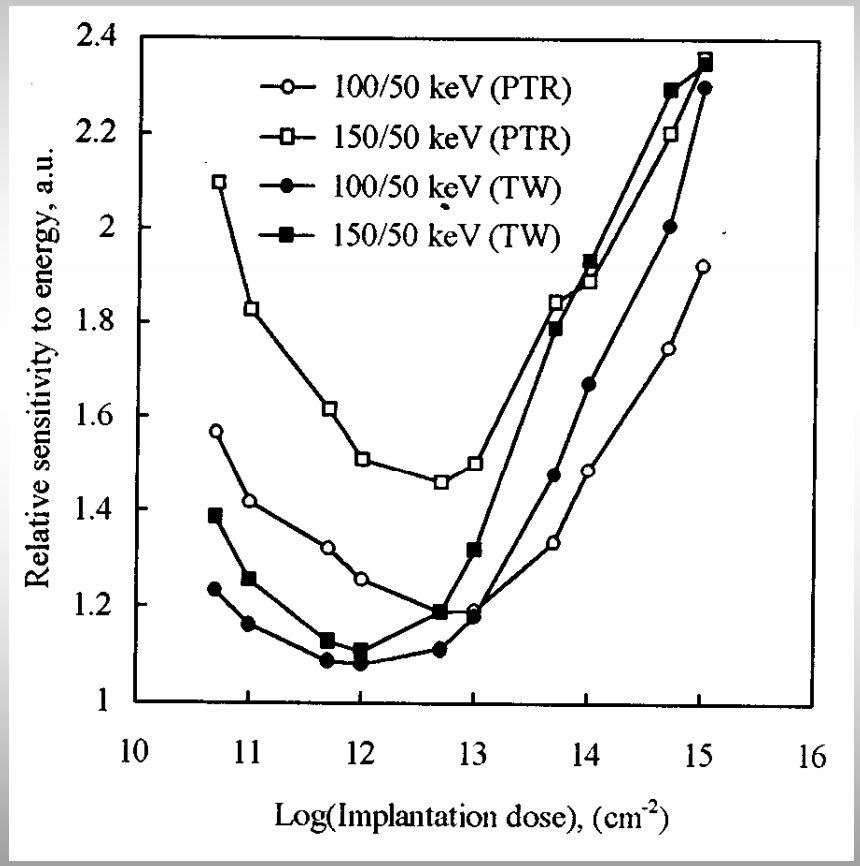

FIG. 4. Implantation dose dependencies of relative sensitivities to energy of the PTR amplitude at 10 kHz and TW signal. Relative sensitivity to implantation energy is defined as a ratio of the corresponding parameters obtained for a high-energy (100 keV, 150 keV) samples to that measured for 50 keV implanted wafer.

The Dawn of Photothermal Semiconductor Camera Imaging

S. Grauby, B. C. Forget, S. Holé, and D. Fournier, Equipe d'Instrumentation associe´e a` l'Universite´ Pierre et Marie Curie, Laboratoire d'Optique, UPR A0005 (CNRS), ESPCI, 10, 75005 Paris, France, *"High resolution photothermal imaging of high frequency phenomena using a visible charge coupled device camera associated with a multichannel lock-in scheme"*, Rev. Sci. Instrum. **70** (9), 3603 (September 1999)

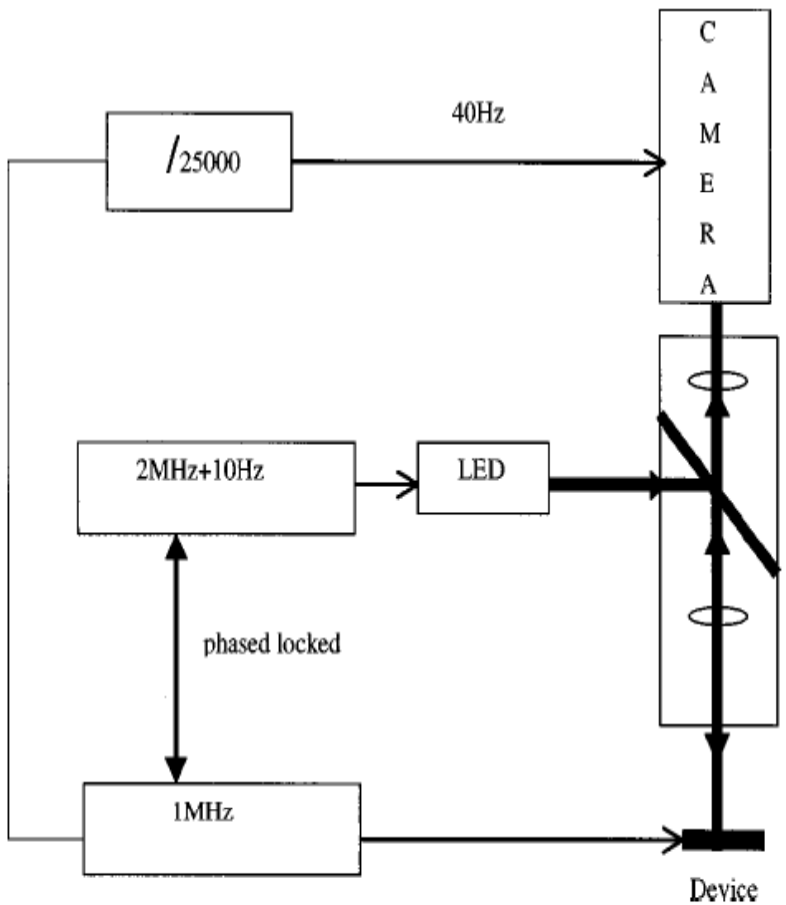

FIG. 1. Experimental setup.

III. THE HETERODYNE METHOD

The modulated field of temperature implies a modulation of reflectivity at the same frequency f_1 at the surface of the sample

$$R(x,y,t)=R_0(x,y,t)+R_1(x,y,t)\cos(2\pi f_1 t+\varphi(x,y)+\psi), \tag{2}$$

where $\varphi(x,y)$ and ψ are, respectively, the phase shift due to the thermal effect and the phase shift due to the setup. As for the LED, its flux is given by

$$\phi=\frac{\phi_1}{2}[1+\cos(2\pi f_2 t)].$$

Therefore, the flux reflected back to the camera[8] is proportional to

$$\begin{aligned} s(x,y,t) &= \frac{\phi_1}{2}\times R_0(x,y,t)+\frac{\phi_1}{4}\times R_1(x,y,t) \\ &\quad \times\cos(2\pi F t-\varphi(x,y)-\psi) \\ &\quad +\text{terms at high frequencies.} \end{aligned} \tag{3}$$

B.C. Forget, S. Grauby, D. Fournier, P. Gleyzes and A.C. Boccara, *"High-resolution temperature field imaging",* Electron. Lett. **33** (20), 1688 (September 1997).

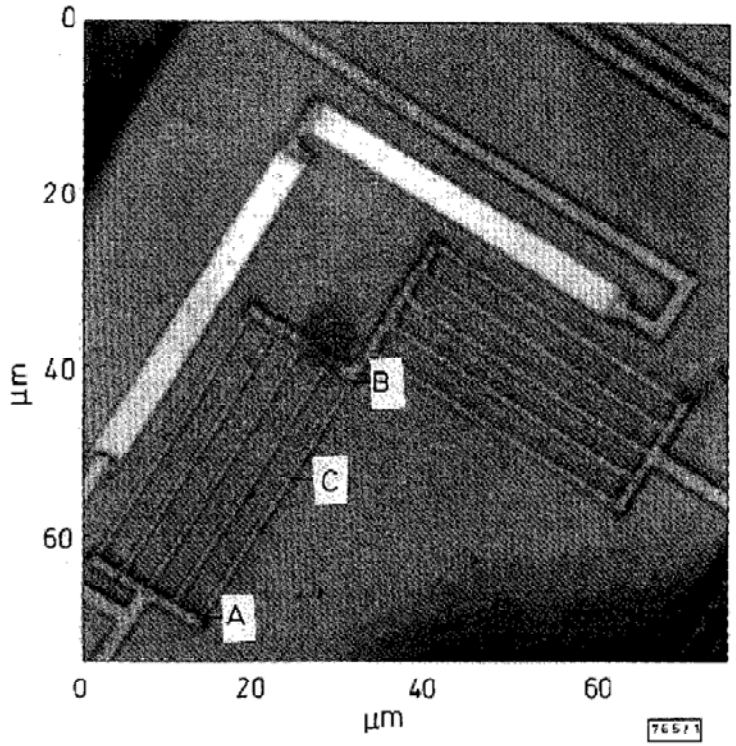

Fig. 1 *Optical image of sample*

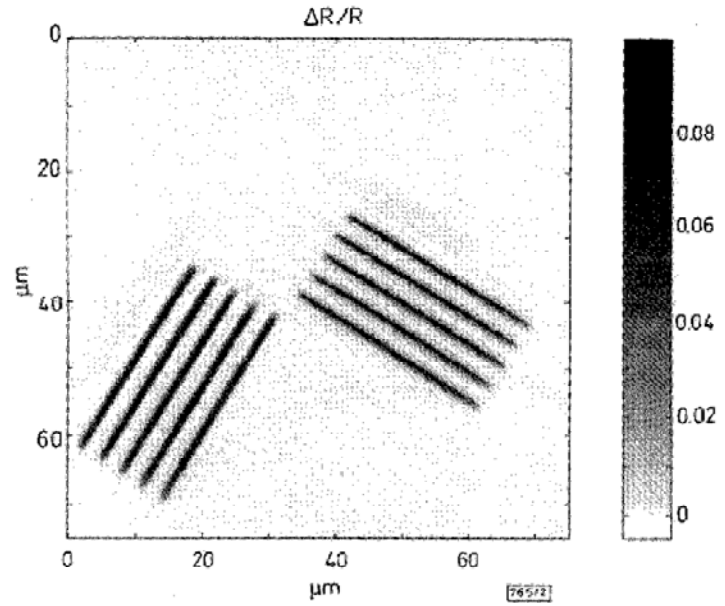

Fig. 2 *Second harmonic temperature field*

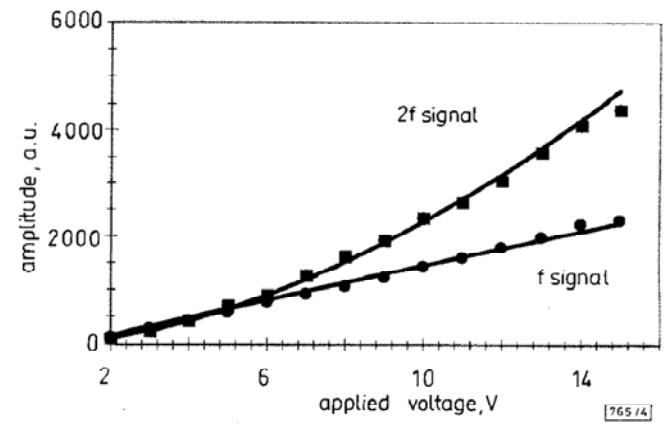

Fig. 4 *First and second harmonic signals against applied voltage*

A. Mandelis, J. Batista, and D. Shaughnessy, Center for Advanced Diffusion-Wave Technologies, Department of Mechanical and Industrial Engineering, University of Toronto, Toronto, Canada M5S 3G8, *"Infrared photocarrier radiometry of semiconductors: Physical principles, quantitative depth profilometry, and scanning imaging of deep subsurface electronic defects"*, PHYSICAL REVIEW **B 67**, 205208 (2003)

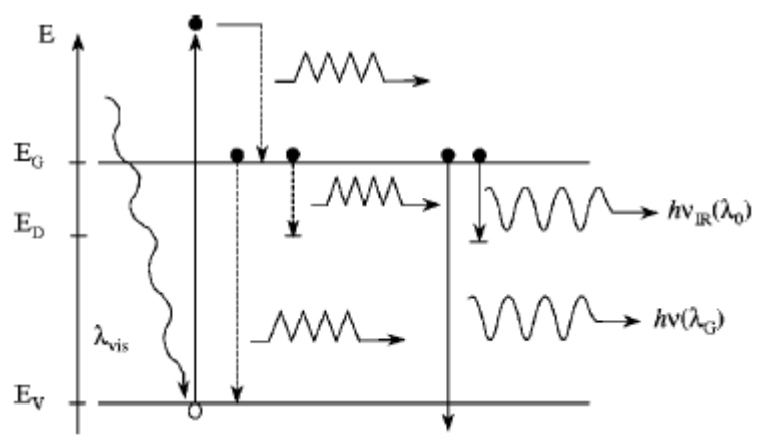

FIG. 1. *n*-type semiconductor energy-band diagram showing excitation and recombination processes. Energy emission processes include nonradiative intraband and interband decay accompanied by phonon emission, as well as direct band-to-band recombination radiative emissions of energy $\hbar\omega(\lambda_G)$ and band-to-defect/impurity-state recombination IR emissions of energy $\hbar\omega_{IR}(\lambda_D)$.

$$P(\omega) \approx F_2(\lambda_1,\lambda_2)\int_0^L \Delta N(z,\omega)\,dz,$$

$$F_2(\lambda_1,\lambda_2) \equiv \int_{\lambda_1}^{\lambda_2} [1-R_1(\lambda)]\{1+R_b(\lambda) \times [1+R_1(\lambda)]\}\eta_R W_{eR}(\lambda)C(\lambda)d\lambda.$$

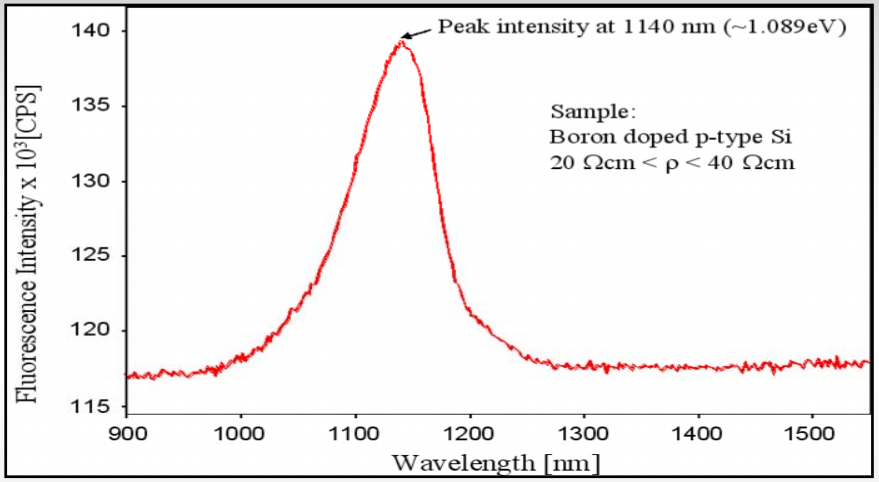

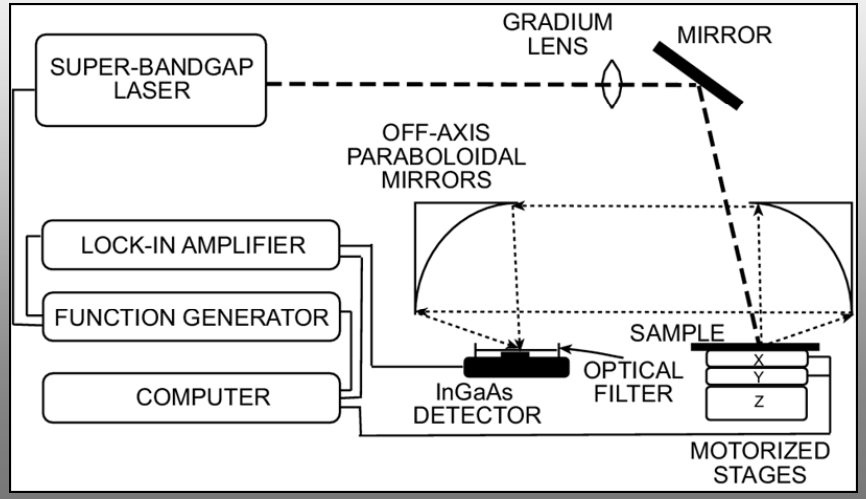

Electronic Defect/Lifetime Imaging, D. Shaughnessy and A. Mandelis, J. Electrochem. Soc. 153 (4), G283 (2006).

f = 100 Hz

f = 12 kHz

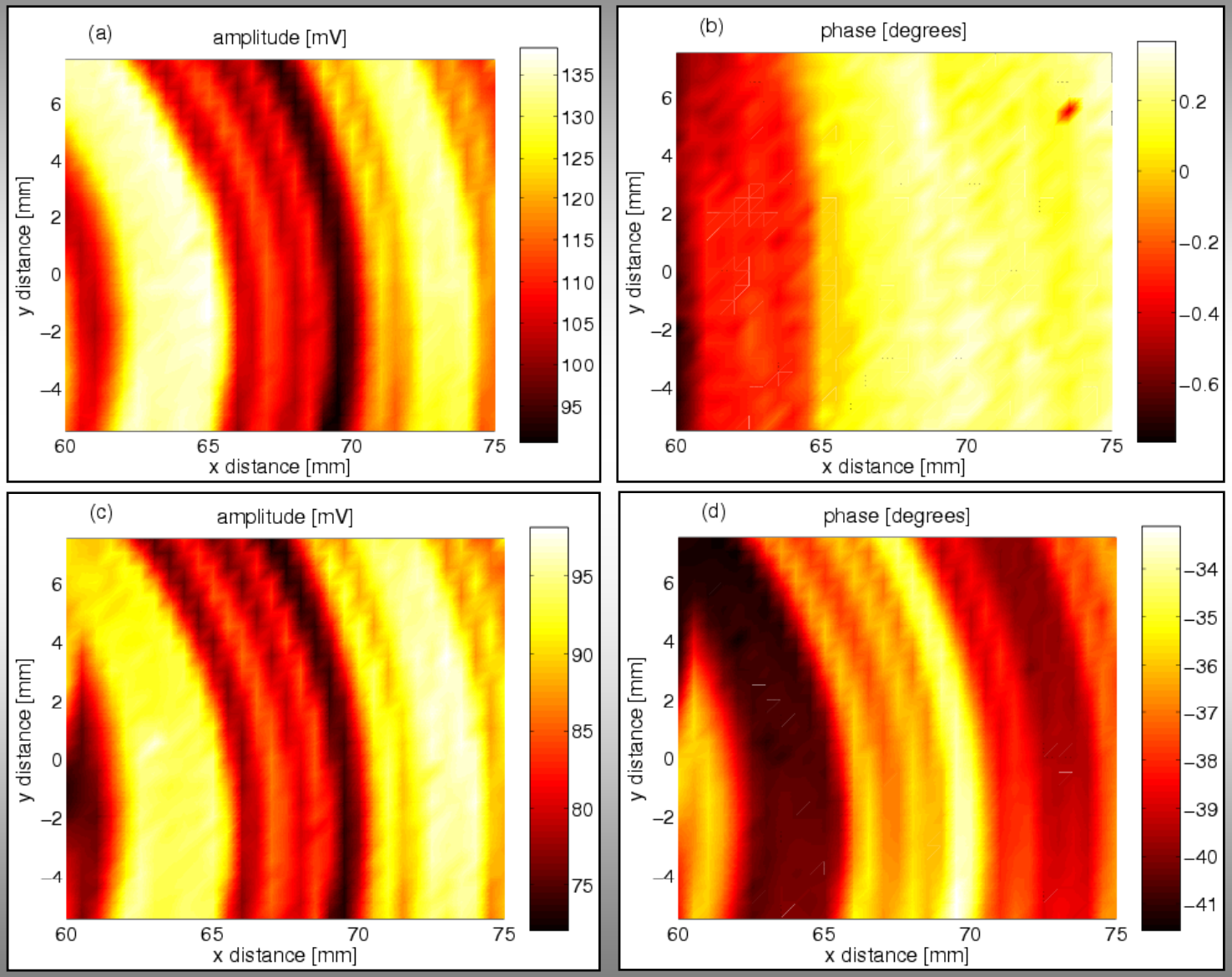

Defect is consistent with swirl defects generated during Czochralski crystal growth.

Infrared Lock-in and Heterodyne Carrierography

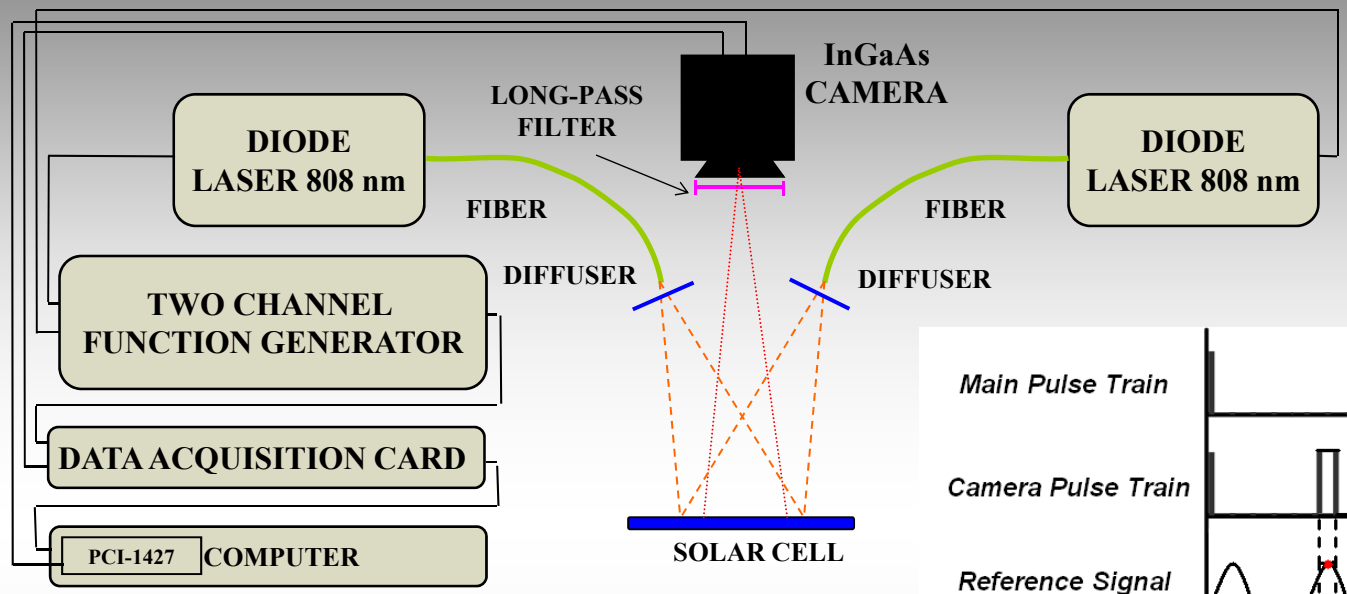

$$Amplitude = \sqrt{(S^0)^2 + (S^{90})^2},$$

$$Phase = \arctan\left(\frac{S^{90}}{S^0}\right)$$

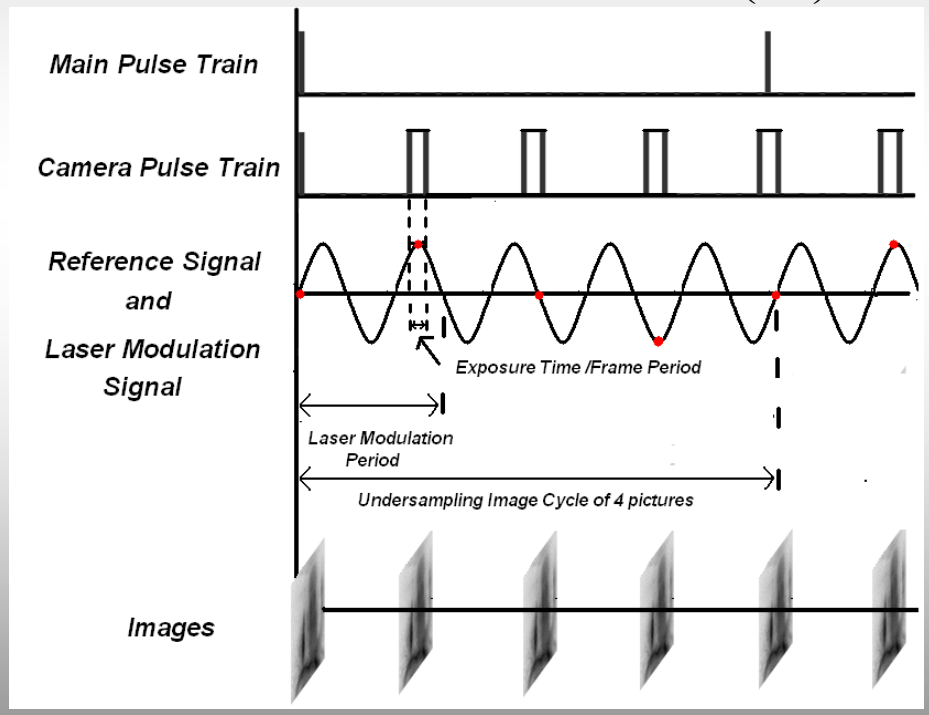

- Full frame exposure time 0.13 – 16 ms
- Spectral bandwidth 0.9 - 1.7 μm
- Electronic shutter
- 256x320 pixels
- observed area from 2 x 2 cm^2

Low-Frequency Lock-in Carrierography

A. Melnikov, A. Mandelis, J. Tolev, P. Chen, and S. Huq,

"Infrared lock-in carrierography (photocarrier radiometric imaging) of Si solar cells", J. Appl. Phys. **107**, 114513 (2010)

Camera image

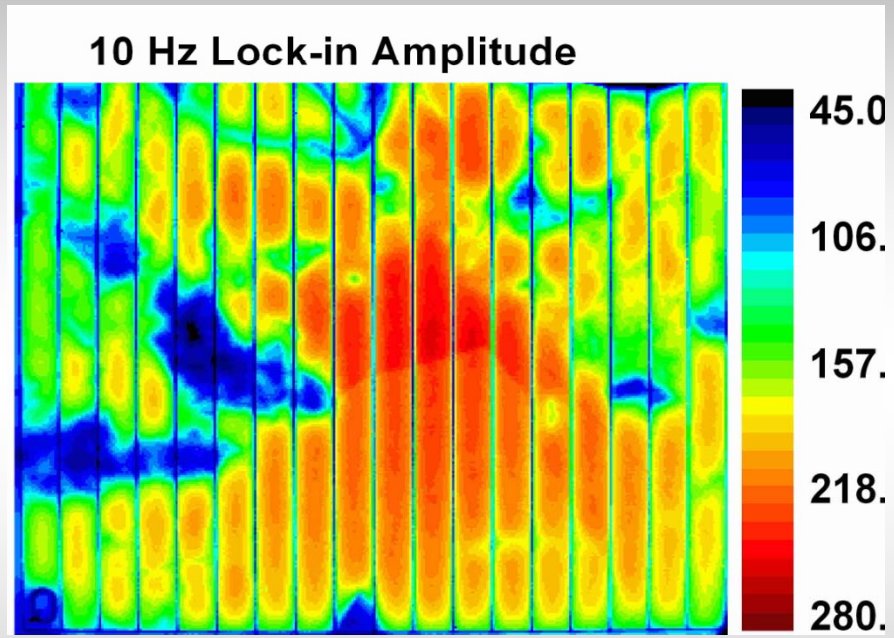

Semilab WT-2000

μ-PCD , lifetime,

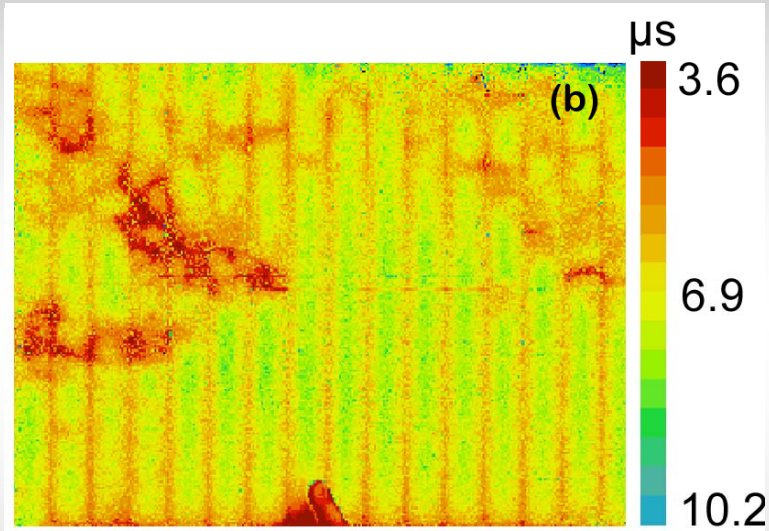

- Lock-in carrierographic amplitude correlates mainly with recombination lifetime

$$S_{PCR} = \frac{C}{\pi a_2} \int_0^\infty \tilde{N}(\xi;\omega) J_1(\xi a_2)\, d\xi \qquad S_{PCR}(\omega) \propto \int_0^\infty N(z;\omega)\, dz$$

"Carrierography"

Center for Advanced Diffusion-wave Technologies (CADIFT), University of Toronto, Toronto, Ontario M5S 3G8, Canada

High-Frequency Heterodyne Carrierography

Two modulation frequencies:
f_1 for one laser and $f_2=f_1+\Delta f$ for the other

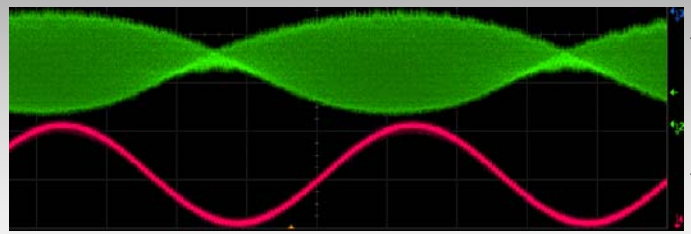

Combined laser irradiation

Reference signal Δf

- Heterodyne method is a detection method based on non-linear CG (or PCR) using the trigonometric identity

$$\sin(\alpha)\sin(\beta)=\frac{1}{2}\cos(\alpha-\beta)-\frac{1}{2}\cos(\alpha+\beta)$$

- The heterodyne signal depends both on excess minority carrier concentration and degree of nonlinearity
- Heterodyne method allows constructing high frequency images using long exposure time of the camera
- Heterodyne image shows higher contrast of solar cell optoelectronic inhomogeneities

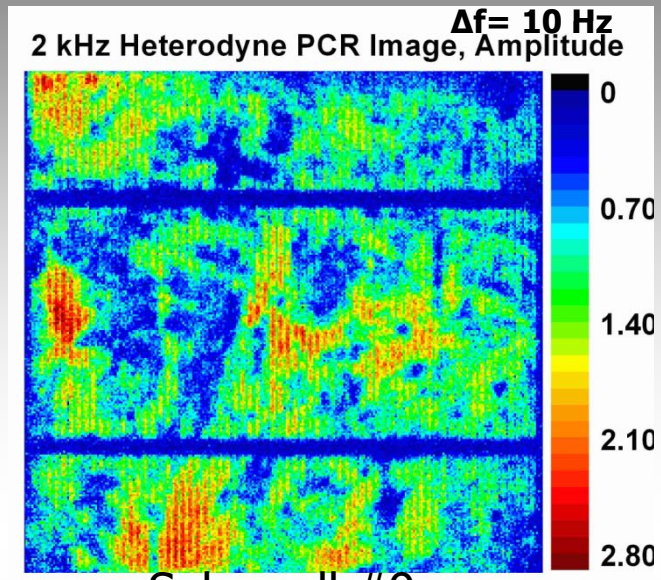

Solar cell #9

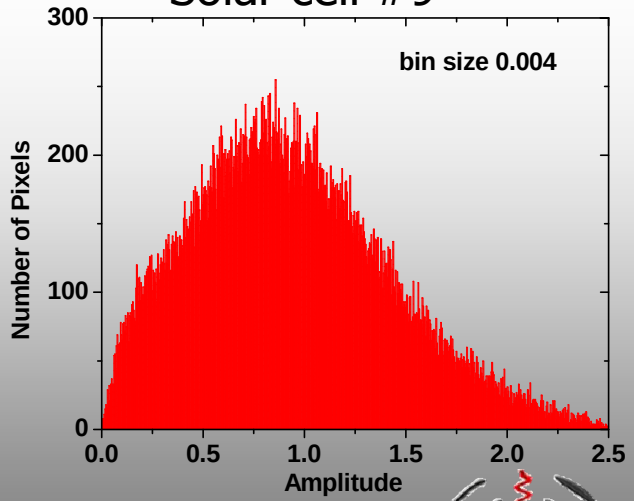

Center for Advanced Diffusion-wave Technologies (CADIFT), University of Toronto, Toronto, Ontario M5S 3G8, Canada

Heterodyne CG (continued)

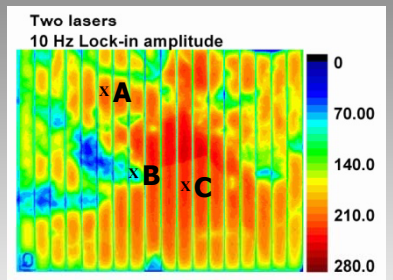

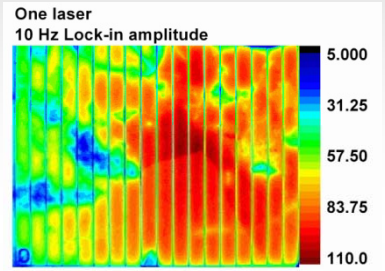

Ratio

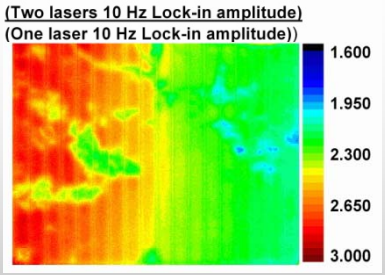

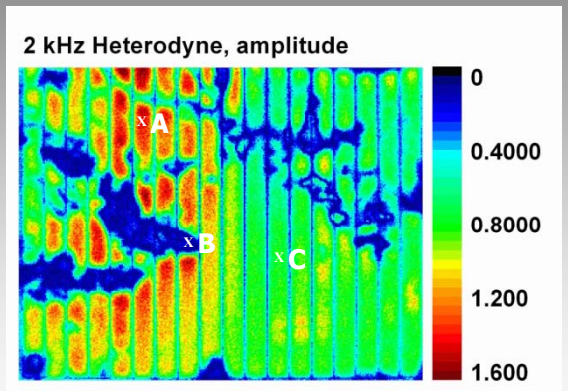

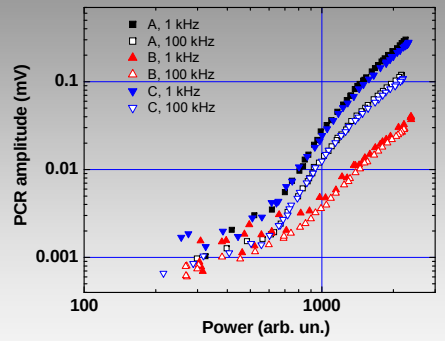

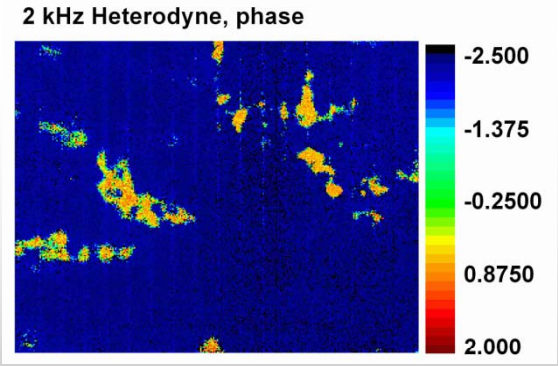

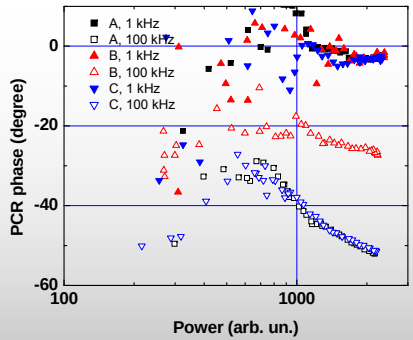

- Ratio of two lock-in images with different excitation intensity shows non-linear inhomogeneities of solar cell
- Superposition of non-linear inhomogeneities and excces minority carrier concentration inhomogeneities leads to higher contrast of heterodyne image

dc PL and heterodyne carrierographic image (square laser waveform) of entire Si solar cell

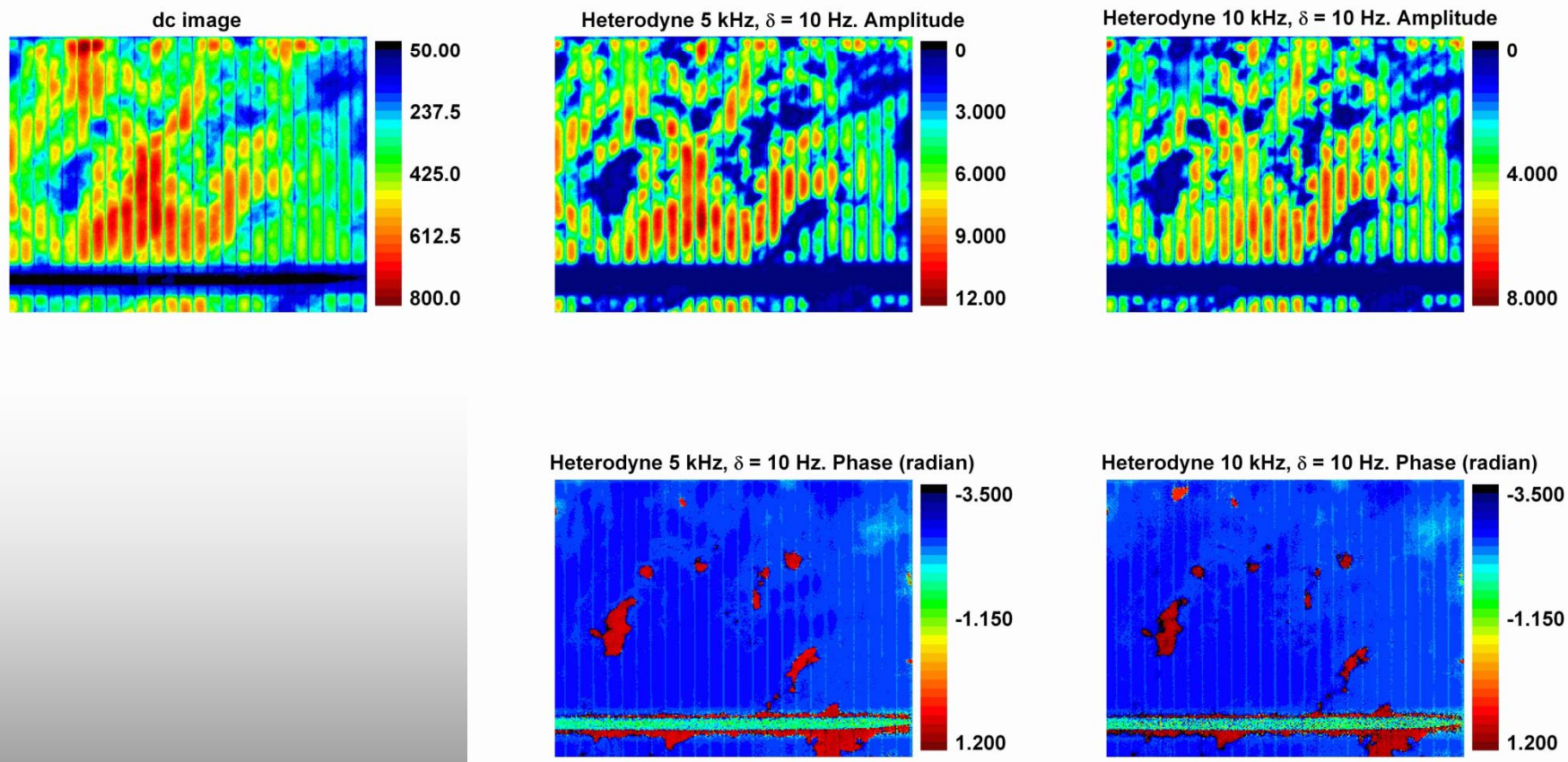

Industrial outlook for photothermal and photocarrier diagnostic science and technologies

- **KLA-Tencor,** 1 Technology Drive Milpitas, CA 95035-7916, USA
- Acquisition of Therma-Wave a "Non-Event" in the Metrology/Inspection Equipment Market. Therma-Wave held only a 1.5% share of the metrology/inspection market in 2005 compared to KLA-Tencor's 44%. The major advantage to KLA-Tencor is Therma-Wave's leadership in Implant Metrology, a technology that back in 1999 Therma-Wave sued KLA-Tencor for patent infringement.

- **Intervac Inc.,** 3560 Bassett Street, Santa Clara, CA 95054, USA
- *Solar Cell Inspection*. NANOVISTA is Intevac's high speed, high resolution photovoltaic cell inspection system. Photoluminescence images of in-process materials and finished cells are collected at up to 3600 wph. With its high throughput capability and proprietary, high sensitivity sensor technology, NANOVISTA captures 1.3 megapixel images in milliseconds with greater accuracy than other imaging systems. NANOVISTA interpretive software performs powerful image analysis using simple graphical tools. The data analysis can then be used to provide process monitoring, simple pass/fail criteria, or wafer grading.

- **HORIBA Jobin Yvon Inc.,** 3880 Park Avenue, Edison, NJ 08820-3097, USA
- *Laser photoreflectance and photoluminescence systems*. Determination of energy band structure, Characterization of quantum well depth, Trap effect studies, Strain analysis, alloy composition in ternary and quaternary compounds.

- **Diffusion-Wave Diagnostic Technologies,** Toronto, ON M1M 2V3,Canada
- Lock-in and Heterodyne Carrierography Imaging Systems.

IV. From Gas-Cell Scanned NDT to Lock-in Thermography and the Thermal-Wave Radar Imager

The early years of NDT imaging

Y. H. Wong, R. L. Thomas, and G. F. Hawkins, Department of Physics, Wayne State University. Detroit. Michigan 48202, *"Surface and subsurface structure of solids by laser photoacoustic spectroscopy"*, Appl. Phys. Lett. **32** (9), 538 (May 1978)

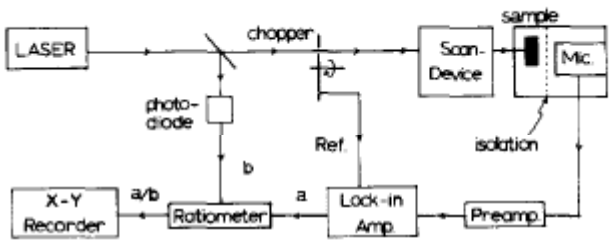

FIG. 1. Schematic diagram of the laser photoacoustic scanning system.

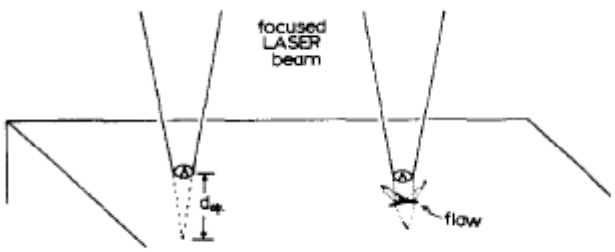

FIG. 2. Geometric consideration of flaw detection with the photoacoustic technique.

evaluated. Therefore we define an effective absorbing depth d_{eff} given by

$$d_{eff} = d_{th} \quad \text{for } d_{th} < d_{op},$$

$$d_{eff} = d_{op} \quad \text{for } d_{th} > d_{op}.$$

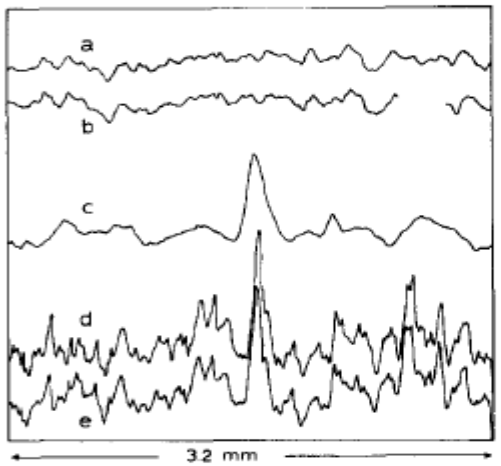

FIG. 3. Typical traces of the photoacoustic signal (f=800 Hz). (a) and (b) Repeated scan on surface with no obvious crack. (c) Scan on surface with obvious cracks. (d) and (e) repeated scan on surface (c) with a better focused laser beam.

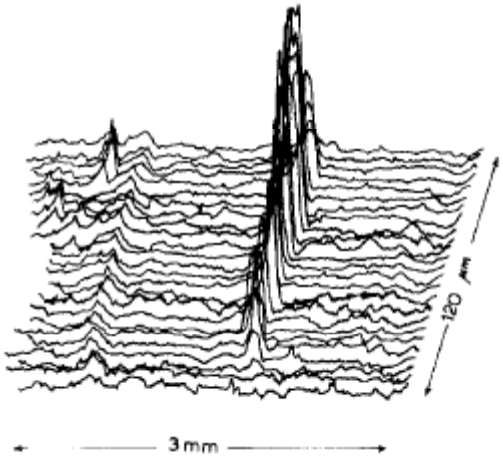

FIG. 4. An X–Y scan of surface with obvious cracks.

Silicon nitride ceramic samples

G. Busse and A. Orhabeck, Institut fuer Physik. Fachbereich Elektrotechnik. Hochschule der Bundeswehr Muenchen. D-80/4 Neubiberg. Federal Republic of Germany, *"Optoacoustic Images",* J. Appl. Phys. **51** (7), 3576 (July 1980)

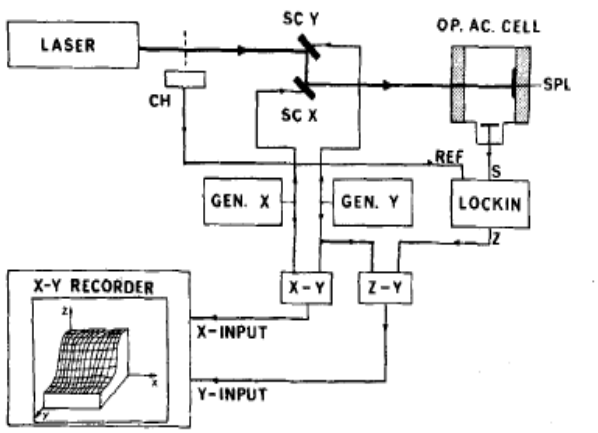

FIG. 1. Experimental arrangement. The laser beam is deflected by saw-tooth-generator driven scanners SCX and SCY. The optoacoustic signal voltage is combined with the scanner voltages in such a way as to give a two-dimensional projection of the signal surface.

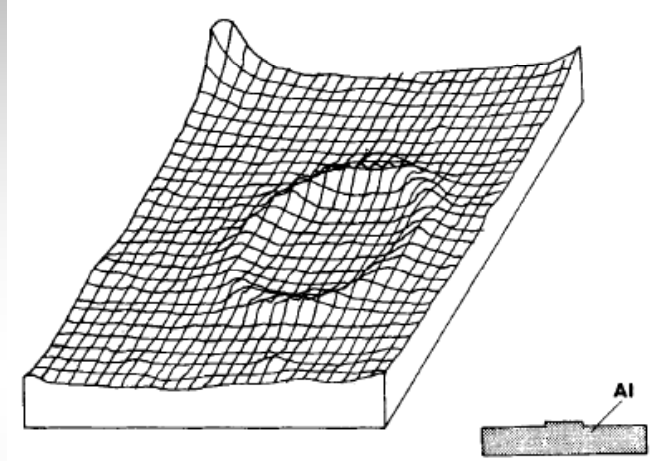

FIG. 3. Surface imaging of an aluminum sample. Optoacoustic signal is enhanced where the step is.

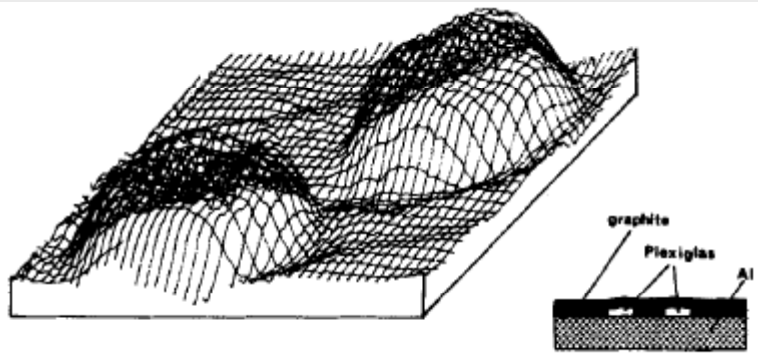

FIG. 5. Subsurface imaging of two small disks under a graphite layer on aluminum. The amplitude of the optoacoustic signal is recorded.

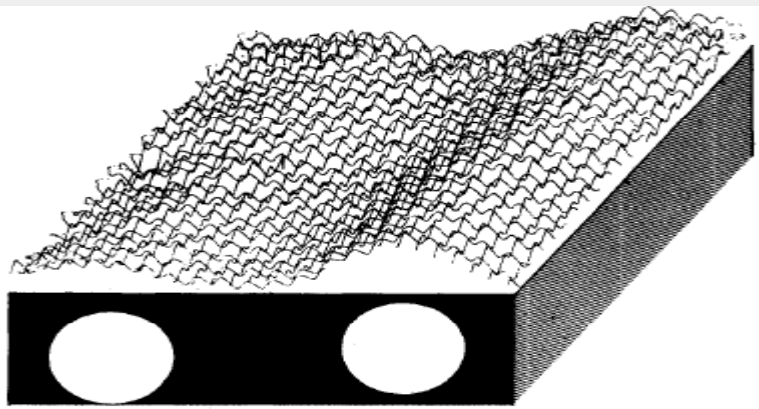

FIG. 6. Subsurface imaging of holes in an aluminum sample. Sample geometry (11×11 cm^2) is shown together with optoacoustic phase image.

P.K. Kuo , Z.J. Feng , T. Ahmed, aıd L.D. Favro, R.L. Thomas, and J. Hartikainen, Dept. of Physics, Wayne State University, Detroit, MI 482O2, USA, *"Parallel ThermaI Wave Imaging Using a Vector Lock_In Video Technique"*, Proc. 5th Int. Topical Meet. Photoacoustic Photothermal Phenomena, Heidelberg, July 27-30 (1987), pp. 415-418.

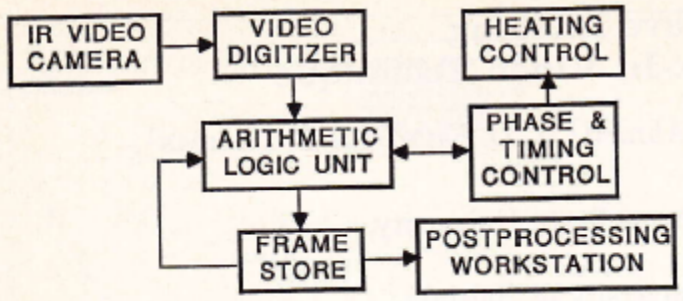

Fig. 1 Block diagram of the vector lock-in IR video imaging system

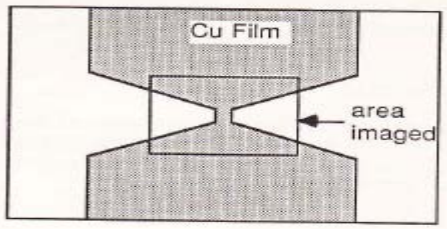

Fig. 4 Schematic diagram of the samples used in Fig. 5, showing the shape of the copper microbridge

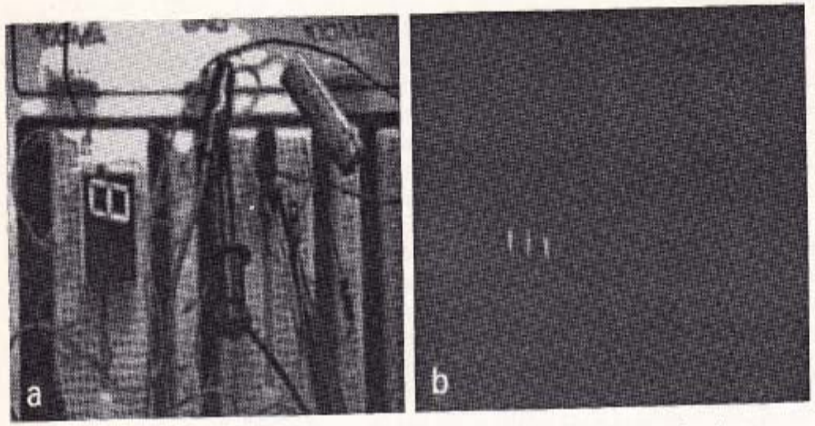

Fig. 2 A video image of a circuit board (a), together with its lock-in image after just two cycles of averaging (b)

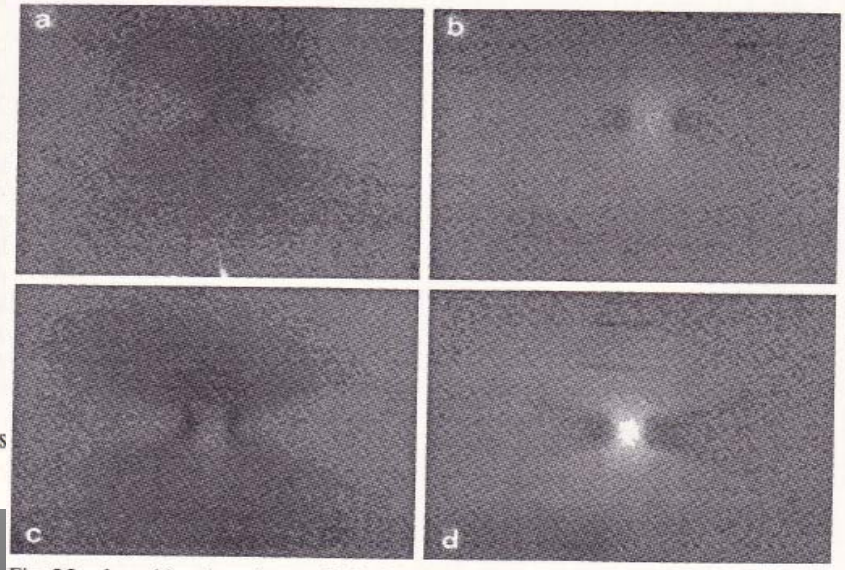

Fig. 5 In-phase (a) and quadrature (b) lock-in images of a Cu microbridge; and the same images (c,d) of a microbridge with a simulated debond. The ac current was adjusted to give the same average power input to both samples

The concept of area-wide lock-in detection as applied to thermal wave imaging was demonstrated

G. Busse, D. Wu, and W. Karpen, Institut fuer Kunststoffpruefung und Kunststoffunde. Universitaet Stuttgart, Pfaffenwaldring 32, D-7000 Stuttgart 80, Germany, *"Thermal wave imaging with phase sensitive modulated thermography"*, J. Appl. Phys. **71** (8), 3962 (April 1992)

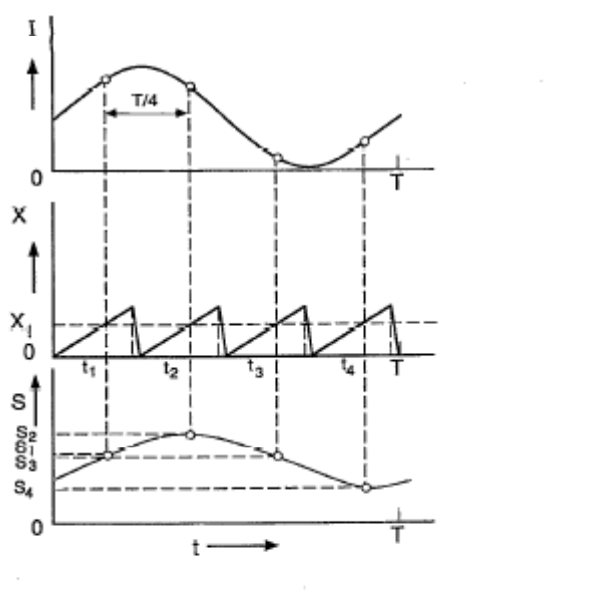

FIG. 1. Principle of phase sensitive thermography: Time dependence of light intensity I is shown together with scanning radiometer coordinate x and with four signal values S_1 to S_4 obtained at x_1 which are related to the thermal wave curve S constructed for x_1.

correct phase. Though more data points reduce the noise, the following discussion will concentrate on four equidistant signal data points, S_1 to S_4, from which the phase shift φ with respect to a given reference modulation results according to

$$\phi = \operatorname{arctg}\left(\frac{S_1 - S_3}{S_2 - S_4}\right) \quad (1)$$

while magnitude A is found to be

$$A = \sqrt{(S_1 - S_3)^2 + (S_2 - S_4)^2}. \quad (2)$$

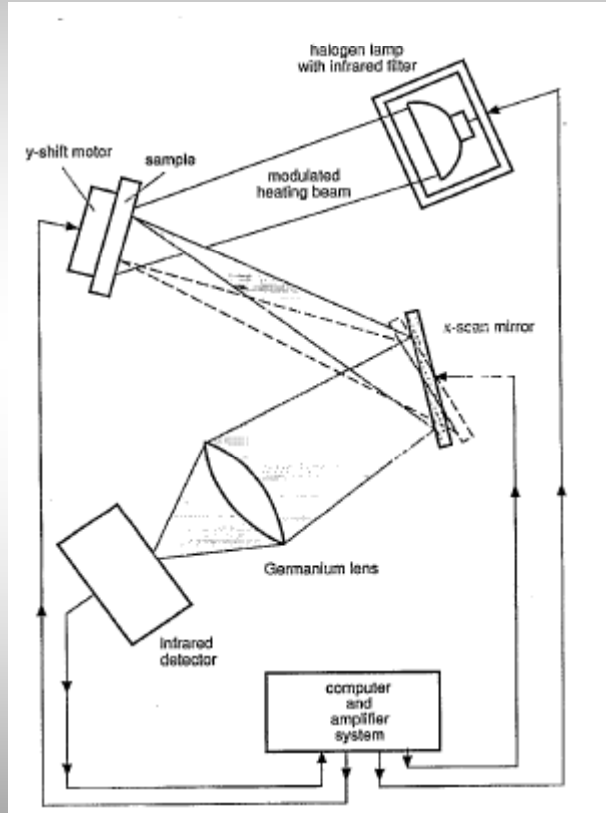

FIG. 2. Experimental arrangement for phase sensitive modulated thermography with sinusoidal modulation of light intensity.

G. Busse, D. Wu, and W. Karpen, J. Appl. Phys. **71** (8), 3962 (April 1992)

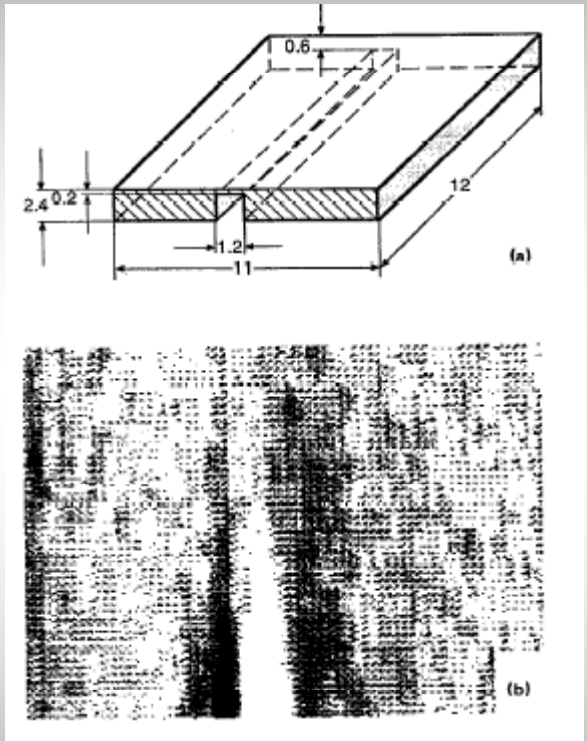

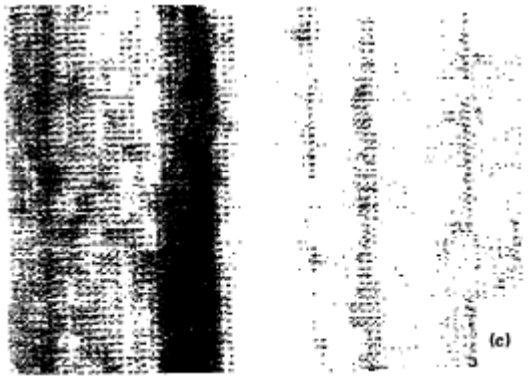

FIG. 3. Depth range test with phase sensitive thermography: CFRP-sample geometry (a) together with magnitude (b) and phase angle (c) images obtained at 0.9 Hz. Contrast is enhanced by differentiation. Dimensions are given in mm.

CONCLUSION

To summarize, the feasibility of thermal wave imaging with phase sensitive thermography ("thermal wave thermography") has been demonstrated where the modulation frequency can be much lower than the line or image frequency.

S. Huth[1], O. Breitenstein[1], A. Huber[2], D. Dantz[2], U. Lambert[2], F. Altmann[3], Max-[1] Planck-Institut für Mikrostrukturphysik Halle, Weinberg 2, D-06120 Halle; [2] Wacker Siltronic AG, P.O. Box 1140, D-84479 Burghausen; [3] Fraunhofer-Institut für Werkstoffmechanik, Institutsteil Halle, Heideallee 19, D-06120 Halle, Germany

"Lock-in IR-Thermography - a novel tool for material and device characterization", Solid-State Phenom. 82 (2000)

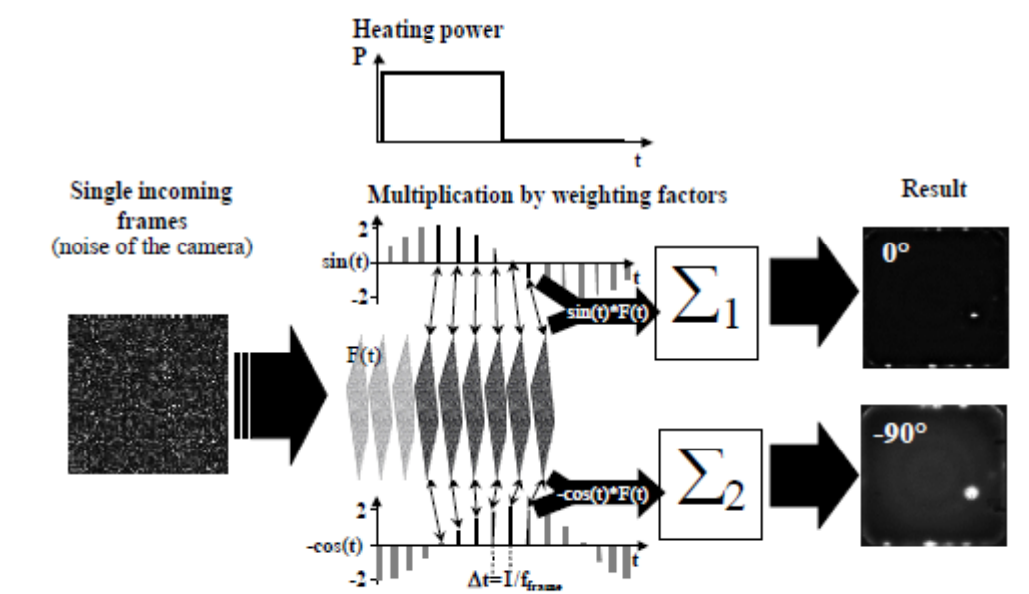

Fig. 1: Principle of Lock-in IR-Thermography.

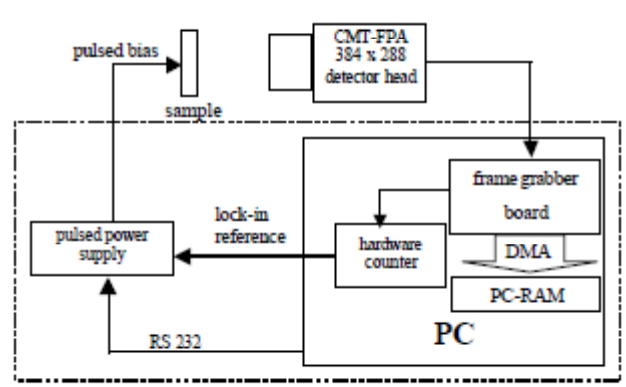

Fig. 2: Scheme of the TDL 384 M "Lock-in" system

Conclusion

Lock-in thermography has been shown to be a versatile and very sensitive tool to detect local heat sources in electronic components. It has been used successfully for detecting local shunts in solar cells, for imaging the local distribution of gate oxide integrity (GOI) defects, and for the functional testing of integrated circuits (ICs).

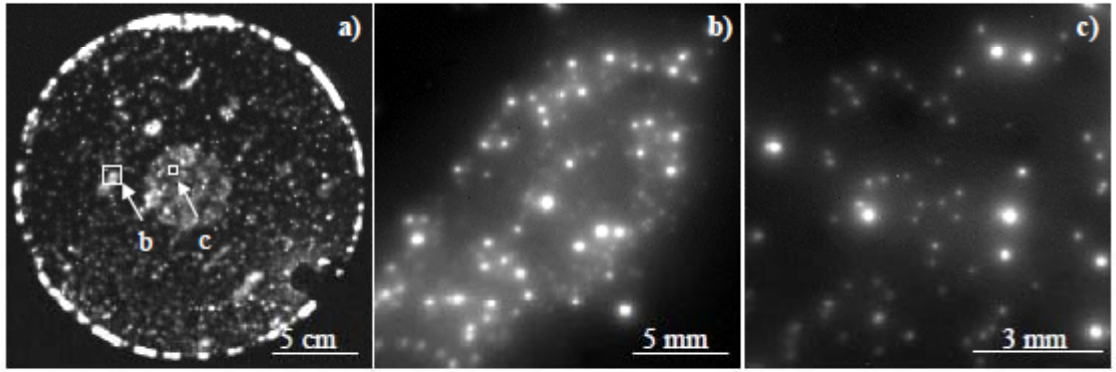

Fig. 5: Thermograms of a whole wafer (a), a defect agglomerat (b) and a 1x1 cm^2 area (c) for the determination of the defect density.

P. Menner, H. Gerhard, and G. Busse, Institute of Polymer Technology (IKT), Non Destructive Testing (IKT-ZfP), University of Stuttgart, Pfaffenwaldring 32, D-70569 Stuttgart, Germany, "*Thermal wave imaging using lockin-interferometric methods*", Journal of Physics: Conference Series **214** (2010) 012090

- Thermal wave lockin-interferometry, though it is very much like Lockin-thermography, the image generating mechanism is substantially different: The thermal wave generates periodical thermal expansion correlated with an overall deformation where the depth integral of the thermal wave is involved. The way how phase is extracted in this lockin-interferometry is similar, though more complicated than in lockin thermography: During the slow periodical deformation, interferometric fringe patterns are recorded continously which are then converted into a stack of images showing modulated thermal expansion.

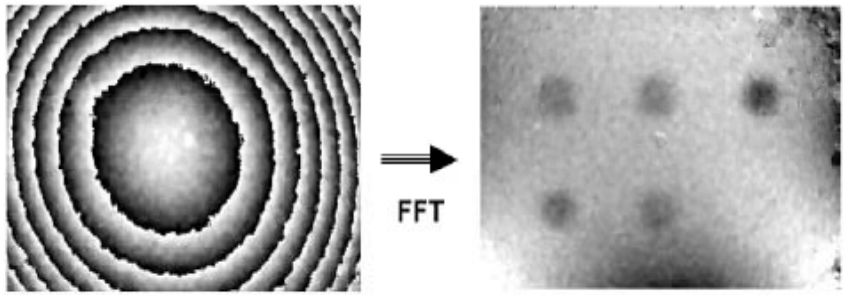

Figure 1. Suppression of whole body deformation. One conventional ESPI image from the stack (left) and resulting lockin phase angle image (right) obtained on the same sample provided with rear surface holes.

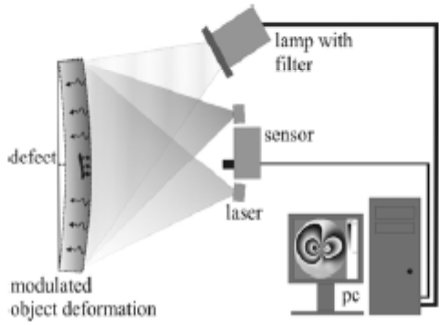

Figure 3. Setup for Lockin-Shearography. The sensor is a conventional shearography camera generating two images that are slightly tilted with respect to each other due to a modified Michelson setup. Superposition of the two images results in fringes indicating the derivative of the deformation state.

Figure 5. Test panel of an aircraft. Stringer areas disbonded in buckling test are afterwards revealed in the phase angle image (see arrow).

DEPTH-SELECTIVE (RESOLVED) vs. DEPTH-INTEGRATED THERMAL-WAVE IMAGING: The Thermal-Wave Radar-I

N. Tabatabaei, A. Mandelis, and Bennett T. Amaechi Center for Advanced Diffusion-Wave Technologies (CADIFT), Department of Mechanical and Industrial Engineering, University of Toronto, Toronto, ON, M5S 3G8, Canada, *"Thermophotonic radar imaging: An emissivity-normalized modality with advantages over phase lock-in thermography"*, Appl. Phys. Lett. **98** (16), 163706 (2011)

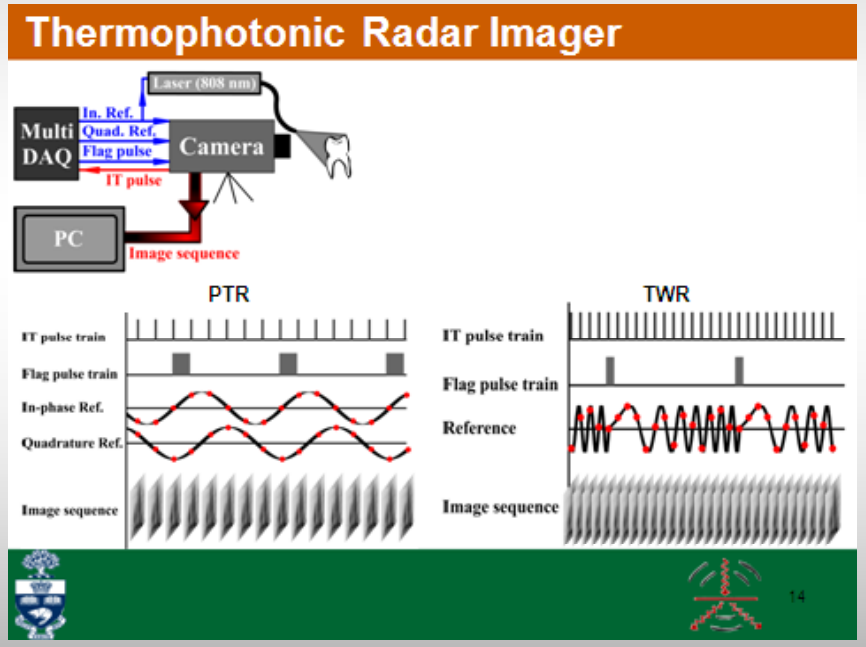

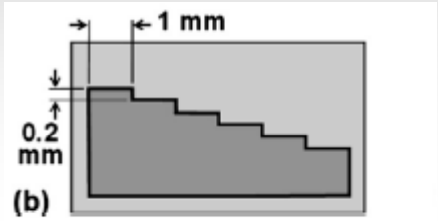

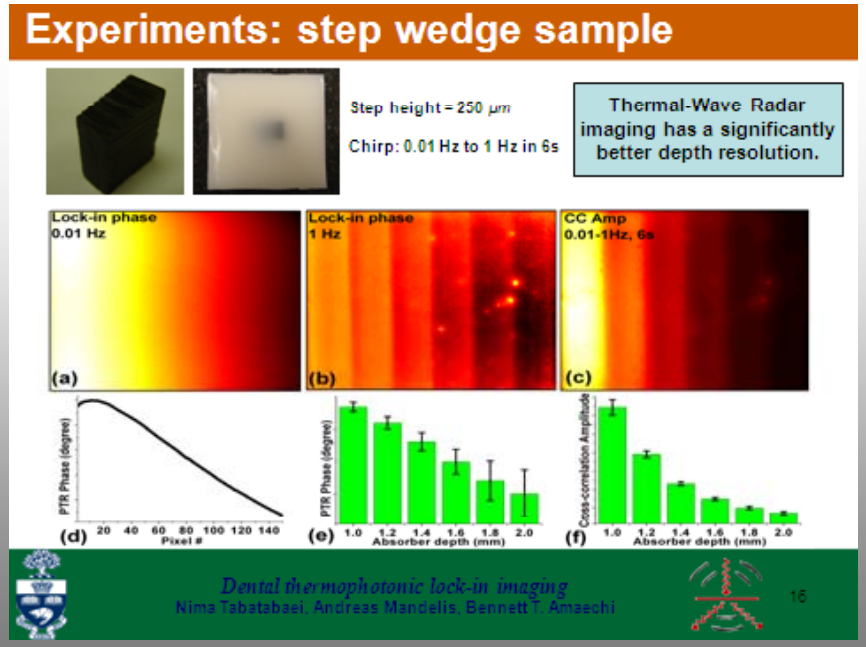

This work experimentally demonstrates the advantages of chirped modulation and introduces a thermophotonic modality of thermal-wave radar based on an emissivity-normalized, higher-dynamic-range contrast parameter known as cross-correlation phase.

N. Tabatabaei, A. Mandelis, and Bennett T. Amaechi, Appl. Phys. Lett. **98** (16), 163706 (2011)

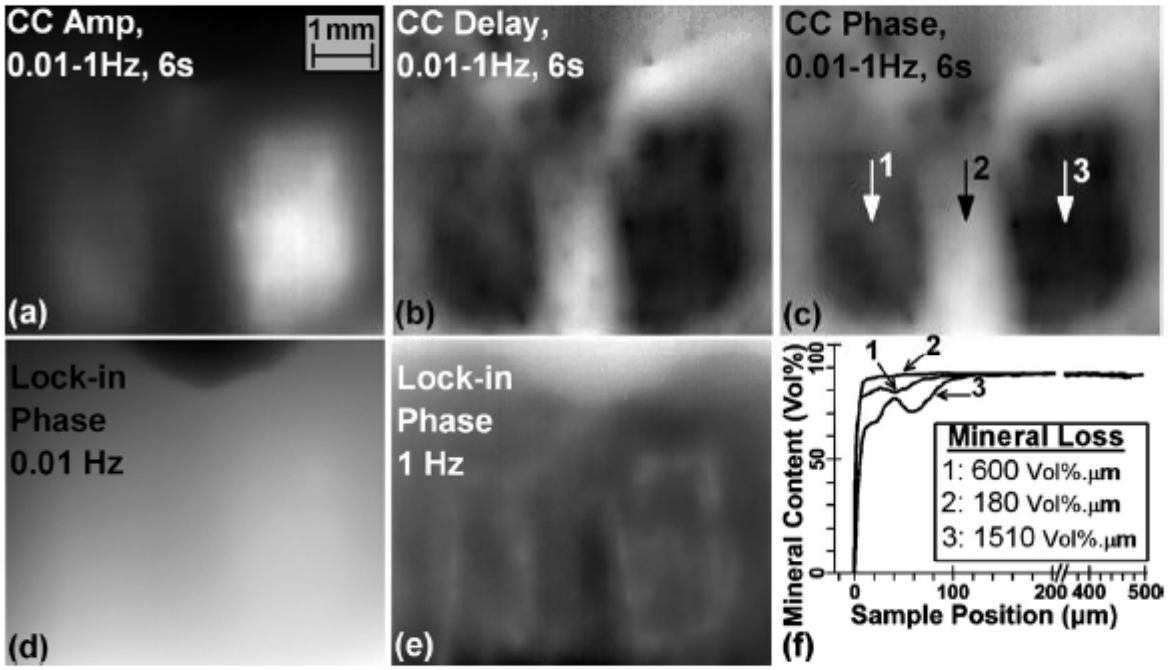

FIG. 4. Thermophotonic radar and phase LI imaging of sample 3. (a) CC amplitude image; (b) CC peak delay time image; and (c) CC phase image (chirp parameters: 0.01–1 Hz in 6 s). LIT phase images at (d) 0.01 Hz and (e) 1 Hz; (f) TMR mineral profiles at points 1–3 indicated in part (c), the inset depicts the amount of mineral loss.

10 days of treatment

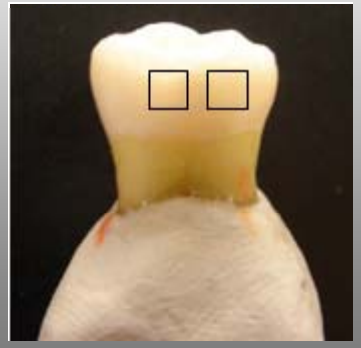

20 days of treatment

DEPTH-SELECTIVE (RESOLVED) vs. DEPTH-INTEGRATED THERMAL-WAVE IMAGING: The Thermal-Wave Radar - II

N. Tabatabaei and A. Mandelis, Center for Advanced Diffusion-Wave Technologies (CADIFT), Department of Mechanical and Industrial Engineering, University of Toronto, Toronto, ON, M5S 3G8, Canada, *"Thermal Coherence Tomography Using Match Filter Binary Phase Coded Diffusion Waves"* PRL **107**, 165901 (October 2011)

Binary Phase Code (BPC) optimizes thermal-wave depth selectivity through suppresion of pulse-compression sidelobes and optimized axial resolution:

Thermal Coherence Tomography

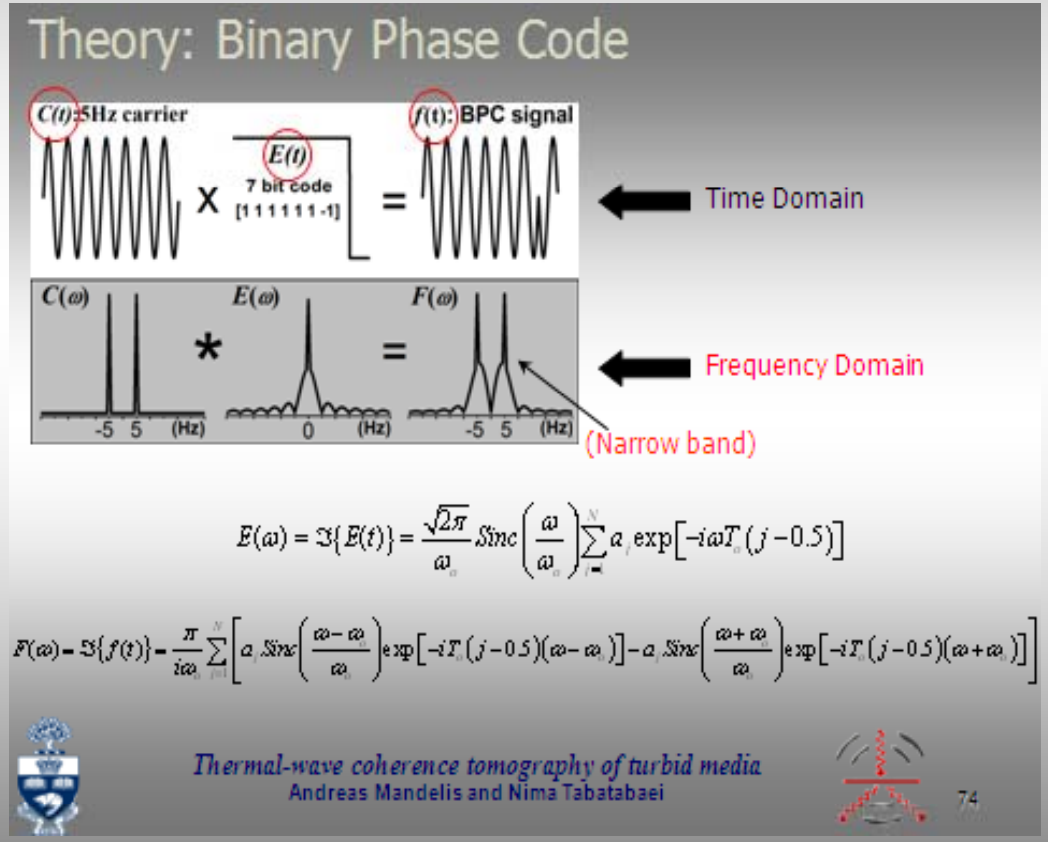

Experimental verification of TCT

Depth-Selective imaging

Improvement in depth resolution

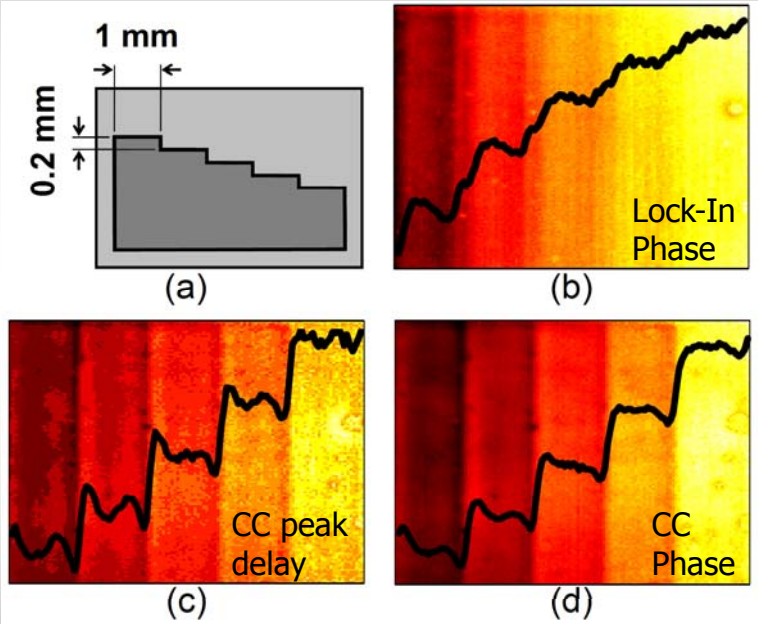

Resolving overlying absorbers

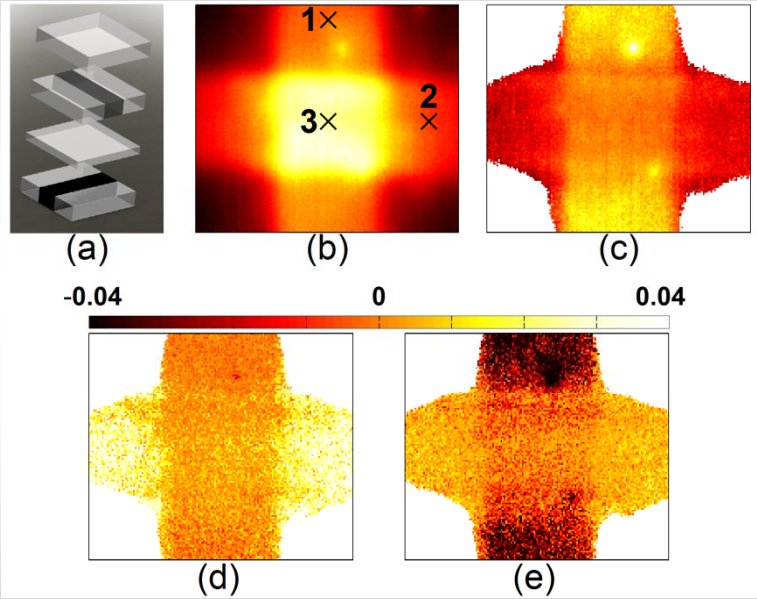

16-bit code; 3 Hz

3-bit code; 1 Hz

Thermal-wave Coherence Tomography (TCT)

Through progressively delaying the matched-filter and registering pixels coherent to the delayed filter one can form thermal-wave coherence tomographic images.

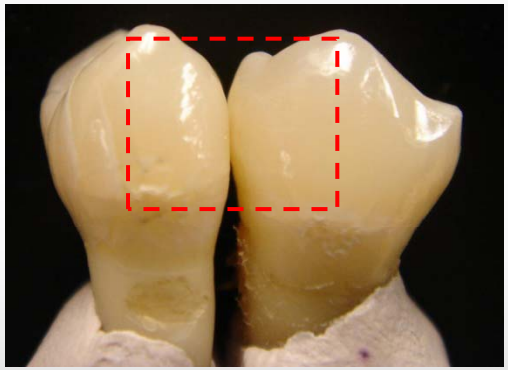

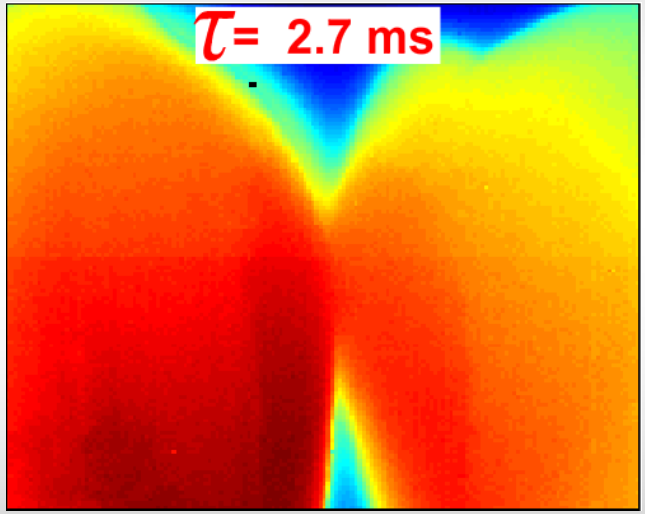

Industrial outlook for thermal-wave non-destructive imaging technologies

- **Thermosensorik GmbH**, Am Weichselgarten 7. D-91058 Erlangen Germany; and **DCG Systems, Inc.,** 45900 Northport Loop East, Fremont, CA 94538, USA.
- Together they make high-resolution lock-in thermography solutions for fault analysis of electronic components available the the world's microelectronic industry.

- **FLIR Systems,** America's Main Office, Boston, MA.

Thesa: Full Radiometric Software Suite for Lock-in Thermography Applications. Camera systems for non-contact imaging of stress in materials and structures. Lock-in thermography processing for Stress Analysis, Electronics and NDE. Complex structures undergoing real loading. Temporal stress analysis Random & transient loading. Dissipated energy measurement. Motion compensation

- **MoviTHERM,** 15540 Rockfield Blvd, Suite C-110, Irvine, CA 92618, USA
- Lock-in Thermography Enables Solar Cell Development.

- **Thermal Wave Imaging, Inc.,** 845 Livernois St., Ferndale, MI 48220 USA
- TWI is operating in the field of Thermographic NDT and is a solution provider for demanding applications in the aerospace, power generation and automotive industries.